

Name: Zhang Zhenyu

Degree: Master of Engineering

Dept: Electrical and Computer Engineering

Thesis Title: The miniaturization and bandwidth enhancement of printed circuit balun designs for wireless applications

Abstract

This thesis focuses on the miniaturization and bandwidth enhancement of balun designs for wireless applications fabricated on the Low Temperature Co-fired Ceramic (LTCC) or conventional Printed Circuit Board (PCB). Firstly, for the purpose of size reduction and performance improvement, the LTCC technique was employed in our balun designs. Several balun structures were developed using the LTCC technique. Secondly, the conventional Marchand balun was examined and design curves were plotted. Based on the even- and odd-mode method analysis, a planar Marchand balun, using a patterned ground plane in a single layer PCB environment, is presented for the first time. Thirdly, a new broadband balun transition, which can either be employed in microstrip-to-microstrip or microstrip-to-CPS applications, is presented for the first time. The evaluation was made based on the measured results for two back-to-back transitions. Finally several passive phase shifter configurations were studied, and a novel concise and low-cost wideband planar balun, which consists of a two-way Wilkinson power divider and a 180° phase shifter, is proposed.

Key words: balun, Marchand balun, LTCC, size reduction, transition, planar, wideband, phase shifter

THE MINIATURIZATION AND BANDWIDTH
ENHANCEMENT OF PRINTED CIRCUIT BALUN DESIGNS
FOR WIRELESS APPLICATIONS

ZHANG ZHENYU

NATIONAL UNIVERSITY OF SINGAPORE

2005

THE MINIATURIZATION AND BANDWIDTH
ENHANCEMENT OF PRINTED CIRCUIT BALUN DESIGNS
FOR WIRELESS APPLICATIONS

ZHANG ZHENYU

(B. ENG. HUAZHONG UNIVERSITY OF SCIENCE AND
TECHNOLOGY, P. R. CHINA)

A THESIS SUBMITTED
FOR THE DEGREE OF MASTER OF ENGINEERING
DEPARTMENT OF ELECTRICAL AND COMPUTER ENGINEERING
NATIONAL UNIVERSITY OF SINGAPORE

2005

Acknowledgement

I would like to thank all the persons who have given me their help in the writing of this thesis. First of all, I want to thank the Electrical and Computer Engineering (ECE) Department of the National University of Singapore (NUS) and the Institute for Infocomm Research (I²R) for their strong support throughout the course of my research.

I am extremely grateful for my supervisor Dr. Yongxin Guo. In my research, over the past two years, I have benefited much from his invaluable and patient instructions.

I thank my former colleagues in the Communication and Device Division of the Institute for Infocomm Research. In particular, Mr. Yuzhe Wei and Mr. Yufeng Ruan have provided me with many helpful suggestions for my research work. I also thank Mr. Poon Kai Ming for his kind assistance in my PCB fabrication.

Special thanks are extended to my lifelong friends and laboratory mates, Mr. Ashok Prabhu and Mr. Jonathan Khoo, and to all my friends in Singapore and China, whose understanding and support are important to me.

Finally, I would like to express my deepest gratitude to my parents who brought me up and walked me through various stages of life.

Contents

1	Introduction	1
2	Balun design using Low Temperature Co-fired Ceramic (LTCC) technique... 7	
2.1	Basic elements in LTCC configuration.....	10
2.1.1	Embedded multilayer capacitors in LTCC	10
2.1.2	Semi-lumped inductors in LTCC.....	10
2.1.3	Resistors in LTCC.....	11
2.1.4	Spiral broadside coupled striplines (SBCS) in LTCC	12
2.1.5	Via hole transitions in LTCC.....	13
2.1.6	Substrate material.....	13
2.2	A LTCC Marchand Balun.....	14
2.2.1	Structure description.....	14
2.2.2	Design procedure	16
2.2.3	Simulation and measurement results	17
2.3	A LTCC Full-matching Marchand balun.....	19
2.3.1	Structure of the full matching Marchand balun	19
2.3.2	Design example.....	21
2.3.3	Simulation and measurement results	22
2.4	LTCC size-reduced balun realized by LC resonanced method	24
2.5	Design of LTCC LC resonant balun	33
2.5.1	A four-capacitor LTCC LC resonant balun	33

CONTENTS

2.5.2	A two-capacitor LTCC LC resonant balun	37
2.6	Discussion and comparison.....	41
2.7	Conclusion	42
3	Study and design of a Marchand balun using a patterned ground plane	41
3.1	Theoretical analysis of the conventional Marchand baluns	46
3.2	Improved Planar Marchand Baluns Using A Patterned Ground Plane.....	51
3.2.1	Structure Description	51
3.2.2	Design procedure	53
3.2.3	Results and Discussions.....	56
3.3	Conclusion	61
4	A Broadband Tapered Balun Transition.....	60
4.1	Transition from microstrip line to parallel strip line.....	65
4.2	A Novel Planar Tapered balun.....	66
4.2.1	Structure description	67
4.2.2	Microstrip-to-microstrip balun transition	68
4.2.3	Microstrip-to-CPS balun transition.....	70
4.3	An application of the proposed UWB planar tapered balun	74
4.3.1	Antenna Configuration.....	74
4.3.2	Simulation and measurement results	75
4.4	Conclusion	78
5	Wideband Microstrip Balun Design Using Phase Shifters	79
5.1	Standard Schiffman phase shifter	82

CONTENTS

5.1.1	Structure description	82
5.1.2	Analysis.....	82
5.1.3	Design curve and example	85
5.2	A broadband 180 ⁰ phase shifter	93
5.2.1	Analysis of the broadband 180 ⁰ phase shifter.....	93
5.3	A new wideband planar balun on a single-layer PCB	96
5.3.1	Design theory	97
5.3.2	Structure description	99
5.3.3	Simulation and measurement results	100
5.3.4	Comparison and discussion.....	102
5.4	Conclusion	106
6	Conclusion	107
	Bibliography.....	110

Summary

As a key component in various wireless communications systems, the balun has attracted widespread attention from researchers. This thesis focuses on the investigation and design of printed circuit baluns for wireless communications using the Low Temperature Co-fired Ceramic (LTCC) or the Printed Circuit Board (PCB) technology.

With the development of small size wireless communications systems, size reduction and performance improvement have become a hot topic for balun designs. To achieve this goal, the LTCC technique has proven a good choice. LTCC circuits allow for a multilayer structure in which transmission lines can be folded into the meandered forms. Meanwhile, the LTCC process allows passive components, such as resistors, capacitors and inductors, to be embedded in a multilayer and integrated module. Chapter 2 focuses on the miniaturization of balun designs using the LTCC technique. In this chapter, first of all, in a bid to achieve size reduction, a conventional 2.4 GHz Marchand balun and an improved full-matching Marchand balun were realized using the LTCC technique. Moreover, the LC resonance method was employed in LTCC balun structures so as to further reduce the size. Several LC resonance balun structures were analyzed using the even-odd mode analysis method and design curves were plotted. Finally, based on the design curves, design examples are presented to demonstrate the analysis process.

Among all the previous balun structures, the Marchand balun and its variations are the most popular configurations. However, Marchand baluns are difficult to be realized in a

SUMMARY

single layer PCB environment due to the tight coupling requirement. In Chapter 3, we explore the means of designing a Marchand balun on a single-layer and double-sided low permittivity substrate. In this chapter, the conventional Marchand balun was examined, of which design curves were plotted. A planar Marchand balun using a patterned ground plane in a single layer PCB environment is presented for the first time.

Balun can also be referred to as a transition between an unbalanced line, such as microstrip or coplanar waveguide, and a balanced line, such as broadside parallel strip, slotline and coplanar stripline (CPS). Broadside parallel stripline, slotline and coplanar stripline are all widely used in the feeding networks of printed dipole antennas, balanced mixers and optoelectronic circuits. In Chapter 4, a broadband uniplanar balun transition, which can either be used as a microstrip-to-microstrip or a microstrip-to-CPS transition, is presented. The proposed balun transition consists of a section of edge coupled transmission line, and a taper is employed on both of the coupled lines to increase its bandwidth. The performance of the newly proposed transition is investigated in terms of a microstrip-to-microstrip and a microstrip-to-CPS transition.

Chapter 5 focuses on developing a low-cost wideband balun structure based on a two-way power divider and a wideband phase shifter which can be easily realized using the conventional PCB technique. Several passive wideband phase shifters are first studied. A Schiffman phase shifter is examined for its optimal bandwidth performance when a certain phase derivation is chosen. Since the Schiffman phase shifters require tight coupling between coupled lines and are not suitable for large phase shift, a simple 180° phase shifter structure is studied. A novel planar balun structure on a single-layer PCB using this wideband 180° phase shifter is presented.

List of Figures

Figure 1.1: Applications of balun in wireless communication systems.....	2
Figure 1.2: Planar balun structures	4
Figure 2.1: Flow chart of the LTCC fabrication process	8
Figure 2.2: An embedded multilayer capacitor in LTCC	10
Figure 2.3: A semi-lumped inductor in LTCC.....	10
Figure 2.4: Dimension description of thin film resistor in LTCC	11
Figure 2.5: Spiral Broadside Coupled Striplines structure	12
Figure 2.6: Side view of a via hole interconnection	13
Figure 2.7: Structure of the conventional Marchand balun	14
Figure 2.8: Multilayer structure of the conventional Marchand balun	15
Figure 2.9: Performance of a single section of $\lambda/4$ coupled-line	16
Figure 2.10: Photograph of the fabricated LTCC board.....	17
Figure 2.11: S-parameters of the LTCC chip Marchand Balun.....	18
Figure 2.12: Simulated amplitude response of a non-spiraled LTCC Marchand balun ...	19
Figure 2.13: Schematic diagram of the full matching Marchand balun.....	20
Figure 2.14: Perfectly matched Marchand balun in LTCC.....	20
Figure 2.15: Photograph of the fabricated LTCC board.....	22
Figure 2.16: S parameter responses of the LTCC full-matching Marchand balun.....	23

LIST OF FIGURES

Figure 2.17: Several LC resonanced balun structures proposed in prior arts 25

Figure 2.18: Circuit analysis of the balun in Figure 2.17(a)..... 26

Figure 2.19: Design curves for determining Z_{0e} , Z_{0o} , and θ for various ωC_2 values with $\omega C_1=0$ mho and $Y_{in}=Y_{out}=0.02$ mho..... 28

Figure 2.20: Design curves for determining Z_{0e} , Z_{0o} , and θ for various combinations of ωC_2 and ωC_1 with $Y_{in}=Y_{out}=0.02$ mho..... 28

Figure 2.21: Circuit analysis of the balun shown in Figure 2.17(a) with C_1 removed 29

Figure 2.22: Circuit analysis of the balun structure in Figure 2.17(b)..... 29

Figure 2.23: Circuit analysis of the balun in Figure 2.17(c)..... 30

Figure 2.24: Design curves for determining Z_{0e} , Z_{0o} and θ for various ωC_2 values with $\omega C_1=0$ and $Y_{in}=Y_{out}=0.02$ mho 31

Figure 2.25: Design curves for determining Z_{0e} , Z_{0o} and θ for various ωC_2 values with $\omega C_1=0.01$ mho and $Y_{in}=Y_{out}=0.02$ mho 32

Figure 2.26: Multilayer structure of the four-capacitor LC resonant balun in Figure 2.17(a)..... 34

Figure 2.27: A summarized design procedure for the proposed four-capacitor LTCC chip balun..... 35

Figure 2.28: Design curves for determining Z_{0e} , Z_{0o} and θ for $\omega C_2=0.0167$ mho and $\omega C_1=0.0077$ mho with $Y_{in}=Y_{out}=0.02$ mho..... 36

Figure 2.29: S parameter responses of the four-capacitor LTCC LC resonant balun..... 37

Figure 2.30: Multilayer structure of the two-capacitor LC resonant balun in Figure 2.17(c)..... 38

LIST OF FIGURES

Figure 2.31: Design curves for determining Z_{0e} , Z_{0o} and θ for $\omega C_2=0.0055$ mho and $\omega C_1=0.0049$ mho with $Y_{in}=Y_{out}=0.02$ mho.....	39
Figure 2.32: S parameter responses of the two-capacitor LTCC LC resonant balun	40
Figure 3.1: Equivalent circuit of Marchand Baluns.....	46
Figure 3.2: A basic element in the Marchand balun structure	47
Figure 3.3: Another basic element in the Marchand balun structure.....	48
Figure 3.4: Even- mode impedance Z_{0e} versus odd- mode impedance Z_{0o} with various port impedances	50
Figure 3.5: New Planar Marchand Balun Using A Patterned Ground Plane.....	52
Figure 3.6: A summarized design procedure for the proposed Marchand balun.....	53
Figure 3.7: Even- mode impedance Z_{0e} versus odd- mode impedance Z_{0o} in the design procedure for the Marchand balun in Figure 3.6(a), $Z_a = Z_b = 50 \Omega$	54
Figure 3.8 S-parameters of the proposed Marchand Balun	57
Figure 3.9: Simulated S-parameter performance for the two contrast designs.....	58
Figure 3.10: Simulated return losses of the proposed balun with various values of depth of the air cavity d	60
Figure 4.1: Transition configurations in prior arts.....	63
Figure 4.2: Layout of microstrip tapered balun	65
Figure 4.3 Amplitude response of two back-to-back microstrip tapered baluns	66
Figure 4.4 Configuration of the balun transition	67
Figure 4.5 Structure of two back-to-back baluns.....	68
Figure 4.6: Return loss and insertion loss of the balanced back-to-back balun transition.....	69

LIST OF FIGURES

Figure 4.7: Simulated S-parameters for the contrast back-to-back microstrip-to-microstrip balun..... 70

Figure 4.8: Microstrip-to-CPS back-to-back transition configuration..... 71

Figure 4.9: Measured input return and insertion loss of the balun transition 72

Figure 4.10: Simulated S-parameter performance for the contrast back-to-back microstrip-to-CPS balun 72

Figure 4.11: Proposed UWB planar dipole antenna. 75

Figure 4.12 Simulated and measured return loss of the proposed UWB antenna 76

Figure 4.13: Measured radiation patterns of the proposed balanced UWB antenna 77

Figure 4.14: Measured peak antenna gain across the operating bandwidth 78

Figure 5.1: Standard 90 degree Schiffman phase shifter structure 82

Figure 5.2: Coupled-line transform used in the Schiffman phase shifter 83

Figure 5.3: Phase deviation versus impedance ratio ρ for the standard 90^0 Schiffman phase shifter 86

Figure 5.4: Side view of the edge coupled transmission line 87

Figure 5.5: 90^0 Schiffman phase shifter using a patterned ground plane 87

Figure 5.6: Even- mode impedance Z_{0e} versus odd- mode impedance Z_{0o} in the design procedure for the Schiffman phase shifter in Figure 5.5 88

Figure 5.7: Simulated results of the 90^0 Schiffman phase shifter design 90

Figure 5.8: Simulated amplitude and phase difference responses of the proposed 90^0 Schiffman phase shifter with various values of depth of the air cavity d 91

Figure 5.9: Simulated results of two cascaded 90^0 Schiffman phase shifters..... 92

Figure 5.10: A broadband 180^0 phase shifter structure..... 94

LIST OF FIGURES

Figure 5.11 Simulated results of the broadband 180⁰ phase shifter..... 95

Figure 5.12: Circuit schematic of the proposed planar balun 97

Figure 5.13: Even- and odd-mode analysis of the proposed balun structure..... 98

Figure 5.14: Layout graph of the planar balun 100

Figure 5.15: S parameter response of the newly proposed planar balun 101

Figure 5.16: Photograph of the fabricated board 102

Figure 5.17: Half-wave balun structure 102

Figure 5.18: Simulated results of a single section half-wave balun 103

Figure 5.19: Simulated results of a three-section half-wave balun..... 105

List of Tables

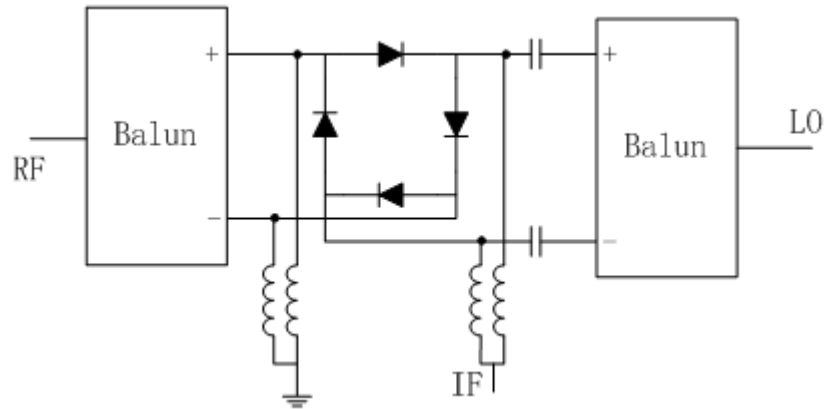
Table 2.1: Dimension consideration of cofired resistors	11
Table 2.2: Material parameters of the FERRO A6-M ceramic at 2.4 GHz	13
Table 2.3: Comparison between the present designs and the prior arts.....	41
Table 3.1: Choice of Z_{0e} and Z_{0o} for $Z_a=Z_b=50 \Omega$	50
Table 3.2: Relationship between the even- and odd-mode impedances Z_{0e} and Z_{0o} and the physical dimensions of the coupled lines with a patterned ground plane as in Figure 3.6(a).....	56
Table 3.3: Comparison between the present design and the prior arts	61
Table 4.1: Comparison between the present design and the prior arts	73
Table 5.1: Relationship between the even- and odd-mode impedances Z_{0e} and Z_{0o} and the physical dimensions of the coupled lines with a patterned ground plane as in Figure 5.5.....	89
Table 5.2: Comparison between the present design and the prior arts	106

Chapter 1

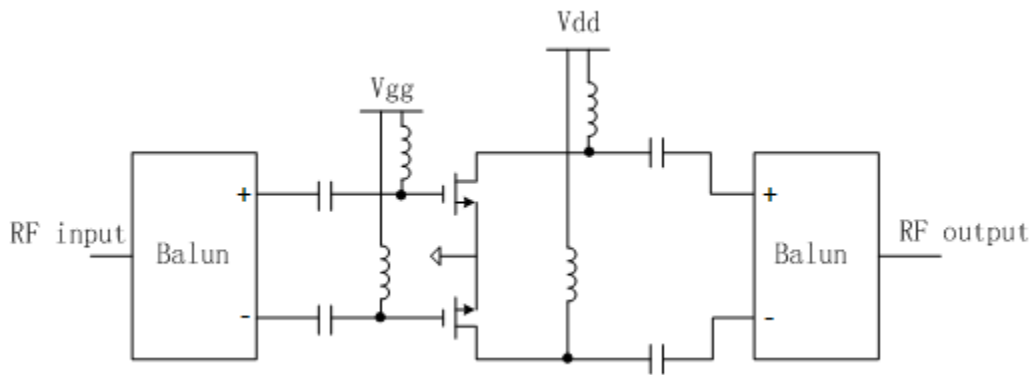
Introduction

Differential circuits are becoming more widely used in RF circuits for the same reason that they have been used for years in lower frequency circuits. The benefits of using differential circuits include immunity to electromagnetic interference, power supply noise and ground noise, even-order harmonic suppression, and tolerance to less than perfect RF grounds. Baluns are critical components in differential circuits.

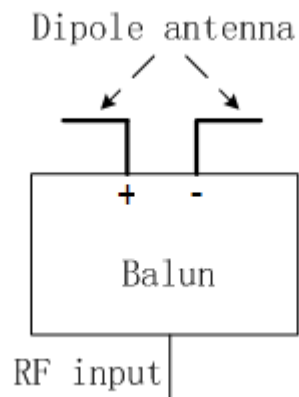
A balun (a compound term meaning “balanced-unbalanced”) is a device for converting signals between an unbalanced circuit structure and a balanced circuit structure. The signal of a balanced circuit structure comprises two signal components with the same magnitude but at a 180° phase difference. A balun consists of an “unbalanced” port converted to two “balanced ports”. The unbalanced port can be either the input or the output while the device’s balanced ports would conversely be either the output or the input. Balanced ports allow components with balanced I/Os to be used, and allow them to be coupled to/from components with unbalanced I/Os. This yields superior noise immunity due to the balanced system architecture.



(a) Double balanced mixer



(b) Push-pull amplifier



(c) Antenna

Figure 1.1: Applications of balun in wireless communication systems

CHAPTER 1. INTRODUCTION

Baluns are employed in many modern circuit designs. For example, they are key components in many wireless communications systems for realizing components such as balanced mixer, push-pull amplifier, and antenna feed networks [1-8]. Many analog circuits require balanced inputs and outputs in order to reduce noise and high order harmonics as well as improve the dynamic range of the circuits. The study of balun dates back to the first structure proposed by N. Marchand in 1944 [1]. The original balun structures, mostly in coaxial form, were used exclusively for feeding networks of dipole antennas. To the author's best knowledge, the development of planar baluns dates back to 1955, where [2] suggested a printed circuit balun for use with antennas. Since then, a large number of planar balun structures have been introduced [3-8]. Figures 1.1(a)-(c) show several balun applications in wireless communications systems. Among them, Figure 1.1(a) shows the circuit of a double balanced mixer. Double balanced mixers have the merits of a higher dynamic range, isolation between ports, and spurious signal suppression. Figure 1.1(b) exhibits a push-pull amplifier circuit, in which the baluns serve to enhance power efficiency. Meanwhile, the balanced ports are well isolated from the ground to eliminate parasitic oscillations. Figure 1.1(c) shows a dipole antenna circuit which is fed by a balun. The dipole antenna is used as a radiation component for circular polarization.

Planar baluns provide greater flexibility and better performance in mixers and modulators. They are compatible with Microwave Integrated Circuit (MIC) and Monolithic Microwave Integrated Circuit (MMIC) technologies and can be fabricated on single-sided substrates. Moreover, with their relatively small size and wide bandwidth, they are very useful in surface-mounted packages for large-volume production.

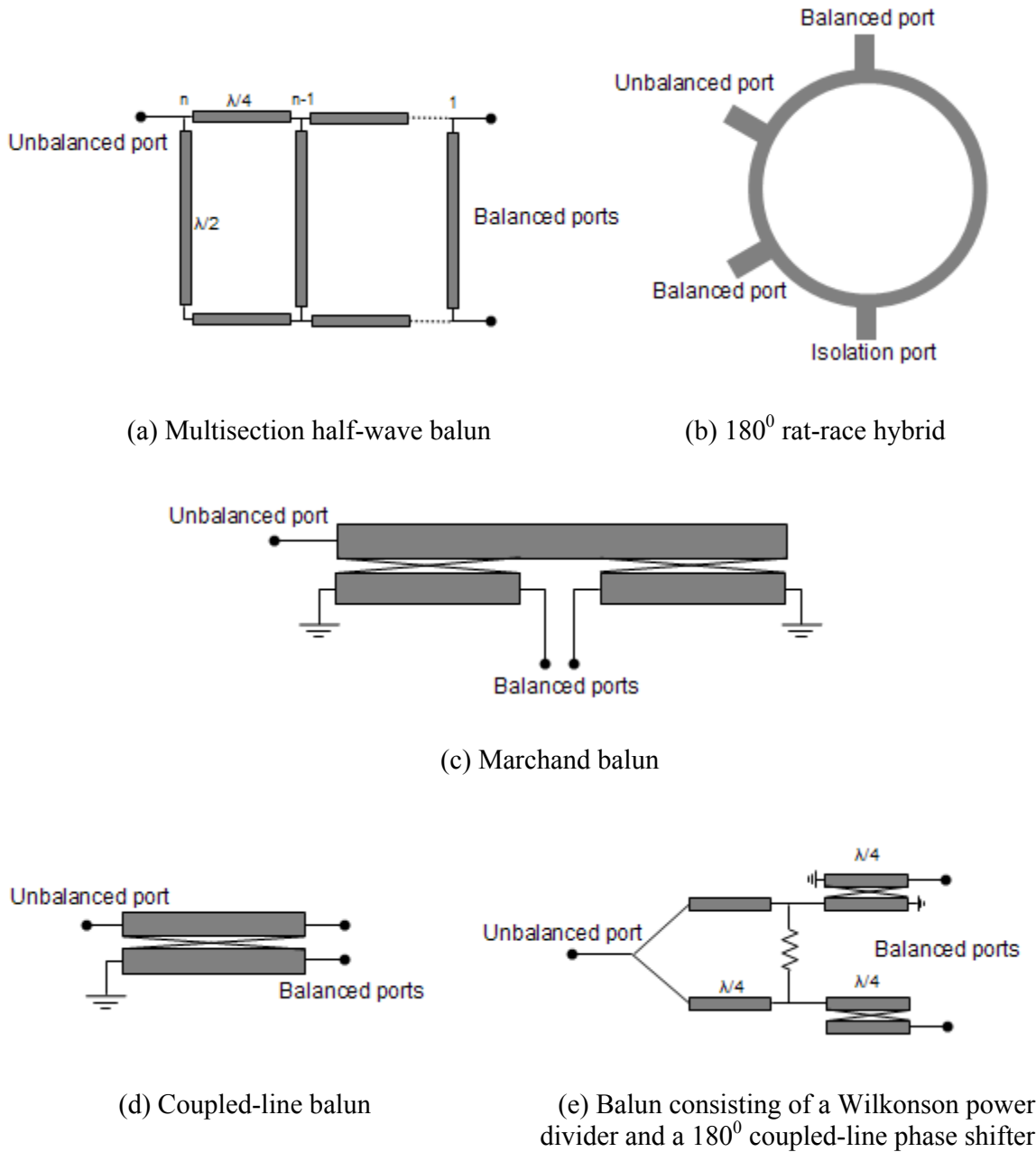


Figure 1.2: Planar balun structures

Figures 1.2(a)-(e) show several popular planar balun structures. Among them, the multisection half-wave balun and 180° rat-race hybrid are very commonly used in low cost PCB configurations because they have a very simple structure and do not require any tight coupled structure. However, the applications of these two structures in microwave circuits

CHAPTER 1. INTRODUCTION

are greatly limited because they are big in size and are unable to provide wideband performance. The Marchand balun, the $\lambda/4$ coupled-line balun and the balun consisting of a Wilkinson power divider and a 180° coupled-line phase shifter, all use tightly coupled lines in their structures. For designs using the printed circuit board (PCB) fabrication technology, the corresponding planar baluns usually tend to use the inter-digital Lange couplers or the broadside coupling lines, i.e. multi-layer structures to achieve tight coupling, which is high in cost and complex in structure.

The organization of this thesis is as follows: Chapter 2 focuses mainly on the miniaturization of balun designs using LTCC technique. In this part, first of all, a conventional 2.4GHz Marchand balun and an improved full-matching Marchand balun were realized, using the LTCC technique, in bid to achieve size reduction. Moreover, the LC resonance method was employed in LTCC balun structures so that the size can be further reduced. Several LC resonance balun structures were analyzed using the even-odd mode analysis method and design curves were plotted. Finally, based on the design curves, design examples are presented to demonstrate the analysis process. In Chapter 3, we explore the means of designing a Marchand balun on a single-layer and double-sided low dielectric substrate. In this chapter, the conventional Marchand balun is examined, based on which design curves were plotted. A planar Marchand balun using a patterned ground plane in a single layer PCB environment is presented for the first time. In this new design, by removing the ground plane under the coupled lines, the even-mode capacitance decreased substantially. Meanwhile, two additional separated rectangular conductors were placed under the coupled lines to act as two capacitors so that the odd-mode capacitance increased. As such, a well-matched Marchand balun on a double-sided PCB was achieved. In Chapter 4, a broadband uniplanar balun transition which can either be used as a microstrip-to-microstrip or a microstrip-to-CPS

CHAPTER 1. INTRODUCTION

transition is presented. The proposed balun transition consists of a section of edge coupled transmission line, and a taper employed on both of the coupled lines to increase its bandwidth. The performance of the newly proposed transition is investigated in terms of a microstrip-to-microstrip and a microstrip-to-CPS transition. Chapter 5 focuses on developing a wideband balun structure which can be easily realized using the conventional PCB technique. Considering the possibility of obtaining a compact balun structure on a single layer PCB using a two-way Wilkinson power divider and a 180^0 phase shifter, we investigated several passive wideband phase shifters. A Schiffman phase shifter was examined for its optimal bandwidth performance when a certain phase derivation is chosen. Since the Schiffman phase shifters require tight coupling between coupled lines and are not suitable for large phase shift, a simple 180^0 phase shifter structure was studied. A novel planar balun structure on a single-layer PCB, using this wideband 180^0 phase shifter, is presented. The last chapter concludes this thesis.

The author's main contribution in this thesis is as follows:

In Chapter 2, several miniaturized LTCC baluns have been designed. The LC resonance balun structures were analyzed using the even-odd mode analysis method and demonstrated using design examples. In Chapter 3, a new Marchand balun structure, which can be realized on a single-layer double-side low dielectric substrate, is proposed and analyzed using the even- and odd-mode analysis method. In Chapter 4, a broadband uniplanar balun transition which can either be used as a microstrip-to-microstrip or a microstrip-to-CPS transition is presented. In addition, a UWB omnidirectional planar dipole antenna, fed by the planar tapered balun, is proposed and studied. In Chapter 5, a wideband balun structure, which can be easily realized using the conventional PCB technique, is proposed and investigated.

Chapter 2

Balun design using Low Temperature Co-fired Ceramic (LTCC) technique

With the development of wireless communications, compact and low cost circuit fabrications have become more and more attractive. Low Temperature Co-fired Ceramic (LTCC) technology is a product with these features. Today it is widely used for applications in the automotive, aerospace, military and telecommunications sectors.

LTCC is a multi-layer ceramic technology which processes the ability to embed passive elements, such as resistors, capacitors and inductors, into a ceramic interconnect package, while the active elements are mounted at the top layer. Up to 50 layers can be constructed. The basic substrates for LTCC-Technology are unfired (green) layers of dielectric glass-ceramics materials in a polymer binder cast. In the LTCC fabrication, green tapes are first preconditioned and blanked for fabrication preparation. Then, holes are punched to create vias through layers. Each via hole is filled with conductive material and layers are printed with appropriate pattern separately. After that, all layers are stacked, laminated and co-fired at a certain temperature between 800°C and 900°C into a highly compact ceramic structure. Finally, some materials may have to be postfired and the fired parts are cut into smaller

pieces. Figure 2.1 summarizes the LTCC fabrication procedure. Because of the low firing temperature, it is possible to use low resistive materials like silver and gold instead of molybdenum and tungsten (which have to be used in conjunction with the HTCCs). Unlike other technologies, such as the CMOS process, fabrication of LTCC is a parallel process. Each layer is fabricated separately and independent of each other. Individual layers can then be examined and inspected. If failure is found, only the defective layer, instead of the whole structure, need to be fabricated again. High yield, reduction in cost and time saving can be achieved.

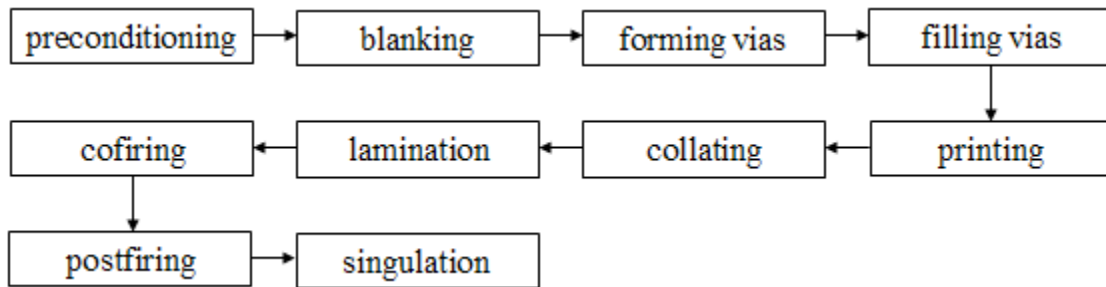


Figure 2.1: Flow chart of the LTCC fabrication process

The last decade of the past century has seen the appearance of many commercial LTCC material systems including ceramic tapes and suitable conductor and resistor pastes (duPont 951 and 943, Ferro A6-5-M-13, Heraeus CT700). With the supports from these material systems, the LTCC technique has been intensively studied in the area of microwave circuit designs. Many applications using LTCC have been introduced, such as LC filters, baluns, couplers, chip antenna, RF diode switches and highly integrated modules (RF & Microwave Receive / Transmit Modules) [9-16]. These LTCC products demonstrate huge advantages in terms of superior electrical performance, reliability, circuit miniaturization and surface mounting.

This chapter focuses on the size reduction and performance improvement of balun design in the LTCC environment. Firstly, a conventional 2.4 GHz Marchand balun is folded and realized in the LTCC multilayer substrate. Secondly, to improve the output matching and isolation of the conventional Marchand baluns, an improved LTCC Marchand balun with all the ports fully matched is implemented. Finally, the capacitors loaded method was employed in the LTCC balun structures so that the size can be further reduced. Several structures were analyzed using the even-odd mode analysis method and the design curves were generated and plotted. Based on the design curves, we present two design examples in a LTCC environment to demonstrate our analysis. It should be mentioned that the full matching balun and the two-capacitor LC resonant balun proposed in this chapter were realized with LTCC technology for the first time. Moreover, although the chip-typed conventional Marchand LTCC balun and the four-capacitor LTCC LC resonant balun have been reported elsewhere, a clear design guide was presented for the first time in this chapter. All the work done in this chapter were supported by a consortium of four R&D institutes including DSO National Laboratories (DSO), National University of Singapore (NUS), Institute for Infocomm Research (I²R) and Singapore Institute of Manufacturing Technology (SIMTech). All the LTCC fabrications were outsourced to SIMTech. More details about SIMTech can be found from the website www.SIMTech.a-star.edu.sg .

2.1 Basic elements in LTCC configuration

2.1.1 Embedded multilayer capacitors in LTCC

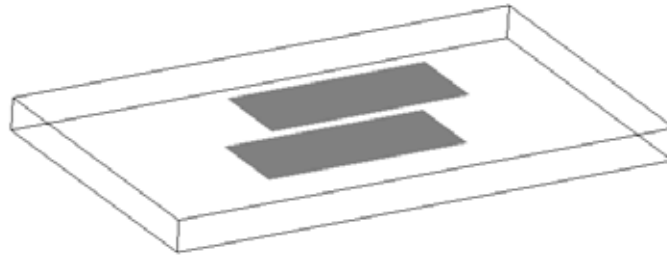


Figure 2.2: An embedded multilayer capacitor in LTCC

The shape of the embedded multilayer capacitor in LTCC is shown in Figure 2.2. It consists of two conductors separated by a dielectric substrate. The Conductors are typically printed on the green tape, and are placed on either an exposed surface or a buried layer.

2.1.2 Semi-lumped inductors in LTCC

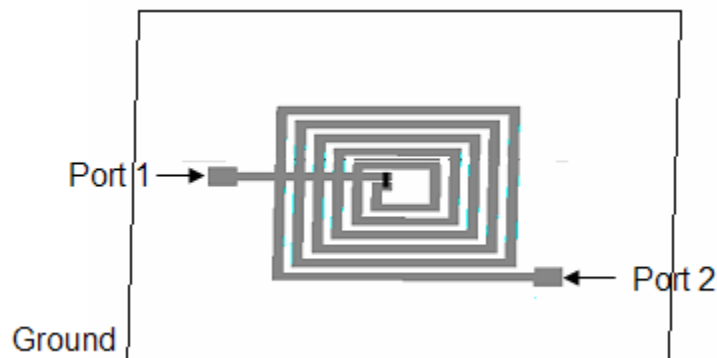


Figure 2.3: A semi-lumped inductor in LTCC

The semi-lumped inductors in LTCC can be realized using transmission lines with inductive characteristics. The value and quality factor of the inductors can be controlled by changing

the physical dimension of the transmission lines and the shunt capacitance between the transmission lines and ground. Figure 2.3 shows an example of a semi-lumped inductor in LTCC. To reduce the size of the inductors, the transmission line is folded into a spiral form.

2.1.3 Resistors in LTCC

In LTCC technique, thin film resistance materials are used to form resistors. Figure 2.4 shows dimension description of resistor in LTCC circuits. Table 2.1 gives a basic consideration for dimension.

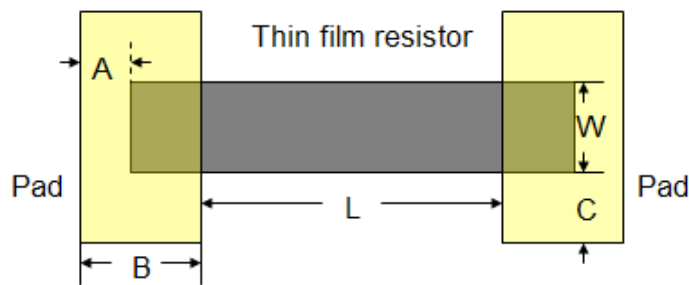


Figure 2.4: Dimension description of thin film resistor in LTCC

Table 2.1: Dimension consideration of cofired resistors

	Description	Preferred (mil)	Minimum (mil)
L	Resistor length	25	15
W	Resistor width	25	15
A	Edge spacing	5	3
B	Pad width	15	7
C	Edge spacing	5	3

The value of resistors is defined as:

$R = \rho' * L/W$, where ρ' is resistivity in ohms/square, L/W is # of squares

2.1.4 Spiral broadside coupled striplines (SBCS) in LTCC

Spiral Broadside Coupled Striplines (SBCS) have been conventionally used in LTCC technique to achieve smaller board space requirement. As shown in Figure 2.5, the SBCS structure is modified from the Broadside Coupled Stripline (BCS) structure. In the SBCS structure, the line spacing between neighboring portions of the spiral is important. In fact, electric potential at two neighboring ones are almost equal; therefore a magnetic wall will appear at the midline between them, reducing their mutual disturbance. From experience, this disturbance can be ignored when the line spacing between neighboring portions of the spiral S is approximately equal to the width of the coupled transmission line W .

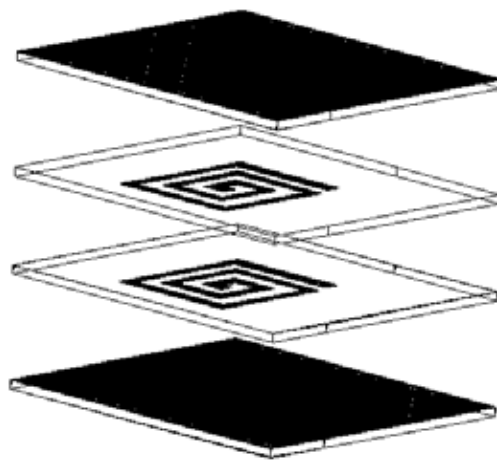


Figure 2.5: Spiral Broadside Coupled Striplines structure

2.1.5 Via hole transitions in LTCC

In LTCC technique, via holes are commonly used to connect two stacked striplines. For example, Figure 2.6 shows the side view of a via hole interconnection.

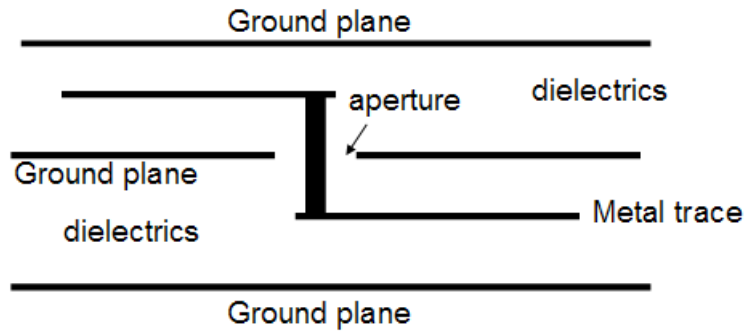


Figure 2.6: Side view of a via hole interconnection

2.1.6 Substrate material

Table 2.2: Material parameters of the FERRO A6-M ceramic at 2.4 GHz

CERAMIC TYPE	FERRO A6-M
DIELECTRIC CONSTANT ϵ_r	5.9
DISSIPATION FACTOR $\tan\delta$	0.0015
FIRED THICKNESS (INCH)	.0037

In our design, FERRO A6-M ceramic is used as the substrate material. LTCC-Technology data sheets state the dissipation factor of the FERRO A6-M ceramic to be 0.0012 within the range 0.1-2 GHz. For an operating frequency of 2.4 GHz, a dissipation factor of 0.0015 is

assumed. Table 2.2 summarizes the material characteristics of the FERRO A6-M ceramic used in our design.

2.2 A LTCC Marchand Balun

The miniaturization of RF telecommunications devices in portable applications, in order to reduce size, weight, cost, and power consumption, has become increasingly widespread. Baluns have been commonly used in RF front-end wireless systems; and therefore many works have reported about how the size of baluns can be reduced. Among these works, the LTCC Marchand balun has been very popular.

2.2.1 Structure description

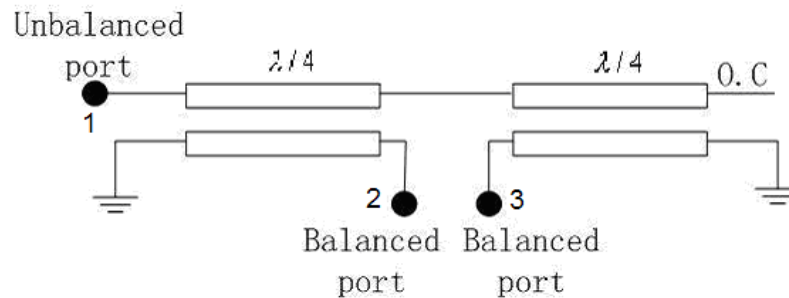


Figure 2.7: Structure of the conventional Marchand balun

Figure 2.7 shows the circuit structure of the conventional Marchand balun, which has been realized in both coaxial and planar form. It consists of two symmetrical $\lambda/4$ coupled lines. Although the Marchand balun has a simple structure, two identical $\lambda/4$ coupled lines still occupy a big area, especially at low frequencies. Using the LTCC technique, we can arrange the $\lambda/4$ coupled lines in different layers so that the size of the Marchand balun circuit can be greatly reduced.

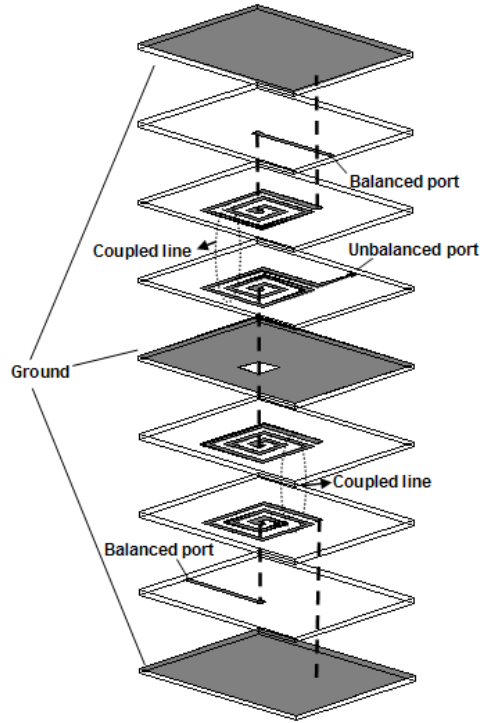


Figure 2.8: Multilayer structure of the conventional Marchand balun

Figure 2.8 shows the multilayer structure of the proposed conventional Marchand balun in LTCC. The LTCC Marchand balun comprises a laminate formed by nine dielectric substrates superimposed one on the other. Two ground electrodes are formed on a main surface of the first and the ninth dielectric substrate respectively. The structure of the balun is broadside coupled and both of the quarter wavelength coupled line sections are of meandered shape to minimize the occupied size. Since the balun structure is symmetrical, a ground plane is placed at the middle layer of the structure, separating these two coupled line sections. The three ground planes in the balun structure are connected to each other through vial holes. The central ground plane can shield the upper and lower parts from influencing each other. The connection between different layers is realized by vial holes through ceramic chip. In practice, the unbalanced and balanced ports are extended to the top layer for measurement using properly designed transmission line.

2.2.2 Design procedure

This chip-type Marchand balun was designed to operate at the central frequency of 2.4 GHz. For convenience, the unbalanced port and the balanced port impedances were all set to be 50Ω. The design procedures are as follows. Firstly, referring to [17], design parameters were chosen: $Z_a=Z_b=Z_0=50 \Omega$, $Z_{0e}=96.55 \Omega$ and $Z_{0o}=25.89 \Omega$ ($Z_{0e} \cdot Z_{0o}=Z_0^2$). Therefore, the $\lambda/4$ coupled-line acts as a -4.77 dB directional coupler. Here, it should be noted that the conclusion in [17] is not a necessary condition for the conventional Marchand balun design. In the next chapter, the close-form Marchand balun design condition will be discussed. Accordingly, the physical dimensions of the coupled line sections can be determined. To validate design procedure, simulation had been done for the $\lambda/4$ coupled-line section with the aid of EM simulation software IE3D. Figure 2.9 shows the simulated performance of a single section of $\lambda/4$ coupled-line employed in our conventional Marchand balun design, where port 1 is the input port, port 2 is the through port, port 3 is the coupled port and port 4 is the isolation port.

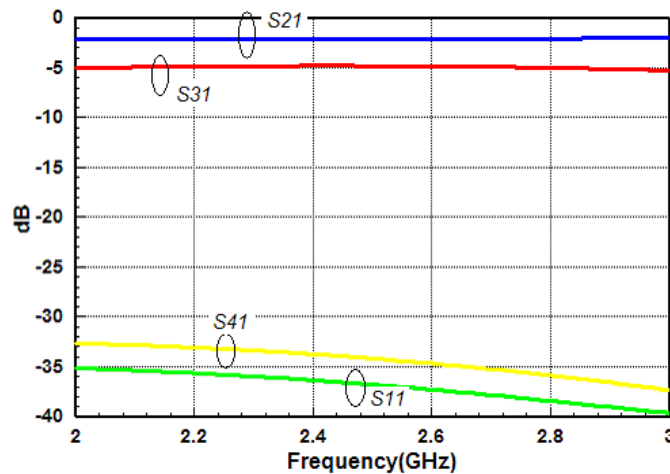


Figure 2.9: Performance of a single section of $\lambda/4$ coupled-line

Secondly, we combined two of these coupled line sections together to form a Marchand balun. Then, simulation is carried out with the aid of commercial simulation software IE3D. Finally, fine tuning is done to optimize performance. The final physical dimensions of this Marchand balun, designed to operate at 2.4 GHz, are given in Appendix I (pp.117-120). The fabricated prototype of the LTCC Marchand balun is shown in Figure 2.10.

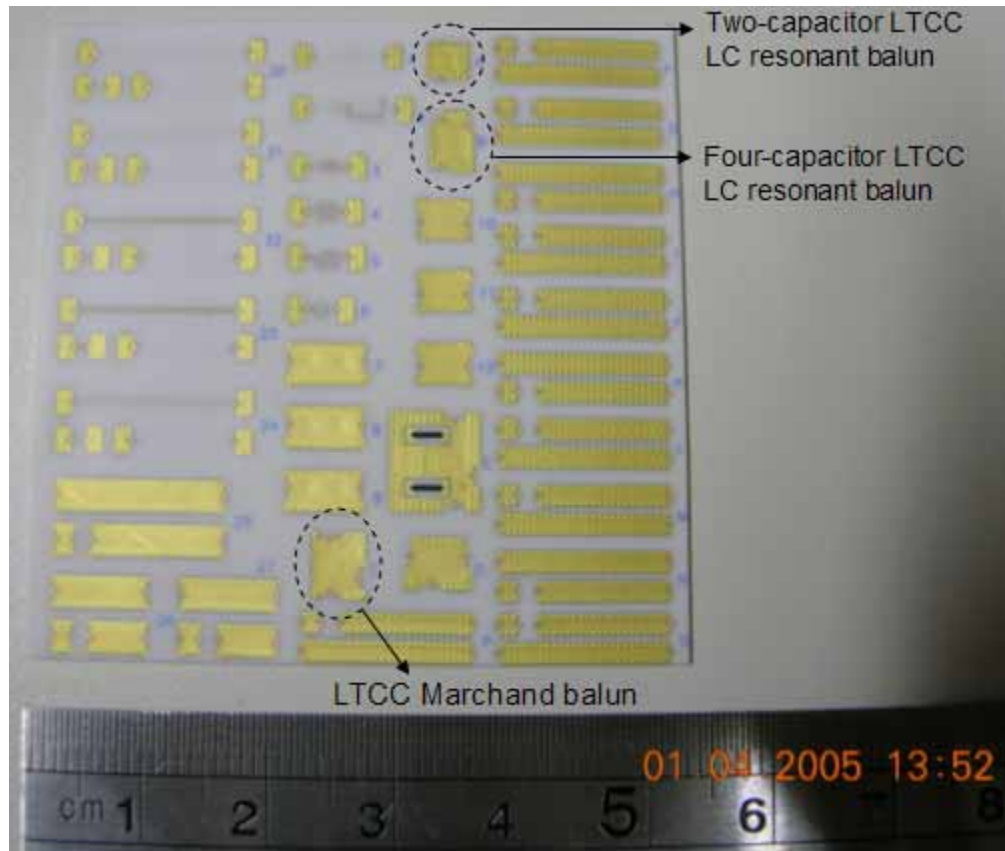
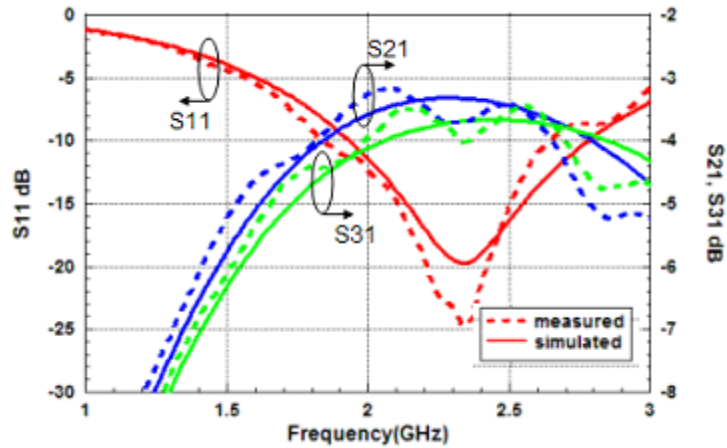


Figure 2.10: Photograph of the fabricated LTCC board

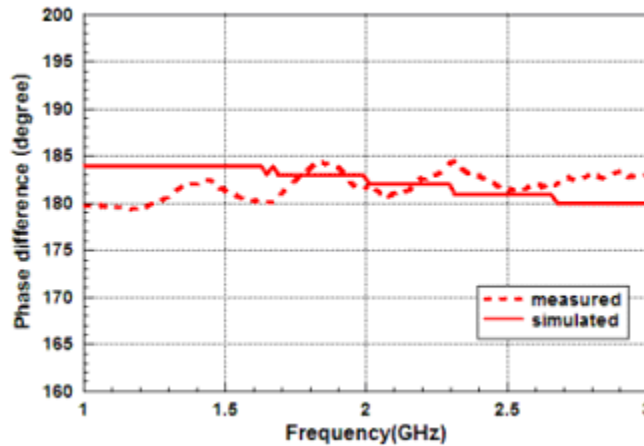
2.2.3 Simulation and measurement results

Figures 2.11 (a) and (b) display the simulated and measured results of amplitude response and phase balance of the proposed Marchand balun. The conventional LTCC chip balun was simulated using Ansoft HFSS. The measurement was carried out on the HP8510C vector

network analyzer. It is observed that good agreement is achieved between measurement and simulation. The measured return loss is found to be better than -15 dB from 2.1 GHz to 2.5 GHz and better than -10 dB over the frequency band from 1.8 GHz to 2.7 GHz, or around 40% bandwidth. The measured amplitude and phase imbalance between balanced output ports are within 1 dB and 4° , respectively, over the operating frequency band.



(a) Amplitude response



(b) Phase difference of the two balanced ports

Figure 2.11: S-parameters of the LTCC chip Marchand Balun

Although the application of spiral coupled line can reduce the size occupation, it will also affect the bandwidth performance of the Marchand balun. Figure 2.12 shows the simulated

amplitude response of a non-spiraled LTCC Marchand balun. From 2.12, it can be observed that the -10 dB bandwidth can be obtained from 1.85-3 GHz, or around 45% bandwidth, which is slightly wider than spiraled LTCC Marchand balun.

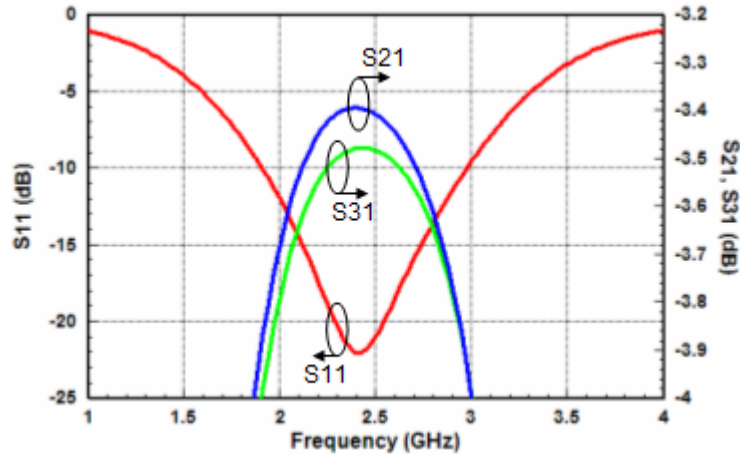


Figure 2.12: Simulated amplitude response of a non-spiraled LTCC Marchand balun

2.3 A LTCC Full-matching Marchand balun

As a three-port lossless network, the conventional Marchand baluns can not be matched simultaneously at all ports. However, the issue of balun output matching and isolation should be considered since good performance of the output port matching and isolation can greatly improve circuit performance. For example, in double-balanced mixers, isolation between LO and RF ports relates to noise suppression, and output matching can improve conversion loss and minimize interference at the output side.

2.3.1 Structure of the full matching Marchand balun

To achieve full matching at three ports of Marchand baluns, an additional lossy network is properly designed and cascaded to the original circuit [17]. Figure 2.13 shows the schematic

diagram of the perfectly matched Marchand balun. The additional lossy network is connected between two balanced ports. It consists of a section of half wavelength transmission line and two identical resistors at both ends of the transmission line. The value of the resistors is $2Z_b$, and the characteristic impedance of the half wavelength line should be as high as possible.

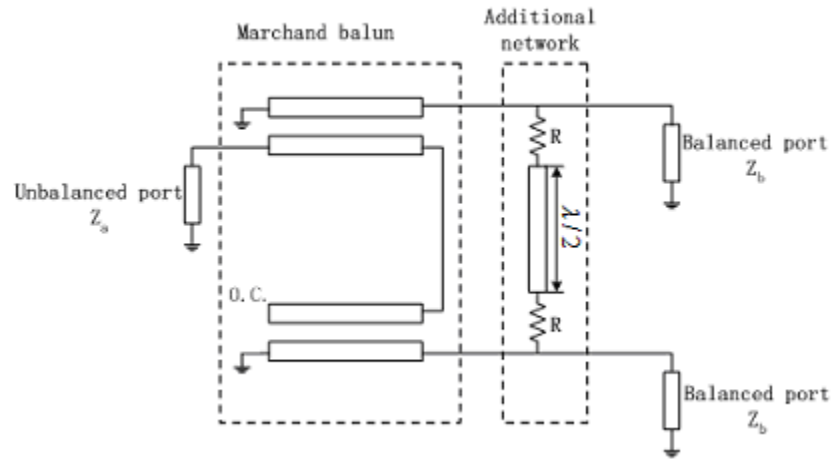


Figure 2.13: Schematic diagram of the full matching Marchand balun

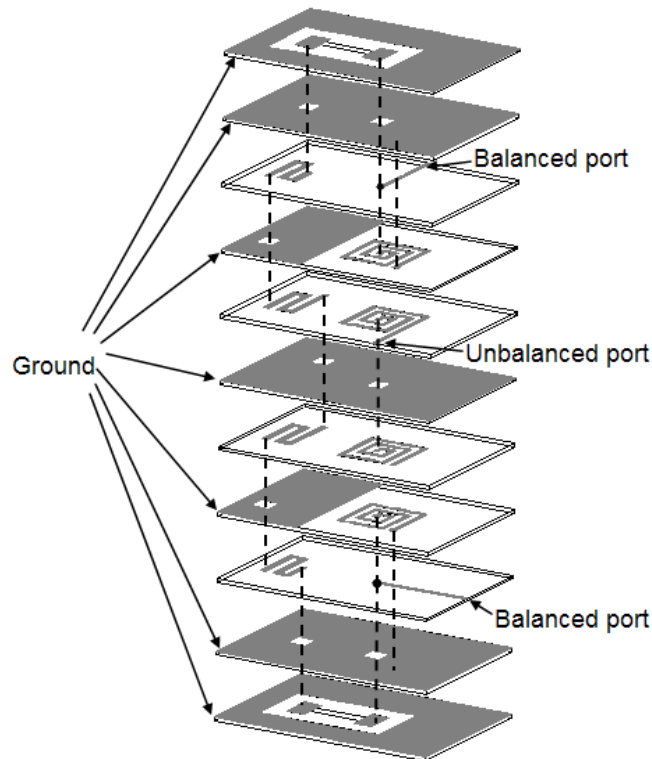


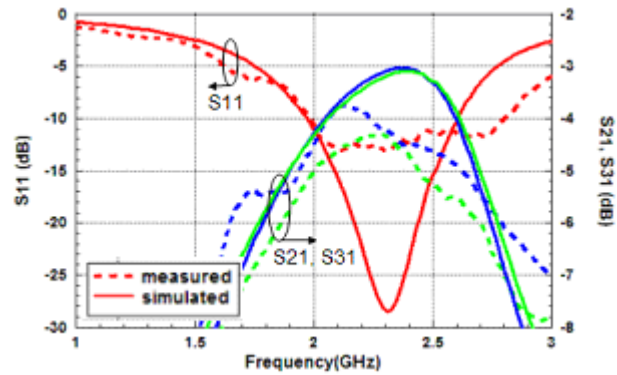
Figure 2.14: Perfectly matched Marchand balun in LTCC

Figure 2.14 shows the multilayer structure of a perfectly matched Marchand balun. Compared to the conventional Marchand balun multilayer structure described in the preceding section, the difference lies mainly on how the additional resistance network is arranged. Taking size occupation into consideration, the half wavelength transmission line of the resistance network is shaped into a meander and realized in several layers. To eliminate the interference between transmission lines on different layers, metallic materials are formed on the middle layer to separate them from each other. Via holes are used to connect these metallic planes to the main surfaces on the top and bottom layers. In addition, according to the LTCC design guide [18], either buried or surface resistors can be used in LTCC circuits. The tolerance of buried resistors is about 30% and only 5% for surface resistors. In this design, two surface resistors are chosen to obtain good tolerance, and these two surface resistors are mounted on the main surface of the top and bottom layer respectively.

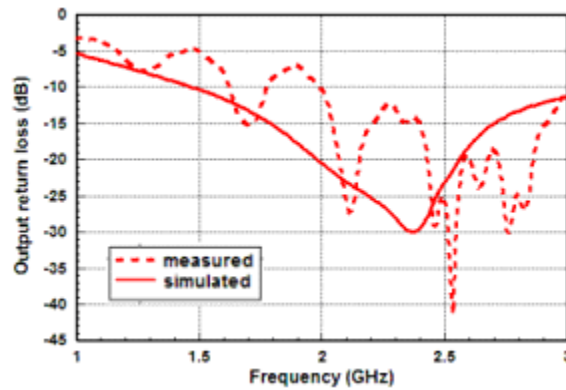
2.3.2 Design example

This chip-type perfectly matched Marchand balun has been designed to operate at the central frequency of 2.4 GHz. The unbalanced port and the balanced port impedances were all set to be 50 Ω . The design structure was realized in a 14-layer LTCC ceramic substrate, which means fifteen metallic layers. The design procedures are as follows. Firstly, a well designed 2.4 GHz conventional Marchand balun was realized in the LTCC substrate. Then, a section of meandered half wavelength transmission line was designed. Since the turns on the transmission line will affect its performance, the exact $\lambda/2$ wavelength is hard to control. Ansoft simulation software HFSS was used to aid the design. At central frequency 2.4 GHz, the phase shift from one end to the other is 180°, which means half wavelength. The final

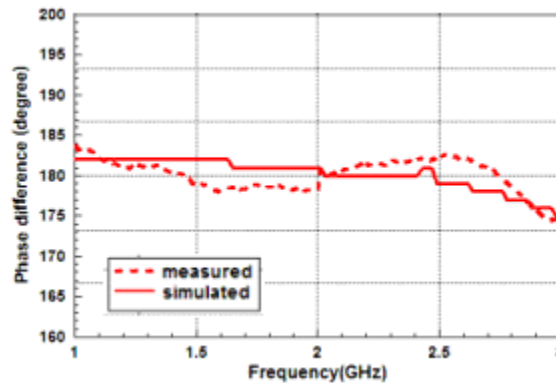
to 2.8 GHz, or around 33% bandwidth. The output return loss is better than -10 dB across the operating band. The measured amplitude and phase imbalance between balanced output ports are within 1 dB and $\pm 2^\circ$, respectively, over the operating frequency band.



(a) Input return loss and insertion loss response



(b) Output return loss



(c) Phase difference

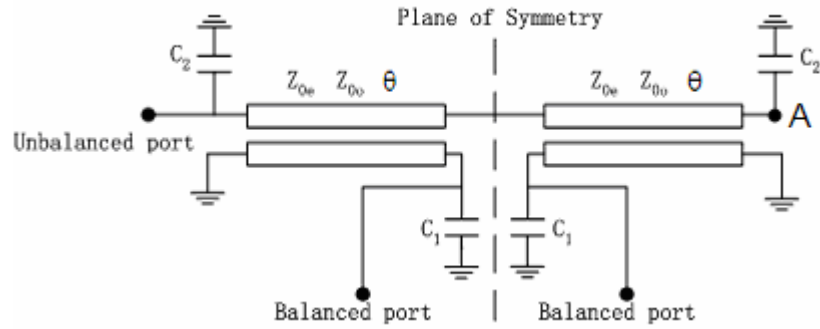
Figure 2.16: S parameter responses of the LTCC full-matching Marchand balun

2.4 LTCC size-reduced balun realized by LC resonanced method

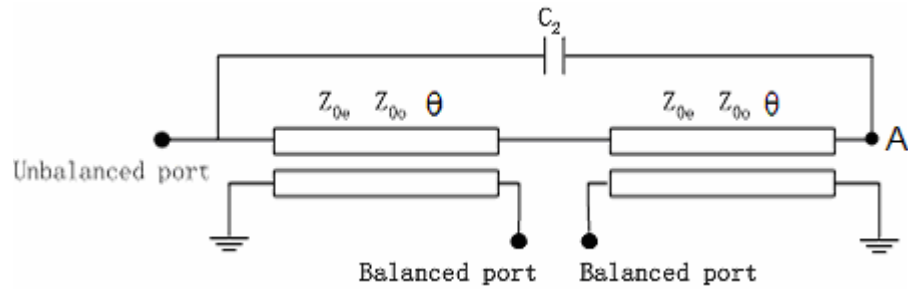
Although conventional Marchand baluns have a fairly large bandwidth, good phase difference and power distribution, they consist of two sections of $\lambda/4$ coupled lines which are relatively large in size. In the previous section, we have discussed the means to reduce the size of the Marchand balun using the LTCC technique. On the other hand, other methods have been developed to further reduce the size of the Marchand balun. In the prior arts, several balun structures employing both lumped and distributed elements have been reported [19-22]. The employment of the lumped elements can reduce the coupled-line lengths much less than a quarter wavelength. In the Tang and Chang's work [20, 21], as shown in Figures 2.17(a) and (b), the balun circuits were designed without design guide. No design data are available. In this section, the baluns, as shown in Figs 2.17(a) and (b), will be analyzed based on the even- and odd-mode method. Moreover, Ang et al. also introduced an LC resonance balun structure in [22]. The schematic diagram of the balun is shown in Figure 2.17(c), where the point A can be either a short circuit or an open circuit. For the first time, Ang et al. utilized even-odd mode analysis to solve the LC resonance balun structure as proposed in Figure 2.17(c). However, only the case of point A being a short circuit has been analyzed. Herein, the case of point A being an open circuit will be analyzed. Design curves in LTCC will be generated and plotted. Note that Figure 2.17(b) is a special case of Figure 2.17(c) with $C_1=0$ and point A an open circuit.

For the balun in Figure 2.17(a), four shunt capacitors are employed to reduce the balun size. It is observed that the balun has a symmetrical structure. The even- and odd- mode analysis technique can be used to analyze this structure. Figure 2.18 shows the corresponding even-

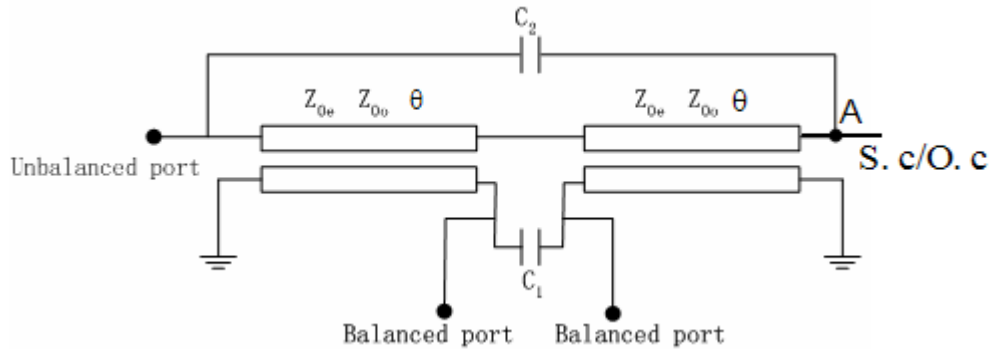
and odd-mode circuits. For the even-mode circuit, the plane of symmetry becomes a magnetic wall, which means an open circuit. For the odd-mode circuit, the plane of symmetry becomes an electrical wall, which means a short circuit.



(a) Schematic diagram of a balun proposed by Tang and Chang



(b) Schematic diagram of another balun proposed by Tang and Chang



(c) Schematic diagram of a balun proposed by Ang et al.

Figure 2.17: Several LC resonated balun structures proposed in prior arts

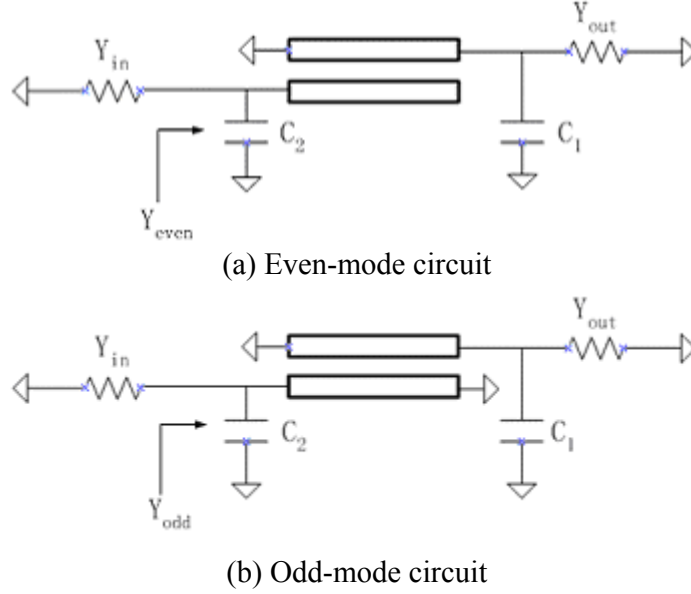


Figure 2.18: Circuit analysis of the balun in Figure 2.17(a)

The input admittances of even- and odd-mode in Figure 2.18 can be derived:

$$Y_{\text{even}} = \frac{(2\omega C_2 \cdot \cos \theta + (Y_{0e} + Y_{0o}) \cdot \sin \theta) \cdot (-2jY_{0e} Y_{0o} \cos \theta + (Y_{0e} + Y_{0o}) \cdot (j\omega C_1 + Y_{\text{out}}) \cdot \sin \theta)}{2 \sin \theta \cos \theta \cdot ((Y_{0e} + Y_{0o}) \cdot (\omega C_1 - jY_{\text{out}}) - 2Y_{0e} Y_{0o} \cot \theta)} \quad (2.1a)$$

$$Y_{\text{odd}} = j\omega C_2 - \frac{1}{2} j(Y_{0e} + Y_{0o}) \csc \theta \sec \theta - \frac{(Y_{0e} - Y_{0o})^2 \csc^2 \theta}{-4(j\omega C_1 + Y_{\text{out}}) + 2j(Y_{0e} + Y_{0o}) \csc \theta \sec \theta} \quad (2.1b)$$

where θ , Y_{0e} and Y_{0o} stand for the electrical length, the even and odd mode admittances of the coupled line section, respectively.

$$\frac{1}{Y_{\text{even}}} + \frac{1}{Y_{\text{odd}}} = \frac{2}{Y_{\text{in}}} \quad (2.2)$$

For point A in Figure 2.17(a) is an open circuit, equation 2.2 is the design condition [22]. By substituting (2.1a) and (2.1b) into (2.2), an equation with a real part and an imaginary part is generated. By equating these two parts, the following equations can be obtained.

For the real part:

$$16 \cdot Y_{out}^2 \cdot (\omega C_2 - 0.5(Y_{0e} + Y_{0o}) \cdot \cot\theta)^2 - 2(Y_{0e} - Y_{0o})^2 \cdot Y_{in} \cdot Y_{out} \cdot \csc^2\theta + \{(2\omega C_2 - (Y_{0e} + Y_{0o}) \cdot \cot\theta) \cdot (-2\omega C_1 + (Y_{0e} + Y_{0o}) \cdot \cot\theta) + ((Y_{0e} - Y_{0o}) \cdot \csc\theta)^2\}^2 = 0 \quad (2.3a)$$

For the imaginary part:

$$\begin{aligned} & -2 \cdot \cos\theta \cdot (16 \cdot Y_{out}^2 \cdot (\omega C_2 - 0.5(Y_{0e} + Y_{0o}) \cdot \cot\theta)^2 + ((2\omega C_2 - (Y_{0e} + Y_{0o}) \cdot \cot\theta) \cdot \\ & (-2\omega C_1 + (Y_{0e} + Y_{0o}) \cdot \cot\theta) + (Y_{0e} - Y_{0o})^2 \cdot \csc^2\theta)^2 + 4 \cdot (-Y_{out}^2 \cdot (\omega C_2 - 0.5(Y_{0e} + Y_{0o}) \cdot \cot\theta) \\ & + 0.5 \cdot (-2\omega C_1 + (Y_{0e} + Y_{0o}) \cdot \cot\theta)^2 \cdot (-2\omega C_2 + (Y_{0e} + Y_{0o}) \cdot \cot\theta) \\ & + (Y_{0e} - Y_{0o})^2 \cdot (\omega C_1 - 0.5(Y_{0e} + Y_{0o}) \cdot \cot\theta) \cdot \csc^2\theta) \cdot (2\omega C_2 \cdot \cos\theta + (Y_{0e} + Y_{0o}) \cdot \sin\theta) = 0 \end{aligned} \quad (2.3b)$$

These two equations should be satisfied simultaneously. Figures 2.19 and 2.20 plot the even- and odd-mode impedances (Z_{0e} and Z_{0o}) of the coupled line for different values of ωC_1 and ωC_2 with $Y_{in} = Y_{out} = 0.02$ mhos. In Figure 2.19, the value of ωC_1 is set to 0mho and only one capacitor C_2 is employed. It can be seen that the balun can be realized by a wide range of practical values of Z_{0e} and Z_{0o} , with different values of C_2 . And the electrical length θ can vary from 20° to 70° . With an increase in the value of ωC_2 , the required values of Z_{0e} and Z_{0o} decreases, and both Z_{0e} and Z_{0o} decrease monotonically with increasing ωC_2 . The decrease is faster when θ is smaller. Figure 2.20 plots the solutions for the case when both capacitors C_1 and C_2 are employed. By solving the design equations (2.3a) and (2.3b), it can be found that C_2 is a must, and when the value of C_1 is larger than that of C_2 , there is no solution for the balun design. Moreover, the reduction of balun is largely related to the value of C_2 . The use of capacitor C_1 can make the values of even- and odd-mode impedance easier to be realized in practice. For example, for the case $\omega C_1 = 0$ mho and $\omega C_2 = 0.02$ mho, if we choose point a-a' ($\theta = 30^\circ$) in Figure 2.19 for the balun design, it requires that $Z_{0e} = 138 \Omega$ and $Z_{0o} = 22 \Omega$, which

means a big impedance ratio $\rho = \frac{Z_{0e}}{Z_{0o}} = 6.27$. However, if we keep $\omega C_2 = 0.02$ mho unchanged

and employ $\omega C_1 = 0.02$ mho, according to point b-b' ($\theta = 30^\circ$) in Figure 2.20, it requires that $Z_{0e} = 136 \Omega$ and $Z_{0o} = 38 \Omega$ which becomes easier to be realized. Since the capacitor C_1 can be removed from the balun structure, as shown in Figure 2.17(a). The even-mode and odd-mode circuits of the balun structure only with C_2 can be derived and shown in Figure 2.21, which will be used for the following comparison.

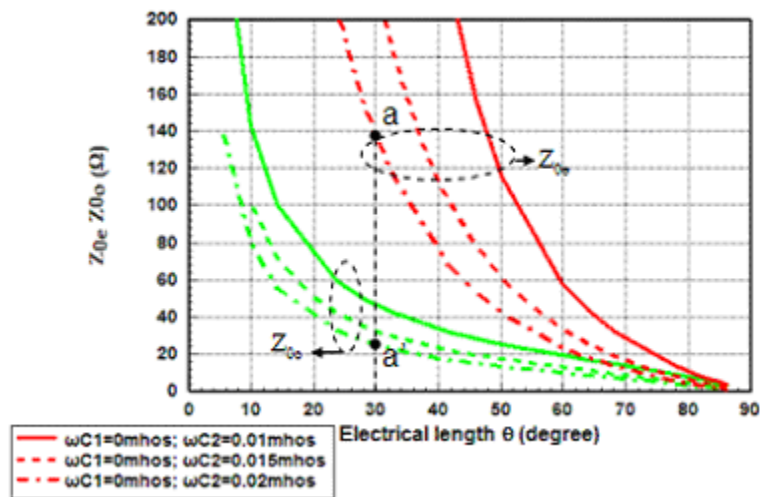


Figure 2.19: Design curves for determining Z_{0e} , Z_{0o} , and θ for various ωC_2 values with $\omega C_1 = 0$ mho and $Y_{in} = Y_{out} = 0.02$ mho.

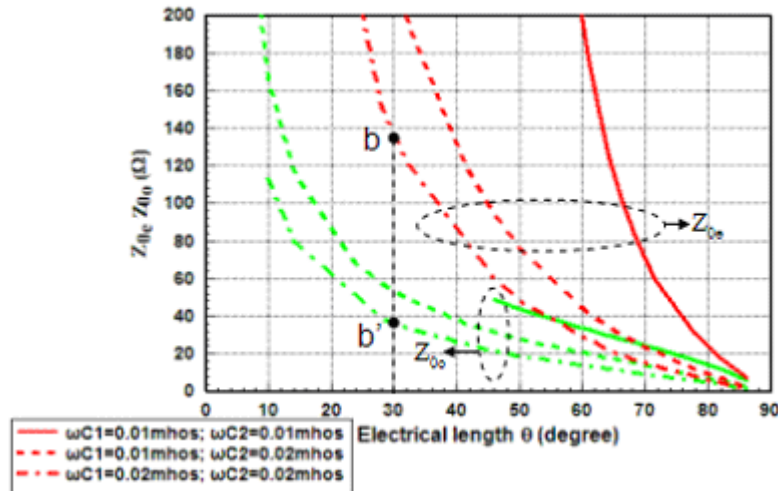


Figure 2.20: Design curves for determining Z_{0e} , Z_{0o} , and θ for various combinations of ωC_2 and ωC_1 with $Y_{in} = Y_{out} = 0.02$ mho.

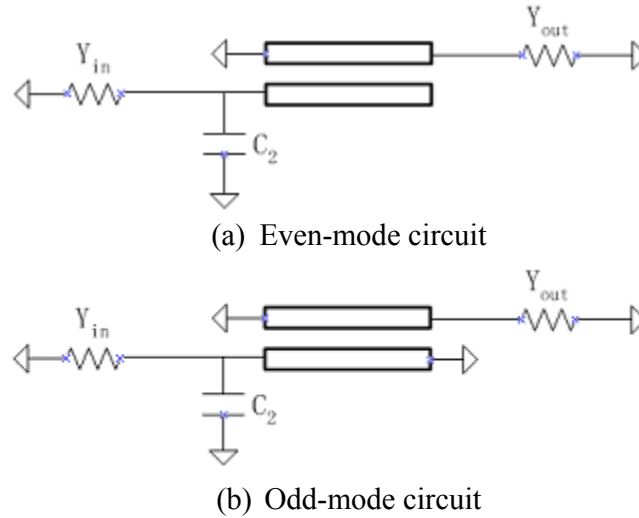


Figure 2.21: Circuit analysis of the balun shown in Figure 2.17(a) with C_1 removed

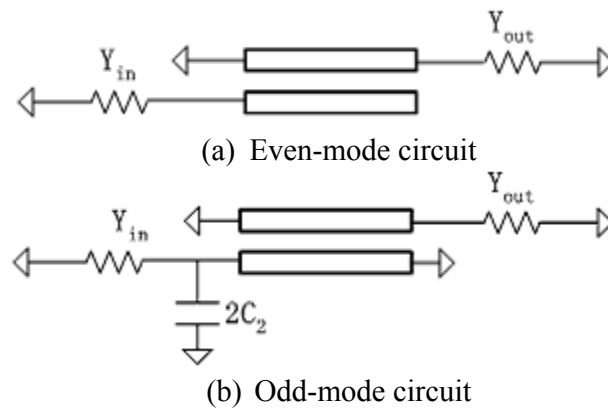


Figure 2.22: Circuit analysis of the balun structure in Figure 2.17(b)

Now, it's worth comparing this balun structure with that of Figure 2.17(b), which is another LC resonant balun structure proposed by Tang and Chang [21]. As shown in Figure 2.17(b), only a single capacitor is used in this structure. Figure 2.22 shows the corresponding even-mode and odd-mode circuits of this balun. Comparing Figure 2.22 and Figure 2.21, it is easy to find that these two structures share one common odd-mode circuit, except that the capacitor value in Figure 2.22(b) is twice that of Figure 2.21(b), which means a smaller capacitor can be used. Compared to the even-mode circuit of Figure 2.22(a), the even-mode

circuit of Figure 2.21(a) has an additional shunt capacitor. However, this capacitor is not related to size reduction because baluns are inherently even-mode blocking devices. Therefore, the balun structure described in Figure 2.17(b) is a better solution for size reduction since the capacitor with a smaller value is required.

Figure 2.17(c) shows an LC resonant balun structure proposed by Ang et al. [22]. It employs two capacitors which imply smaller circuit areas compared with the balun structures in Figures 2.17(a) and (b). Since the case for point A being a short circuit in Figure 2.17(c) has been studied by Ang et al. [22], we focus on another situation with point A being an open circuit. Likewise, the corresponding even-mode and odd-mode circuits can be derived as shown in Figure 2.23.

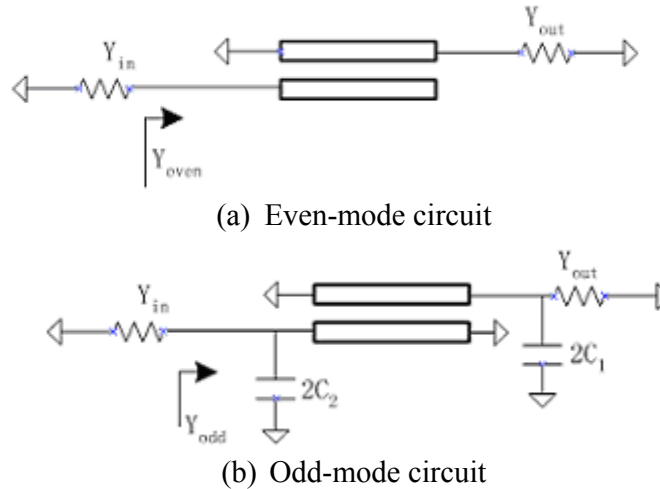


Figure 2.23: Circuit analysis of the balun in Figure 2.17(c)

The even- and odd-mode admittances in Figure 2.23 can be determined as:

$$Y_{\text{even}} = j \frac{(Y_{0e} + Y_{0o}) \tan \theta}{2} \quad (2.4a)$$

$$Y_{\text{odd}} = 2j\omega C_2 - 0.5j(Y_{0e} + Y_{0o}) \cot \theta + \frac{(Y_{0e} - Y_{0o})^2 \csc^2 \theta}{4(2j\omega C_1 + Y_{\text{out}} - 0.5j(Y_{0e} + Y_{0o}) \cot \theta)} \quad (2.4b)$$

By substituting (2.4a) and (2.4b) into $\frac{1}{Y_{\text{even}}} + \frac{1}{Y_{\text{odd}}} = \frac{2}{Y_{\text{in}}}$, we can obtain:

Real part:

$$2 \cdot (Y_{0e} - Y_{0o})^2 \cdot Y_{\text{in}} \cdot Y_{\text{out}} \cdot \csc^2 \theta - 16 Y_{\text{out}}^2 \cdot (2\omega C_2 - 0.5(Y_{0e} + Y_{0o}) \cdot \cot \theta)^2 - \{(4\omega C_2 - (Y_{0e} + Y_{0o}) \cdot \cot \theta) \cdot ((Y_{0e} + Y_{0o}) \cdot \cot \theta - 4\omega C_1) + (Y_{0e} - Y_{0o})^2 \csc^2 \theta\}^2 = 0 \quad (2.5a)$$

Imaginary part:

$$4 \cdot (Y_{0e} + Y_{0o}) \cdot (-4 \cdot Y_{\text{out}}^2 \cdot (2\omega C_2 - 0.5 \cdot (Y_{0e} + Y_{0o}) \cdot \cot \theta) + 0.5 \cdot (-4\omega C_1 + (Y_{0e} + Y_{0o}) \cdot \cot \theta)^2 \cdot (-4\omega C_2 + (Y_{0e} + Y_{0o}) \cdot \cot \theta) + (Y_{0e} - Y_{0o})^2 \cdot (2\omega C_1 - 0.5 \cdot (Y_{0e} + Y_{0o}) \cdot \cot \theta) \cdot \csc^2 \theta) - 2 \cdot \cot \theta \cdot (16 \cdot Y_{\text{out}}^2 \cdot (2\omega C_2 - 0.5 \cdot (Y_{0e} + Y_{0o}) \cdot \cot \theta)^2 + ((4\omega C_2 - (Y_{0e} + Y_{0o}) \cdot \cot \theta) \cdot (-4\omega C_1 + (Y_{0e} + Y_{0o}) \cdot \cot \theta) + (Y_{0e} - Y_{0o})^2 \cdot \csc^2 \theta)^2) = 0 \quad (2.5b)$$

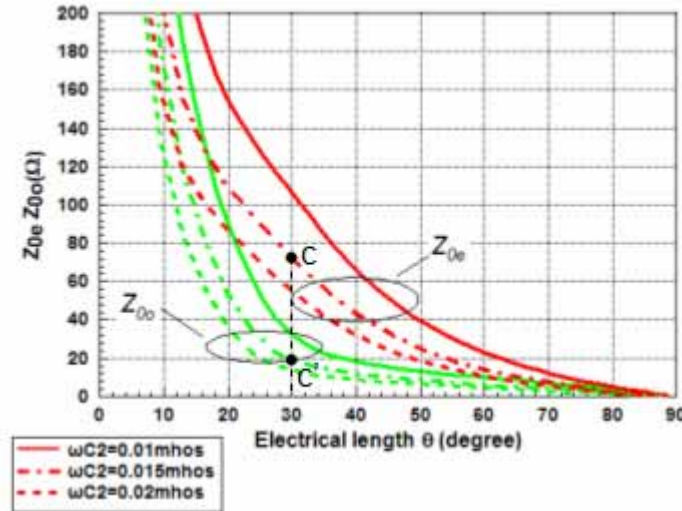


Figure 2.24: Design curves for determining Z_{0e} , Z_{0o} and θ for various ωC_2 values with $\omega C_1=0$ and $Y_{\text{in}}=Y_{\text{out}}=0.02$ mho

Solving these two equations, it can be found that in this two-capacitor lumped-distributed Marchand balun structure, C_2 is necessary for size reduction of the balun, while C_1 is optional.

Figure 2.24 exhibits the solutions for the case where only C_2 is employed. From the design

curves, it can be seen that the presence of C_2 brings a wide range of realizable values of Z_{0e} and Z_{0o} values with the electrical length θ of the coupled line θ varying from 10^0 to 70^0 . Both Z_{0e} and Z_{0o} decrease monotonically as θ increases. When θ is smaller, the slope of the decrease is steeper, and when θ gets bigger, the slope becomes smoother. Moreover, the size shrinkage of balun largely depends on the value of C_2 . With an increasing of the value of C_2 , the values of Z_{0e} and Z_{0o} reduced.

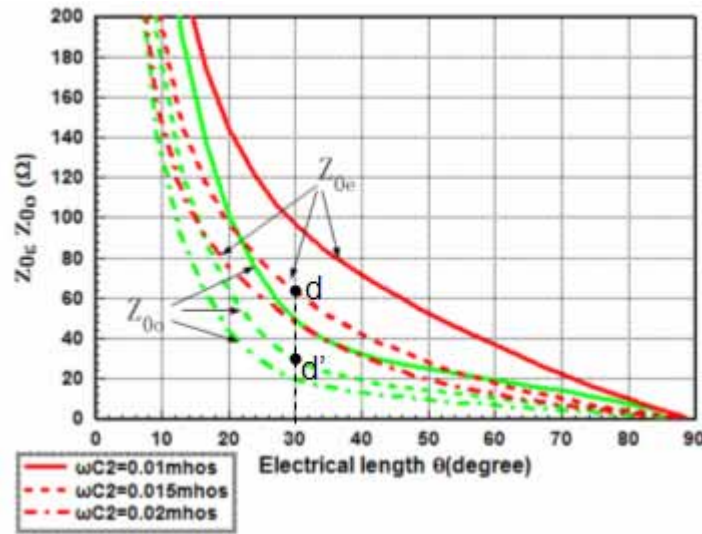


Figure 2.25: Design curves for determining Z_{0e} , Z_{0o} and θ for various ωC_2 values with $\omega C_1=0.01$ mho and $Y_{in}=Y_{out}=0.02$ mho

Figure 2.25 exhibits the solutions for the case when C_1 and C_2 are employed simultaneously. Curves are plotted for various values of ωC_2 with $\omega C_1=0.01$ mho and the port impedances being 50 ohms. Comparison between Figure 2.24 and Figure 2.25 shows that the presence of capacitor C_1 will not contribute much to the size reduction of balun. It will, however, affect the values of Z_{0e} and Z_{0o} . With the introduction of the capacitor C_1 , the values of Z_{0e} and Z_{0o} become easier to be realized in microwave circuits. For example, for the case $\omega C_1=0$ mho and $\omega C_2=0.015$ mho, if we choose point c-c' ($\theta=30^0$) in Figure 2.24 for the balun design, it requires that $Z_{0e}=73 \Omega$ and $Z_{0o}=19 \Omega$ which means an impedance ratio $\rho = \frac{Z_{0e}}{Z_{0o}} = 3.84$ is

needed. However, if we keep $\omega C_2=0.015$ mho unchanged and introduce ωC_1 with its value being 0.01 mho, according to point b-b' ($\theta=30^\circ$) in Figure 2.23, it can be seen that $Z_{0e}=63 \Omega$ and $Z_{0o}=30 \Omega$, which are easier to be realized.

2.5 Design of LTCC LC resonant balun

To demonstrate the analysis process of the LC resonant baluns, we give two design examples in this section. Both of the designs are fabricated on the FERRO A6-M ceramic with the material parameters described in Table 2.2. The capacitors in the balun structures are achieved by the LTCC embedded multilayer capacitors.

2.5.1 A four-capacitor LTCC LC resonant balun

2.5.1.1 Structure description

Figure 2.26 shows the multilayer structure of the four-capacitor LC resonant balun in Figure 2.17(a). The LTCC LC resonant balun comprises a laminate formed by seven dielectric substrates superimposed one on the other. Two ground electrodes are formed on a main surface of the first and the seventh dielectric substrate respectively. The structure of the balun is broadside coupled and both of the coupled line sections are meandered to minimize the occupied size. Since the balun structure is symmetrical, a ground plane is placed at the middle layer of the structure to separate these two coupled line sections. The three ground planes in the balun structure are connected with each other through via holes. The central ground plane can shield the upper and lower parts from the influence of each other. Short

circuits or interconnections between the metal traces of the different layers are realized using via holes.

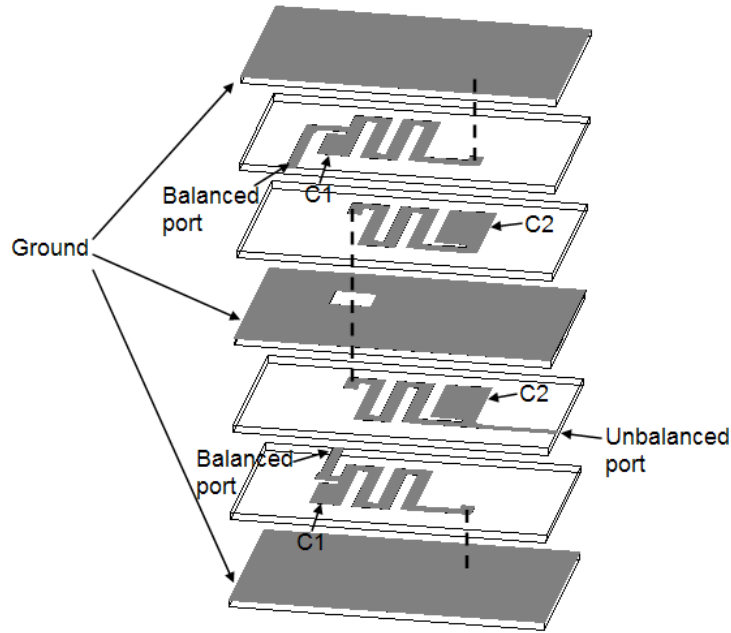


Figure 2.26: Multilayer structure of the four-capacitor LC resonant balun in Figure 2.17(a)

2.5.1.2 Design procedure

The design procedures are as follows: 1) Determine the dimensions of C_1 and C_2 according to the practical size of the LTCC chips; 2) Calculate the values of C_1 and C_2 (in our design, the values of C_1 and C_2 were obtained with the aid of IE3D); 3) According to the values of ωC_1 and ωC_2 , plot the design curve for determining Z_{0e} , Z_{0o} and θ ; 4) Choose a solution point of the design curve and determine the values of Z_{0e} , Z_{0o} and θ ; 5) According to the values of Z_{0e} , Z_{0o} and θ , determine the physical dimensions of the coupled line sections; 6) Properly arrange the layout of the balun circuit and run simulation; 7) Fine tuning may be required in obtaining the final geometry of the balun circuit. A flow diagram of the design procedure is summarized in Figure 2.27.

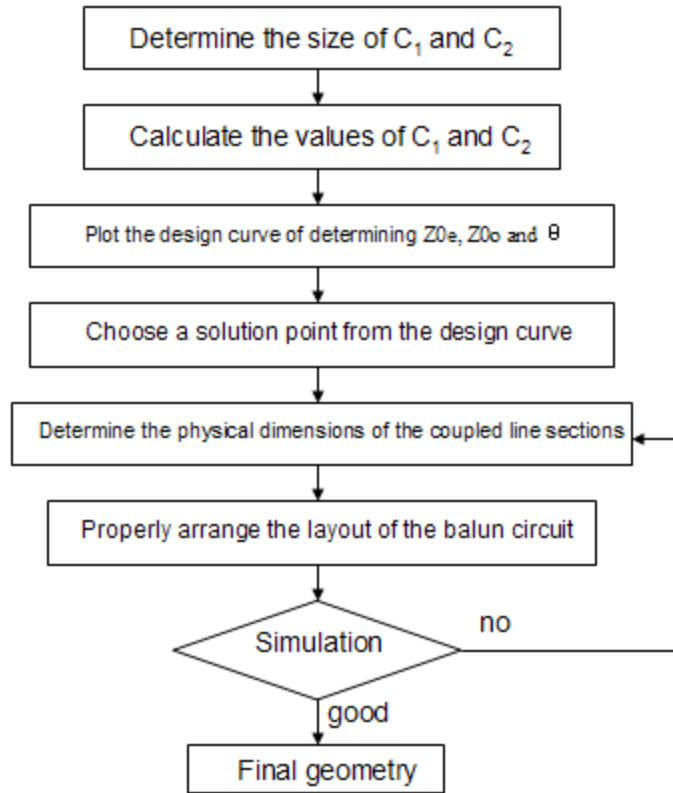


Figure 2.27: A summarized design procedure for the proposed four-capacitor LTCC chip balun

To illustrate the procedure clearly, a design example is given. This chip-type balun has been designed to operate at the central frequency of 2.4 GHz. The unbalanced input port impedance and the balanced output port impedances were all set to be 50Ω . The FERRO A6-M ceramic, with a dielectric constant of 5.9 and thickness of 3.7 mil, was used as the substrate material.

- 1) Step one: Set geometry of C_1 and C_2 to be $40 \times 20 \text{ mil}^2$ and $64 \times 30 \text{ mil}^2$, respectively.
- 2) Step two: Shunted capacitance of C_1 and C_2 are 0.51 pF and 1.11 pF or $\omega C_1 = 0.0167 \text{ mho}$ and $\omega C_2 = 0.0077 \text{ mho}$.
- 3) Step three: Plot the design curve as shown in Figure 2.28.

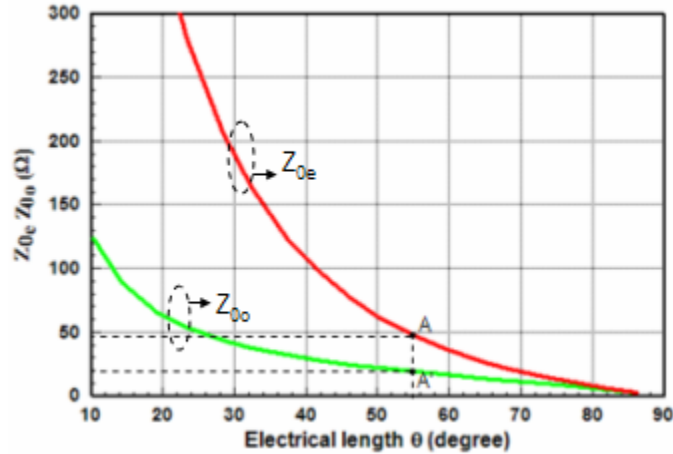


Figure 2.28: Design curves for determining Z_{0e} , Z_{0o} and θ for $\omega C_2=0.0167$ mho and $\omega C_1=0.0077$ mho with $Y_{in}=Y_{out}=0.02$ mho

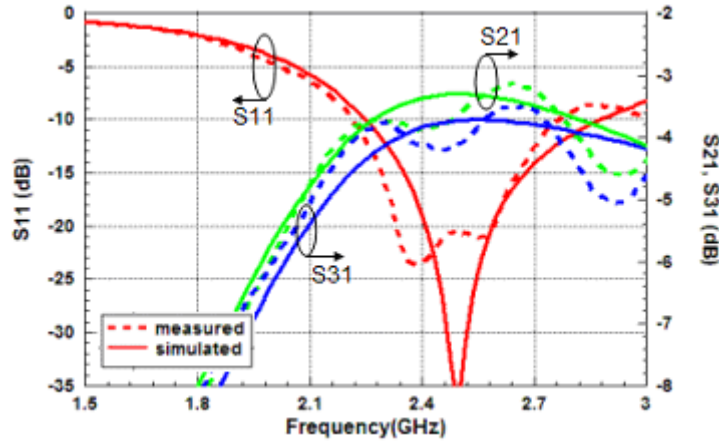
- 4) Step four: Choose A-A' as the solution point, and determine the geometry of coupled line section according to $Z_{0e}=47.0 \Omega$, $Z_{0o}=19.65 \Omega$ and $\theta=55^\circ$.
- 5) Step five: Finish the layout of the balun circuit and run simulation

The final geometry of the four-capacitor LC resonant balun is shown in Appendix I (pp.127-129).

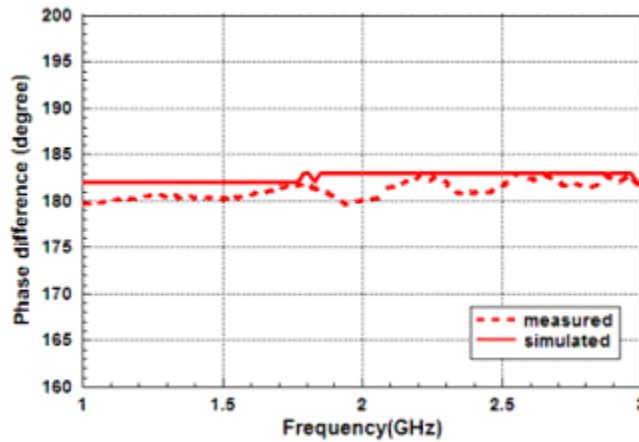
2.5.1.3 Simulation and measurement results

Figures 2.29 (a)-(b) display the simulated and measured results of amplitude responses and phase balance of the four-capacitor LC resonant balun. The balun was simulated using Ansoft HFSS. The measurement was carried out on an HP8510C vector network analyzer. It is observed that good agreement is achieved between measurement and simulation. The measured return loss is found to be better than -15 dB from 2.3 GHz to 2.65 GHz and better than -10 dB over the frequency band from 2.2 GHz to 2.75 GHz, or around 22.2% bandwidth.

The measured amplitude and phase imbalance between the balanced output ports are within 1 dB and 3° , respectively, over the operating frequency band.



(a) Amplitude response



(b) Phase difference

Figure 2.29: S parameter responses of the four-capacitor LTCC LC resonant balun

2.5.2 A two-capacitor LTCC LC resonant balun

2.5.2.1 Structure description

Figure 2.30 shows the multilayer structure of the two-capacitor LC resonant balun in Figure 2.17(c), where the point A being an open circuit. The LTCC LC resonant balun comprises a

laminates formed by seven dielectric substrates, which means seven metallic layers excluding the ground plane layers, superimposed one on the other. Two ground electrodes are formed on the surface of the first and the seventh dielectric substrate respectively. The structure of the balun is broadside coupled and both of the coupled line sections are meandered to minimize the occupied size. The two capacitors are positioned in the middle of the balun circuit in order to reduce the shunt capacitance between the ground planes. Short circuits or interconnections between the metal traces of the different layers are realized using via holes.

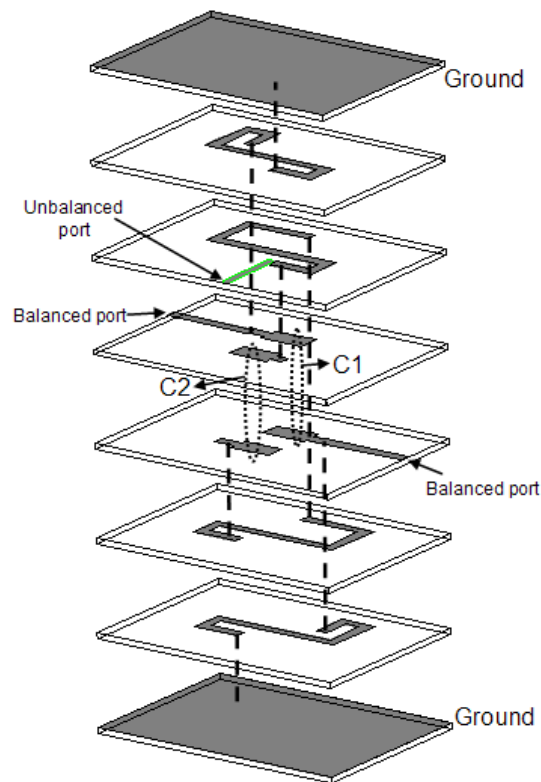


Figure 2.30: Multilayer structure of the two-capacitor LC resonant balun in Figure 2.17(c)

2.5.2.2 Design procedure

The design procedure is similar to the design of the four-capacitor chip balun described in the preceding section. To demonstrate the procedure, a design example is given. This chip-type

balun has been designed to operate at the central frequency of 2.4 GHz. The unbalanced input port impedance and the balanced output port impedances were all set to be 50 Ω . The FERRO A6-M ceramic, with a dielectric constant of 5.9 and thickness of 3.7 mil, was used as the substrate material.

- 1) Step one: Set geometry of C_1 and C_2 to be $40 \times 21 \text{ mil}^2$ and $37 \times 20 \text{ mil}^2$, respectively.
- 2) Step two: Series capacitance of C_1 and C_2 are 0.365 pF and 0.325 pF or $\omega C_1 = 0.0055 \text{ mho}$ and $\omega C_2 = 0.0049 \text{ mho}$.
- 3) Step three: Plot the design curve as shown in Figure 2.31.

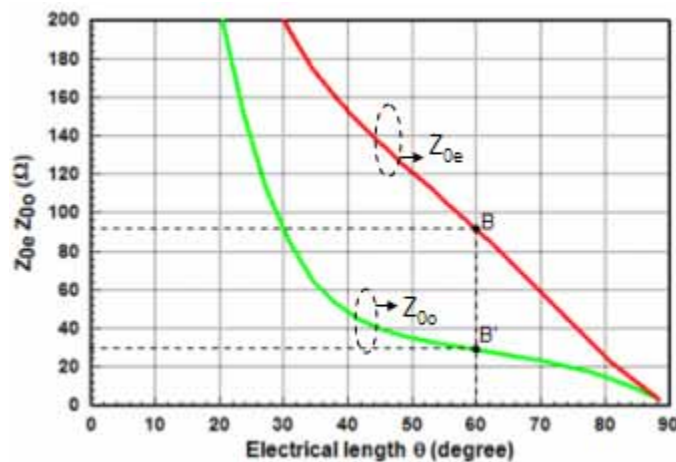
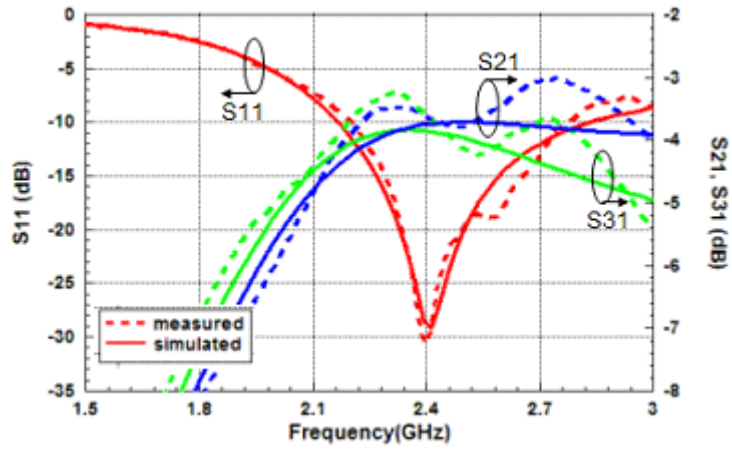


Figure 2.31: Design curves for determining Z_{0e} , Z_{0o} and θ for $\omega C_2 = 0.0055 \text{ mho}$ and $\omega C_1 = 0.0049 \text{ mho}$ with $Y_{in} = Y_{out} = 0.02 \text{ mho}$

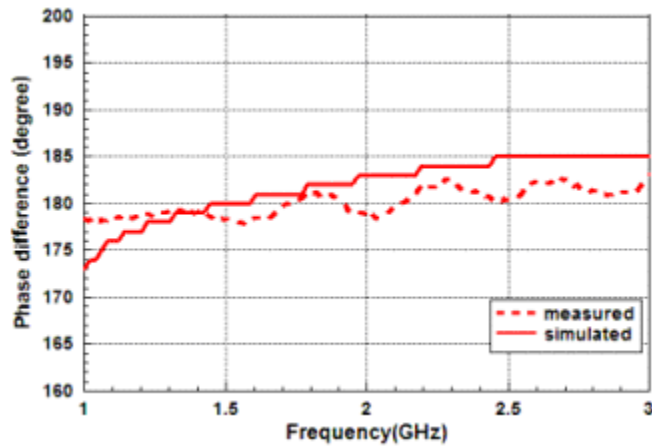
- 4) Step four: Choose B-B' as the solution point, and determine the geometry of coupled line section according to $Z_{0e} = 91 \Omega$, $Z_{0o} = 29 \Omega$, and $\theta = 60^\circ$.
- 5) Step five: Finish the layout of the balun circuit and run simulation

The final geometry of the four-capacitor LC resonant balun is shown in Appendix I (pp.130-132).

2.5.2.3 Simulation and measurement results



(a) Amplitude response



(b) Phase difference

Figure 2.32: S parameter responses of the two-capacitor LTCC LC resonant balun

Figures 2.32 (a)-(b) display the simulated and measured results of amplitude response and phase balance of the proposed two-capacitor LTCC LC resonant balun. The balun was simulated using Ansoft HFSS. The measurement was carried out on the HP8510C vector network analyzer. It is observed that good agreement is achieved between measurement and simulation. The measured return loss is found to be better than -15 dB from 2.28 GHz to 2.65 GHz and better than -10 dB over the frequency band from 2.2 GHz to 2.8 GHz, or around

24% bandwidth. The measured amplitude and phase imbalance between the balanced output ports are within 1 dB and $\pm 3^\circ$, respectively, over the operating frequency band.

2.6 Discussion and comparison

Table 2.3: Comparison between the present designs and the prior arts

Item	Bandwidth	Size(mm ²)	Number of layers
LTCC Marchand balun [16]	27.5%	3.2*1.6	8
Present design (including calibration kits)	40%	3.9*4.8	8
Four-capacitor LTCC LC resonance balun [21]	20.4%	2.0*1.2	16
Present design (including calibration kits)	22.2%	3.0*4.1	6
LTCC LC resonance balun [20]	8.2%	3.2*1.67	8
Present LTCC full-matching Marchand balun (including calibration kits)	33%	4.9*7.5	14
Present two-capacitor LTCC LC resonance balun (including calibration kits)	24%	3.0*2.7	7

It should be mentioned that the full matching balun and the two-capacitor LC resonant balun proposed in this chapter were realized with LTCC technology for the first time. Moreover, although the chip-typed conventional Marchand LTCC balun and the four-capacitor LTCC LC resonant balun have been reported, a clear design guide has not been given. In this chapter, the design guide is clearly described for the first time. The comparisons between the newly proposed LTCC baluns and the prior arts have been tabulated and summarized in Table 2.3. From Table 2.3, it can be found that, for the same kind of LTCC device, the size of the proposed LTCC baluns is comparably bigger than those of the reported ones. It is mainly attributed to the different substrate properties and restriction of fabrication tolerance. Moreover, the proposed balun devices include the calibration kits(for the purpose of

measurement) at each ports which also occupies a big area. Note that the proposed examples of the LTCC LC resonant baluns were designed to verify the analysis and not optimized for size reduction (the size of the baluns can be further reduced by choosing appropriate points along the design curves).

2.7 Conclusion

In this chapter, the Low Temperature Co-fired Ceramic (LTCC) technique has been used in the balun designs to achieve smaller size occupation. First, a conventional 2.4 GHz Marchand balun has been realized using LTCC technique. In this balun circuit, the coupled-line sections are folded into spiral form and placed in different layers so that the overall size is largely reduced. Secondly, considering the output return loss of the conventional Marchand balun is not good, a miniaturized LTCC balun, with all the three ports fully matched, has been implemented. Moreover, the LC resonanced method has been employed in the LTCC balun structures so that the size can be further reduced. Several structures were analyzed using the even-odd mode analysis method and the design curves were plotted. Finally, based on the design curves, we present two design examples in LTCC environment to demonstrate our analysis.

Chapter 3

Study and design of a Marchand balun using a patterned ground plane

Various types of baluns have been reported for applications in microwave integrated circuits (MICs) and monolithic microwave integrated circuits (MMICs) [23-31]. Among them, the planar version of the Marchand balun [27-31] is probably one of the most popular because of its ease of implementation and wide bandwidth. The planar Marchand balun consists of two sections of quarter-wave coupled lines, which may be realized using microstrip coupled lines [27], Lange coupler [28, 29], multiplayer coupler structures [30], or spiral coils [31].

A strong coupling is required for both the two coupled line sections in order to obtain a well designed Marchand balun [32]. Also, high even-mode impedances, to reject even-mode excitations, are required in Marchand baluns for broadband performance [33]. For the edge-coupling structure, the coupling factor is largely dependant on the gap between two coupled lines. For MMICs design, the gap between two coupled lines can be a few micrometers, thus such tight coupling is still achievable in the edge-coupled way [28, 29]. However, for MIC designs using the printed circuit board (PCB) fabrication technology, Marchand Baluns usually tend to choose broadside coupling lines, or multilayer structures [30, 31] to achieve

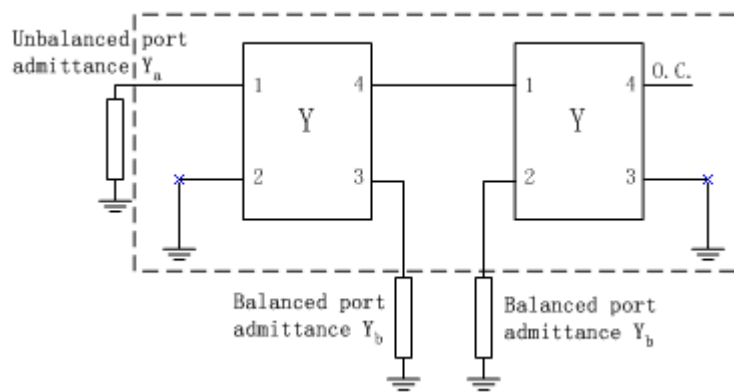
tight coupling, which is high in cost or complex in structure. Therefore, it will be very beneficial if baluns can be implemented using simple microstrip couple lines. In [33], by cascading several of single-layer microstrip coupled-line sections, very high even-mode impedances can be obtained, yielding good balun amplitude and phase balance. Furthermore, the cascading microstrip coupled-lines with a slot cut in the ground plane beneath the coupled lines were proposed to increase the even-mode impedances, and hence improve the coupled-line balun performance in [33].

In this chapter, a novel planar Marchand balun using a patterned ground plane is presented. For this new design, with the ground plane under the coupled lines removed, as in [33], the even-mode impedance will increase substantially. Meanwhile, we proposed that two additional separated rectangular conductors be placed under the coupled lines to act as two capacitors so as to decrease the odd-mode impedance. The new design is based on the concept that the even-mode impedance of a coupler is mainly related to the capacitance of the microstrip conductor to the ground plane, and the odd-mode impedance is related to the capacitance between the microstrip conductor and the ground plane as well as the capacitance between the two coupled conductors [34]. Simple design theory and design procedure are presented to optimize the designed Marchand balun. The proposed new design was simulated by the full-wave electromagnetic software Ansoft HFSS and validated by measurements. Compared with the cascading microstrip multi-section coupled-line baluns with a slot cut in the ground plane [33], our newly proposed planar Marchand balun with a patterned ground plane is small in size and has a good performance. For example, one Marchand balun on a double-sided PCB is designed, simulated, fabricated and measured. The measured return loss is found to be better than -10 dB over the frequency band from 1.2 GHz to 3.3 GHz, or around 100% bandwidth. The measured amplitude and phase imbalance between the

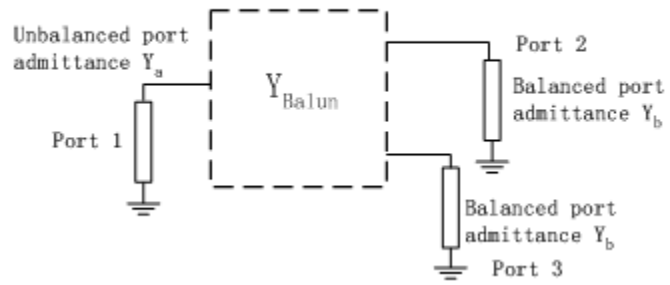
balanced output ports are within 1 dB and 4°, respectively, over the operating frequency band. In this chapter, all the fabrication works were outsourced to Shenzhen King Brother PCB Technology CO., LTD, China. More details are available in the company website www.kbpcb.com.

3.1 Theoretical analysis of the conventional Marchand baluns

With reference to the conventional Marchand balun structure described in Figure 2.6, the symmetrical $\lambda/4$ coupled line can be deemed as a four-port network [35]. Figure 3.1(a) shows the equivalent circuit of the Marchand Baluns when the coupled-line sections are replaced by their admittance matrix. The coupled-line network, enclosed by a dashed line in Figure 3.1(a), can be regarded as a three-port network with an admittance matrix Y_{Balun} , as shown in Figure 3.1(b).



(a) Original network



(b) Transformed network

Figure 3.1: Equivalent circuit of Marchand Baluns

The corresponding Y parameters expressed in terms of the even- and odd-mode characteristic admittances Y_{0e} and Y_{0o} are given as in [35]:

$$Y = \begin{bmatrix} Y_{11} & Y_{12} & Y_{13} & Y_{14} \\ Y_{21} & Y_{22} & Y_{23} & Y_{24} \\ Y_{31} & Y_{32} & Y_{33} & Y_{34} \\ Y_{41} & Y_{42} & Y_{43} & Y_{44} \end{bmatrix} \quad (3.1)$$

where

$$Y_{11}=Y_{22}=Y_{33}=Y_{44}=-j\frac{1}{2}(Y_{0e} + Y_{0o}) \cot \theta$$

$$Y_{12}=Y_{21}=Y_{43}=Y_{34}=-j\frac{1}{2}(Y_{0e} - Y_{0o}) \cot \theta$$

$$Y_{13}=Y_{31}=Y_{42}=Y_{24}=j\frac{1}{2}(Y_{0e} - Y_{0o}) \csc \theta$$

$$Y_{14}=Y_{41}=Y_{23}=Y_{32}=j\frac{1}{2}(Y_{0e} + Y_{0o}) \csc \theta$$

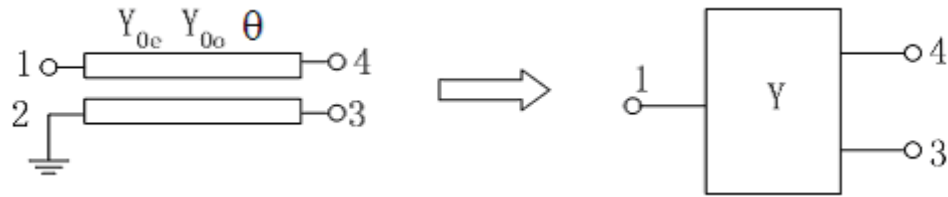


Figure 3.2: A basic element in the Marchand balun structure

The original symmetrical coupled line section is a 4-port network. When the short circuit is considered as shown in Figure 3.2, the boundary condition $U_2=0$ will be imposed on the original 4-port coupled line network,

$$I = \begin{bmatrix} Y_{11} & Y_{12} & Y_{13} & Y_{14} \\ Y_{21} & Y_{22} & Y_{23} & Y_{24} \\ Y_{31} & Y_{32} & Y_{33} & Y_{34} \\ Y_{41} & Y_{42} & Y_{43} & Y_{44} \end{bmatrix} \times U \quad (3.2)$$

the remaining 3-port is described by the following matrix equation:

$$I = \begin{bmatrix} Y_{11} & Y_{13} & Y_{14} \\ Y_{31} & Y_{33} & Y_{34} \\ Y_{41} & Y_{43} & Y_{44} \end{bmatrix} \cdot U \quad (3.3)$$

where Y_{mn} ($m, n \leq 4$) are indicated by (3.1).

Likewise, for the circuit shown in Figure 3.3, the boundary condition $U_3=0, I_4=0$ will be imposed on the original 4-port coupled line,

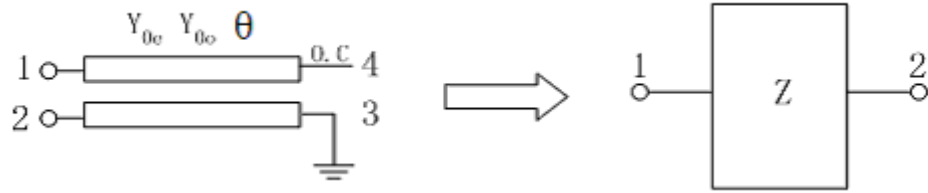


Figure 3.3: Another basic element in the Marchand balun structure

the final impedance parameters can be denoted as a 2×2 matrix

$$Z = \begin{bmatrix} Z'_{11} & Z'_{12} \\ Z'_{21} & Z'_{22} \end{bmatrix} \quad (3.4)$$

where

$$Z' = \begin{bmatrix} Z'_{11} & Z'_{12} & Z'_{13} \\ Z'_{21} & Z'_{22} & Z'_{23} \\ Z'_{31} & Z'_{32} & Z'_{33} \end{bmatrix} = \begin{bmatrix} Y_{11} & Y_{12} & Y_{14} \\ Y_{21} & Y_{22} & Y_{24} \\ Y_{41} & Y_{42} & Y_{44} \end{bmatrix}^{-1} \quad (3.5)$$

, and Y_{mn} ($m, n \leq 4$) are indicated by (3.1).

We have analyzed two element circuits which are derived from the original symmetrical coupled line section. In fact, a Marchand balun consists of these two parts with port 4 of the

first circuit and port 1 of the second circuit connected. Therefore, applying Kirchhoff's Current Law, we can derive Y_{Balun} , as defined in Figure 3.1. To get the corresponding scattering matrix of Y_{Balun} , the conversion relationship from Y matrix to S matrix will be applied:

$$S = R^{-1} \times (U - Z_g^* \times Y_{\text{Balun}}) \times (Z_g \times Y_{\text{Balun}} + U)^{-1} \times R \quad (3.6)$$

where $R = \text{diag}(\sqrt{\text{Re } Z_{gi}})$, $Z_g = \text{diag}(Z_{gi})$, Z_{gi} is the port impedance, U is the identity matrix and Z_g^* stands for the conjugate of Z_g .

With the port assignments defined in Figure 3.1(b), the S-parameters characterizing the Marchand Balun is given by (It should be noted that conventional Marchand baluns are not components matched at all the ports. In the former chapter, the method to achieve three-port matching has been discussed):

$$\begin{aligned} S_{11} &= 0; \\ S_{21} &= -S_{31} \end{aligned} \quad (3.7)$$

Substitute the obtained S parameters into the equations above, the desired design equation for Marchand Baluns is

$$((Y_{0e} - Y_{0o}) \cdot \csc \theta)^4 - 2 \cdot (Y_{0e} - Y_{0o})^2 \cdot Y_a \cdot Y_b \cdot \csc^2 \theta = 0 \quad (3.8)$$

the coupled transmission line is $\lambda/4$ in length, therefore the above equation can be simplified as:

$$\begin{aligned} Y_{0o} - Y_{0e} &= \sqrt{2Y_a Y_b} \\ \text{Or,} \quad \frac{1}{Z_{0o}} - \frac{1}{Z_{0e}} &= \sqrt{\frac{2}{Z_a Z_b}} \end{aligned} \quad (3.9)$$

Referring to equation (3.9), the desired relationship between Z_{0e} and Z_{0o} for different combinations of the input and output port impedances Z_a and Z_b , was plotted as shown in Figure 3.4. Note that for a given set of balun impedances at the input and output port impedances Z_a and Z_b , the even- and odd-mode impedances Z_{0e} and Z_{0o} of the coupled line parameters are not unique. For example, when $Z_a = Z_b = 50 \Omega$, any of the combinations shown in Table 3.1 will fulfill the desired design equation (3.9) for achieving a well-matched Marchand balun, where ρ stands for the even- and odd-mode impedance ratio.

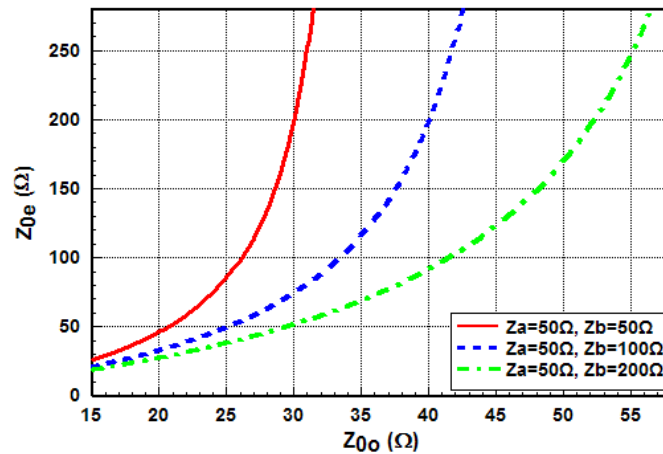


Figure 3.4: Even- mode impedance Z_{0e} versus odd- mode impedance Z_{0o} with various port impedances

Table 3.1: Choice of Z_{0e} and Z_{0o} for $Z_a=Z_b=50 \Omega$

$Z_{0e} (\Omega)$	$Z_{0o} (\Omega)$	ρ
89	25.3	3.52
158	28.9	5.47
260	31.1	8.36

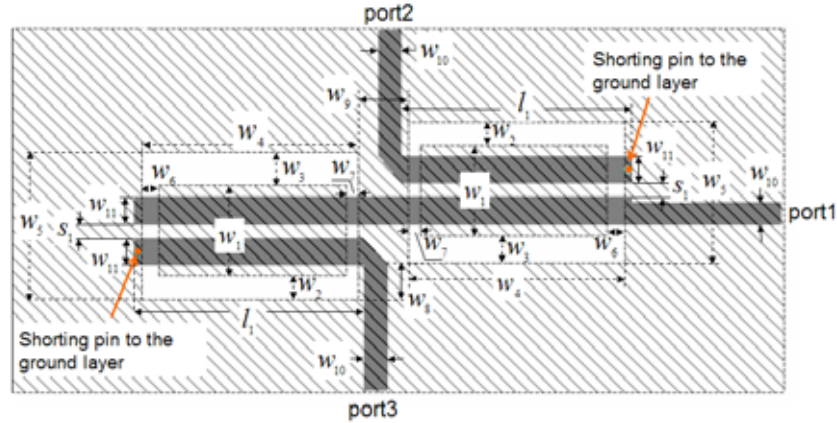
3.2 Improved Planar Marchand Baluns Using A Patterned Ground Plane

In this section, a novel planar Marchand balun using a patterned ground plane is presented. The new design is based on the concept that the even-mode impedance of a coupler is mainly related to the capacitance of the microstrip conductor to the ground plane, and odd-mode impedance is related to the capacitance between the microstrip conductor and the ground plane as well as the capacitance between the two coupled conductors [34]. In this new design, with the ground plane under the coupled lines removed, as in [33], the even-mode capacitance would decrease substantially. Meanwhile, two additional separated rectangular conductors are placed under the coupled lines to act as two capacitors so that the odd-mode capacitance would increase. As such, a well-matched Marchand balun on a double-sided PCB is achieved. The proposed new design was simulated by the full-wave electromagnetic software Ansoft HFSS and validated by measurement.

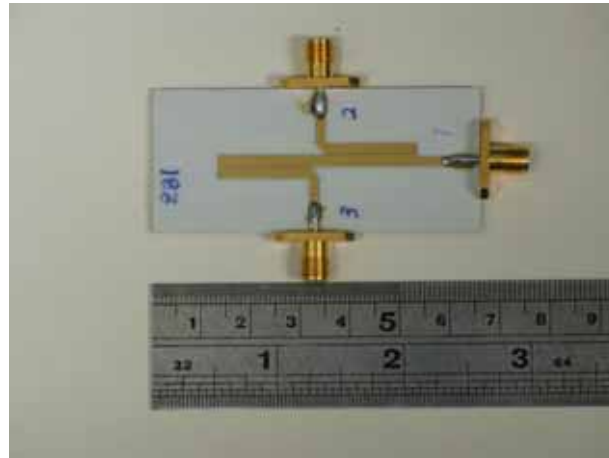
3.2.1 Structure Description

From the analysis in the previous section, we learn that a large impedance ratio between the even- and odd- mode impedances of the coupled-line sections is required. For the Marchand balun design on one single layer and single side PCB, such a high impedance ratio is hard to achieve. On the other hand, as we know, the even-mode impedance of a coupler is mainly related to the capacitance of the microstrip conductor to the ground plane, and the odd-mode impedance is related to the capacitance between the microstrip conductor and the ground plane as well as the capacitance between the two coupled conductors. Therefore, we can

deduce that the major challenge in edge-coupled Marchand balun designs lies in finding the means to decrease the even-mode capacitance and increase the odd-mode capacitance.



(a) Layout schematics



(b) Photograph of the prototype

Figure 3.5: New Planar Marchand Balun Using A Patterned Ground Plane

$w_1 = 4.65$ mm, $w_2 = 3$ mm, $w_3 = 4$ mm, $w_4 = 17.4$ mm, $w_5 = 11.65$ mm, $w_6 = 0.9$ mm, $w_7 = 0.5$ mm, $w_8 = 2$ mm, $w_9 = 4$ mm, $w_{10} = 1.86$ mm, $w_{11} = 2.2$ mm, $l_1 = 18.5$ mm, and $s_1 = 0.15$ mm

In our new design, we have demonstrated that not only has the even-mode impedance increased, the odd-mode impedance has also decreased. Figure 3.5(a) shows the new Marchand balun. The grey area stands for the metallization on the front side of the PCB, and the dashed line area stands for the metallization on the bottom side of the PCB. In this

improved Marchand balun structure, a patterned ground plane is used. With a slot under the coupled lines cut on the ground plane, both the even-mode capacitance and the odd-mode capacitance of the coupled lines would decrease substantially. However, the decrease in the even-mode capacitance is at a much faster rate than that of the odd-mode capacitance. Meanwhile, two additional separated rectangular conductors are placed under the coupled lines to act as two capacitors so that the odd-mode capacitance is increased. Therefore, a large impedance ratio between the even- and odd-mode impedances can be attained.

3.2.2 Design procedure

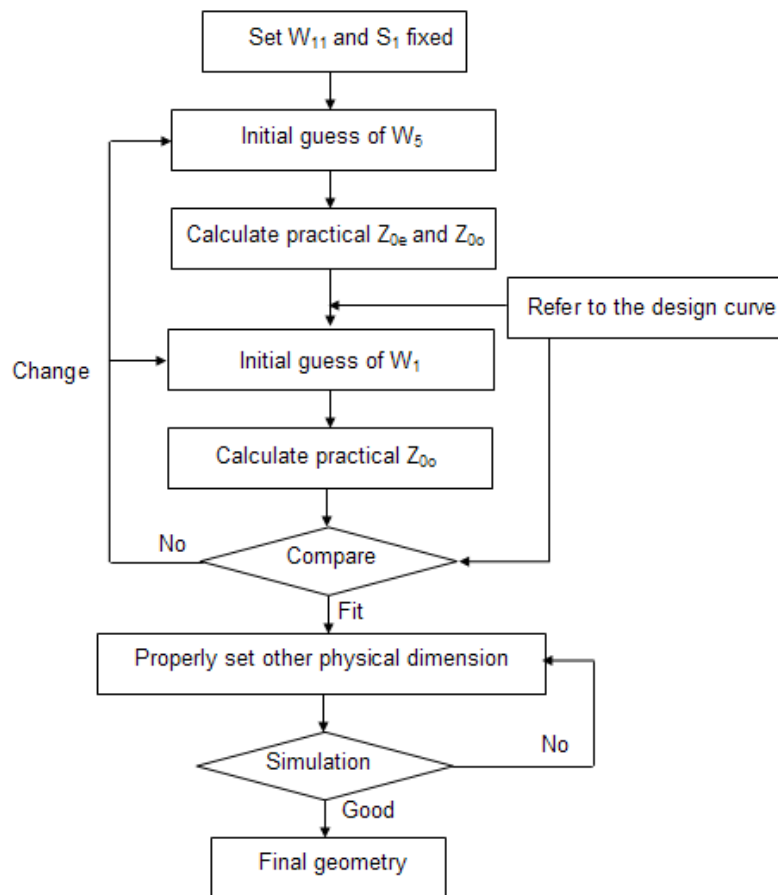


Figure 3.6: A summarized design procedure for the proposed Marchand balun

The physical sizes of the proposed Marchand balun were determined through an optimization procedure. The optimization was carried out with the aid of theoretically calculated values of Z_{0e} and Z_{0o} as in Figure 3.4. There are four key parameters which are related to the values of Z_{0e} and Z_{0o} . These parameters are the width W_{11} of the coupled lines, the line spacing S_1 between the coupled lines, the width W_5 of the slots beneath the coupled lines and the width W_1 of the conductors located under the coupled lines. For convenience, the width and line spacing of the coupled lines are fixed. A flow diagram of the design procedure is summarized in Figure 3.6.

To illustrate the procedure clearly, a Marchand balun design example is given in Figure 3.5(a). The balun was designed on the microwave substrate RO4003 having thickness 0.8 mm and dielectric constant $\epsilon_r = 3.38$. Referring to the equation (3.9), the Marchand balun can be designed as an impedance transforming devices. In our design, for convenience in measurement, all the balanced and unbalanced ports impedances were assumed to be 50Ω . In Figure 3.7, a design procedure is illustrated for this Marchand balun design.

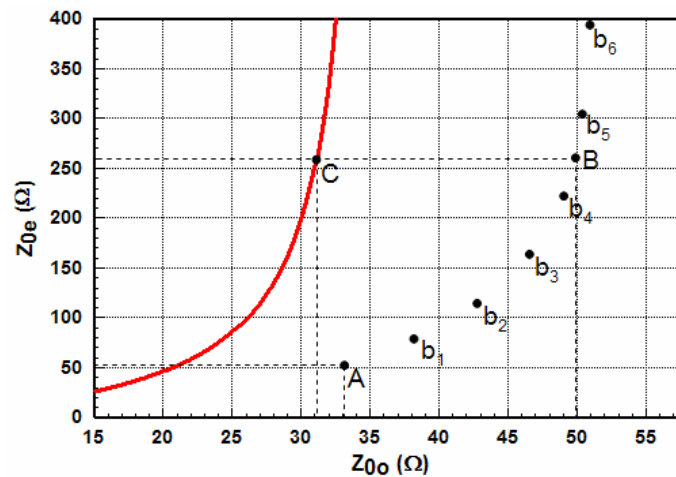


Figure 3.7: Even- mode impedance Z_{0e} versus odd- mode impedance Z_{0o} in the design procedure for the Marchand balun in Figure 3.6(a), $Z_a = Z_b = 50 \Omega$

The solid line stands for the desired relationship between Z_{0e} and Z_{0o} for a well matched Marchand balun for $Z_a = Z_b = 50 \Omega$. Firstly, the coupled lines were set 2.2 mm in width; and in accordance to the PCB fabrication capability, the gap between the coupled lines was set as 0.15 mm. At this stage, with a perfect ground plane under the coupled lines, the even- and odd-mode impedances of the coupled lines could be determined as $Z_{0e} = 52.5 \Omega$ and $Z_{0o} = 33.1 \Omega$, which locate at point A in Figure 3.7. Then a slot was cut on the ground plane beneath the coupled lines to increase the value of Z_{0e} . The dots ($b_1, b_2, b_3, b_4, B, b_5, b_6$) denote the trace of Z_{0e} and Z_{0o} as the width W_5 of the slot varies.

For this movement from b_1 to b_6 as in Figure 3.7, it is observed that a larger slot width will produce higher even-mode impedance. However, a wider slot in the ground plane may require a large sized PCB. In this demonstrated design example, point B is chosen with W_5 being 12.65 mm where $Z_{0e} = 260 \Omega$ and $Z_{0o} = 49.9 \Omega$. From Figure 3.7, Z_{0o} is too big to meet the requirement of a matched Marchand balun. Two additional conductors are then placed under the coupled lines to decrease Z_{0o} but this will not have much effect on the value of Z_{0e} . The dots c_1 and c_2 between point B and C denote the trace of Z_{0e} and Z_{0o} as the width of the additional conductors W_1 varies. One well-matched Marchand balun can be achieved with the dimensions at the point C which locates on the solid line of Figure 3.7 with $Z_{0e} = 260 \Omega$ and $Z_{0o} = 31.1 \Omega$. Table 3.2 shows the relationship between the even- and odd-mode impedances Z_{0e} and Z_{0o} and the physical dimensions of the coupled lines with a patterned ground plane during the above process from point A to C.

Table 3.2: Relationship between the even- and odd-mode impedances Z_{0e} and Z_{0o} and the physical dimensions of the coupled lines with a patterned ground plane as in Figure 3.6(a)

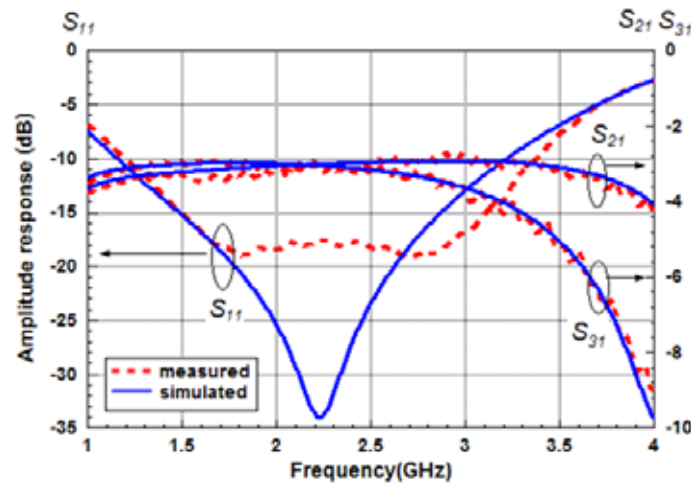
Trace point	$W_5(\text{mm})$	$W_1(\text{mm})$	$Z_{0e}(\Omega)$	$Z_{0o}(\Omega)$
A	--	--	52.5	33.1
b_1	2.75	--	81.3	38.2
b_2	4.65	--	115	42.8
b_3	6.65	--	164	46.7
b_4	9.65	--	223	49.1
B	12.65	--	260	49.9
b_5	14.65	--	305	50.3
b_6	18.65	--	395	51
c_1	12.65	2.35	260	43.1
c_2	12.65	3.35	260	37.2
C	12.65	4.65	260	31.1

Moreover, considering the change in the even-mode and odd-mode capacitances and the fringing effects of the coupled lines, the length of the coupled line is a little less than one quarter wavelength. For this design, with a center operating frequency of 2.2 GHz, the length of the coupled lines is 18.5 mm. The short circuit is attained through via holes connected to the ground. More dimensions for the balun are displayed at the figure caption of Figure 3.5(a). Figure 3.5(b) shows the photograph of the fabricated prototype.

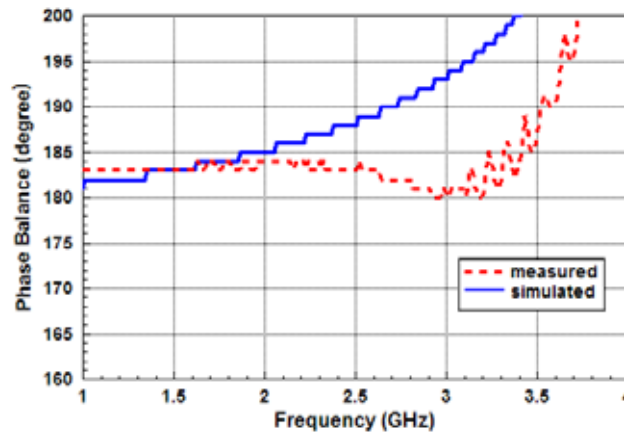
3.2.3 Results and Discussions

Figures 3.8 (a) and (b) display the simulated and measured results of amplitude response and phase balance of the proposed Marchand balun. The new balun was simulated using Ansoft

HFSS v9.0. The measurement was carried out on the HP8510C vector network analyzer. It is observed that good agreement is achieved between measurement and simulation. The measured return loss is found to be around -18 dB from 1.7 GHz to 2.8 GHz and better than -10 dB over the frequency band from 1.2 GHz to 3.3 GHz, or around 100% bandwidth. The measured amplitude and phase imbalance between the balanced output ports are within 1dB and 4° , respectively, over the operating frequency band.

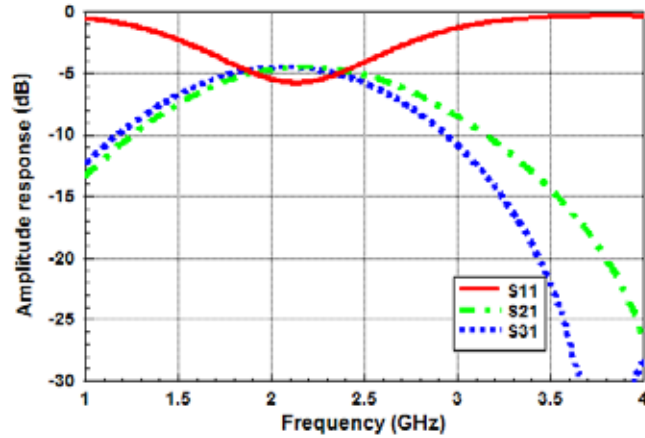


(a) Amplitude Responses

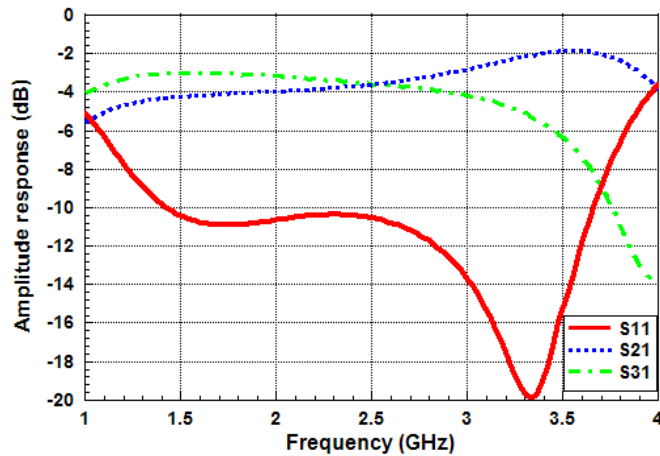


(b) Phase Responses

Figure 3.8 S-parameters of the proposed Marchand Balun



(a) Case 1: the ground plane under the coupled lines kept perfect without any removed



(b) Case 2: the ground plane under the coupled lines removed and no separated rectangular conductor placed under the coupled lines

Figure 3.9: Simulated S-parameter performance for the two contrast designs

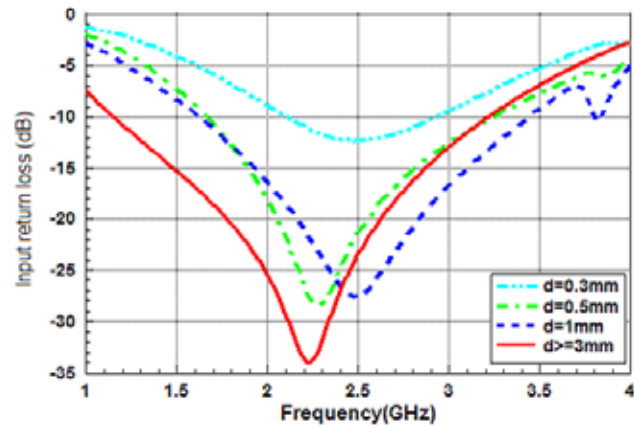
To further demonstrate the merits of the proposed design, two contrasting design cases were simulated. Case 1 is where the ground plane under the coupled lines was kept perfect without any removed, and Case 2 is where the ground plane under the coupled line was removed, but the two extra separated conductors under the coupled lines were not added. The simulated amplitude responses of these two design cases are shown in Figures 3.9(a) and (b), respectively. From Figure 3.9(a), it is observed that the matching at the unbalanced port S_{11} is

very poor over the band for Case 1. From Figure 3.9(b), it is observed that the matching at the unbalanced port can be improved but the imbalance between the two balanced ports has become worse for Case 2. The measured and simulated results, shown in Figures 3.8 and 3.9, demonstrate very clear advantages for the proposed design method in achieving an improved planar Marchand balun using a patterned ground plane.

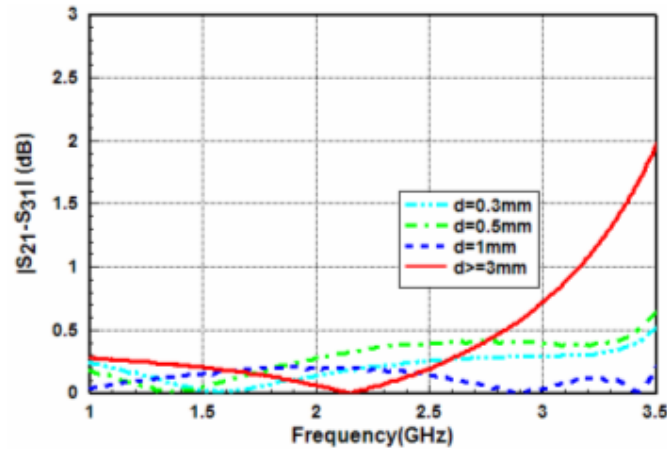
Since the proposed improved Marchand balun may be used in system applications, the radiation effects from the patterned ground plane should be considered. A minimum depth for the air cavity is necessary; otherwise practical values of Z_{0e} and Z_{0o} will be disturbed. To investigate the performance interference when the proposed balun is packaged into a system box, we place a ground plane as a virtual system box surface, and use HFSS to simulate the effects. Figures 3.10(a) and (b) show the input return losses and amplitude imbalance between balanced ports of the proposed balun for various values of depth of the air cavity d . With reference to Figure 3.10, it can be seen that in our design the interference is mainly relevant to the input impedance matching, and when d is larger than 3 mm, the interference can be ignored. When $d < 3$ mm, the smaller is the depth of the air cavity, the stronger is the interference. A value of the cavity depth d less than 0.5 mm is not recommended in order to maintain a good performance. Moreover, from Figure 3.10(a), a slight shift of the central frequency to the upper band can also be observed. This phenomenon may be caused by the fringing effects of the coupled lines with the modified ground plane.

Misalignment for the front and back side of the fabricated board is another factor which may affect the performance of the proposed balun design. Therefore, we examine the impact of the misalignment, which is defined as the distance between the longitude midlines of the coupled lines and the conductor on the bottom side of the PCB. In an ideal case, the

misalignment is assumed to be 0. According to our studies, good performance can be expected if the misalignment is less than 1mm.



(a) Return losses of the unbalanced port



(b) Amplitude imbalance between the balanced ports

Figure 3.10: Simulated return losses of the proposed balun with various values of depth of the air cavity d

Compared to Marchand balun designs in the prior arts, the present balun has the merits of planar structure and is easy to realize. The comparisons between the newly proposed balun and the prior arts have been tabulated and summarized in Table 3.3. Note that in Table 3.3, the bandwidths are determined by the impedance bandwidth (-10dB) as well as phase bandwidth based on a $\pm 5^\circ$ phase imbalance.

Table 3.3: Comparison between the present design and the prior arts

Item	Bandwidth	Complexity	Planar structure
Pavio and Kikel's balun [27]	100%	High (Multilayer/MMIC)	no
Tsai's balun [28]	92.3%	High (Interdigital coupler/MMIC)	yes
Shimozawa et. al's balun [29]	100%	High (Lange coupler/MMIC)	yes
Present balun	~100%	Low	yes

3.3 Conclusion

A new Marchand balun using a patterned ground plane has been presented in this chapter. In our new design, we have demonstrated that not only has the even-mode impedance increased, the odd-mode impedance has also decreased. The proposed structure provides a planar configuration which greatly simplifies its use in many applications. Design theory and procedure have been presented to optimize the Marchand balun. The novel Marchand balun has been simulated and verified by measurement. The measured results show that the proposed Marchand balun has a bandwidth of around 100%. The measured amplitude and phase imbalances between the two balanced ports are within 1dB and 4° , respectively, over the operating frequency band. Furthermore, two contrasting designs have also been presented to demonstrate the merits of the novel design method.

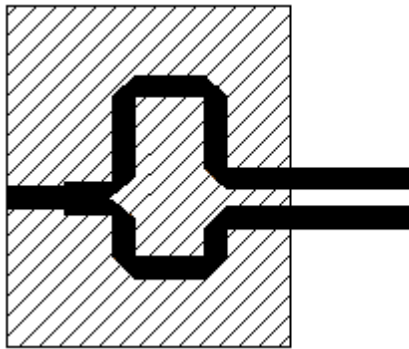
Chapter 4

A Broadband Tapered Balun Transition

A balun is a device for converting signals between an unbalanced circuit structure and a balanced circuit structure. Based on this description, two categories of planar formed baluns with respect to their applications can be defined. The first category of balun can be referred to as the microstrip-to-microstrip balun, which means that the interface of unbalanced and balanced ports is microstrip lines. The second category of balun can be referred to as a transition between an unbalanced line (microstrip or coplanar waveguide) and a balanced line such as broadside parallel strip and coplanar stripline (CPS). Broadside parallel stripline and coplanar stripline are both widely used in feeding networks of printed dipole antennas, balanced mixers and optoelectronic circuits.

To date, a number of reported efforts have been dedicated to the bandwidth enhancement of balun transitions [36-41]. For example, in [36], Dib et al. reported a type of microstrip-to-CPS transition based on the concept of mode conversion with a 3 dB back-to-back insertion loss bandwidth from 7 GHz to 11.5 GHz. In [37], Qian and Itoh provided a microstrip-to-CPS transition from 6 GHz to 13 GHz. In [38], Suh et al. presented a microstrip-to-CPS transition with an insertion loss of less than 3 dB and a return loss of better than 10 dB operating from 1.3 GHz to 13.3 GHz. For CPW-to-CPS transitions, many broadband

transitions have also been developed. Tilley et al. [39] reported a wideband CPW-to-CPS transition with a 1 dB back-to-back insertion loss bandwidth from 0.45 GHz to 5 GHz. Li et al. [40] proposed a CPW-to-CPS back-to-back transition with the bandwidth ranging from 0.4 GHz to 3.6 GHz. Figures 4.1(a)-(d) show these balun transition configurations. Moreover, for microstrip-to-broadside parallel strip transitions, Duncan and Minerva [41] introduced a tapered coaxial balun structure for broadband performance, which has been extensively used in many wideband applications. The planar form structure is shown in Figure 4.2.

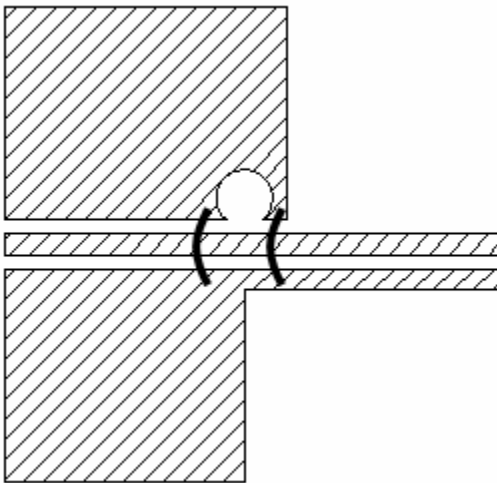


(a) Microstrip-CPS transition [36, 37]

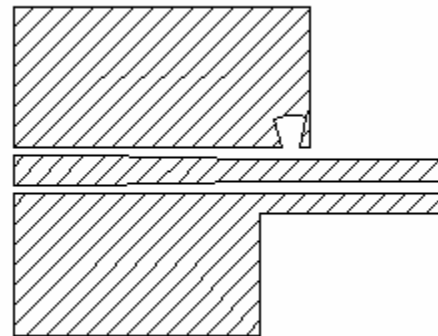


(b) Microstrip-CPS transition [38]

■ Metallization on top layer
 ▨ Metallization on bottom layer



(c) CPW-CPS transition [39]



(d) CPW-CPS transition [40]

Figure 4.1: Transition configurations in prior arts

CHAPTER 4. A BROADBAND TAPERED BALUN TRANSITION

This chapter focuses on the studies of tapered balun transitions for bandwidth enhancement. Firstly, the microstrip tapered balun are investigated. Compared with the conventional Marchand balun, the tapered balun shows a very broad bandwidth performance. Secondly, as the most important part of this chapter, a broadband uniplanar balun transition, which can either be used as a microstrip-to-microstrip or a microstrip-to-CPS transition, is reported. The proposed balun transition consists of a section of edge coupled transmission line, and a taper is employed on both of the coupled lines to increase its bandwidth. The performance of the newly proposed transition is investigated in terms of a microstrip-to-microstrip and a microstrip-to-CPS transition. Lastly, as an application example, a UWB omnidirectional planar dipole antenna, fed by the planar tapered balun, is proposed and studied. In this chapter, all the fabrication works were outsourced to Shenzhen King Brother PCB Technology CO., LTD. More details are available in the company website www.kbpcb.com.

4.1 Transition from microstrip line to parallel strip line

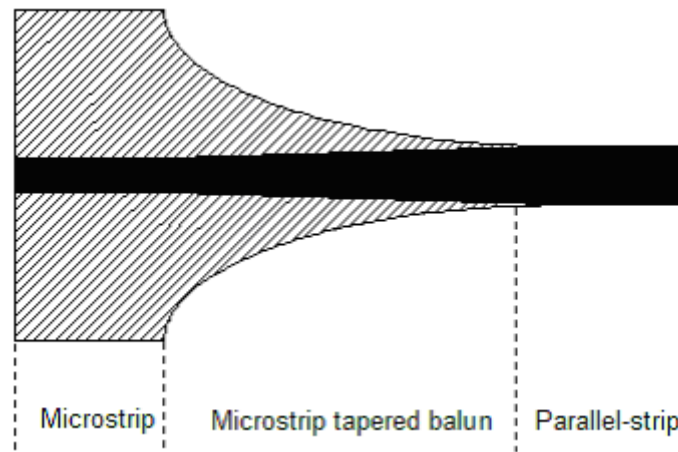


Figure 4.2: Layout of microstrip tapered balun

Figure 4.2 illustrates the configuration of the balun transition from microstrip line to double-sided parallel strip. This microstrip tapered balun is the planar form of the balun structure proposed by Duncan and Minerva [41]. The microstrip tapered balun consists of a section of a $\lambda/4$ broadside coupled transmission line with a dielectric substrate mounted in the middle of the metallic planes. There is a taper in both the top and bottom conductor widths and the signal potential is always between the conductors. The input signal is excited at the left end of the upper side metallic conductor, and at the other end, the strips of the different layers constitute an output balanced line. To investigate the performance of the microstrip tapered balun, we have designed one using the microwave substrate RO4003 of thickness 0.8 mm and dielectric constant $\epsilon_r = 3.38$. The input unbalanced port impedance is 50 ohms, and the strip width of the balanced lines is 2.5 mm to keep the parallel-strip characteristic impedance at 50 Ω .

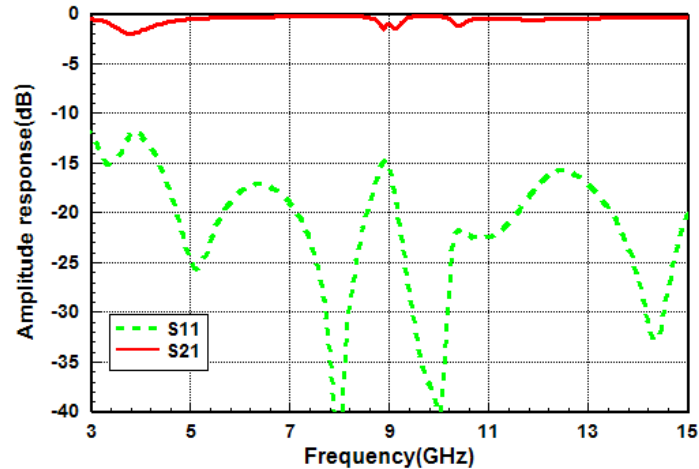


Figure 4.3 Amplitude response of two back-to-back microstrip tapered baluns

The microstrip tapered baluns were simulated using two back-to-back baluns because, in practice, it is difficult to interface the balanced ports with actual measurement equipment. Figure 4.3 shows the amplitude response of two back-to-back microstrip tapered baluns. As can be observed from the graph, the bandwidth of the microstrip tapered balun is much broader than that of the conventional Marchand balun. With the operating band from 3-15 GHz, the microstrip tapered balun can easily cover the unlicensed UWB band (3.1-10.6 GHz) allocated by the Federal Communications Commission (FCC).

4.2 A Novel Planar Tapered balun

Although the microstrip tapered balun mentioned in the previous section has a very wide bandwidth, it is not suitable for many specific applications. For example, it cannot work as a CPS/microstrip antenna feeding network. In this section, a broadband uniplanar balun transition which can either be used as a microstrip-to-microstrip transition or a microstrip-to-CPS transition is presented. The proposed balun transition consists of a section of edge

coupled transmission line. And a taper is employed on both of the coupled lines to increase its bandwidth. The performance of the newly proposed transition is investigated in terms of a microstrip-to-microstrip and a microstrip-to-CPS transition.

4.2.1 Structure description

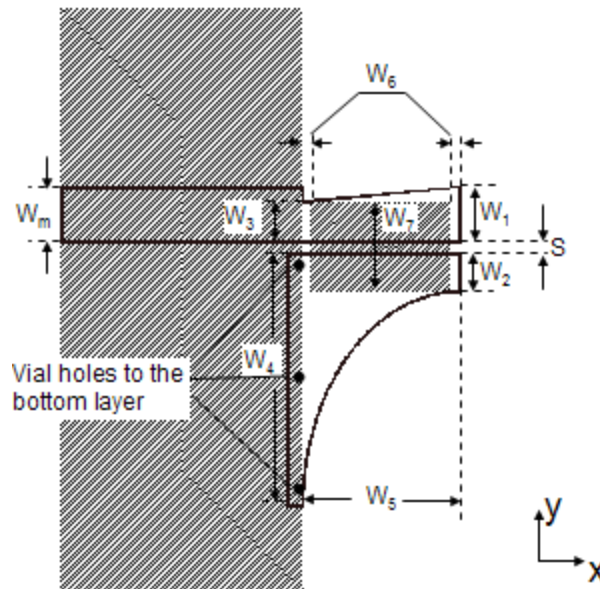
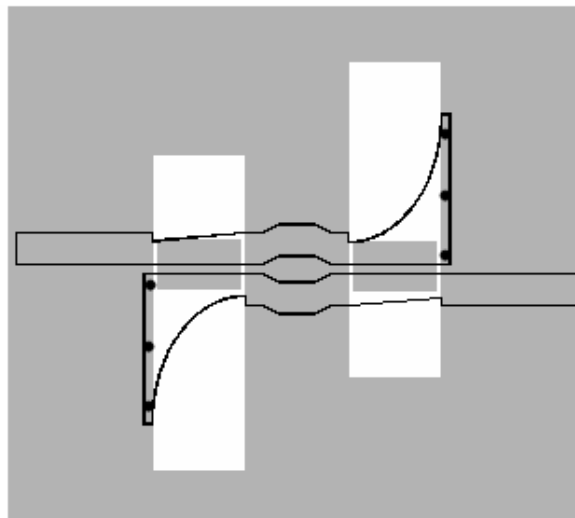


Figure 4.4 Configuration of the balun transition

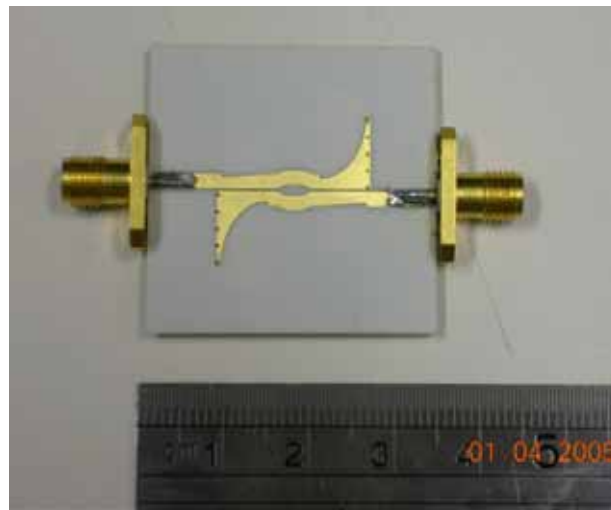
The structure of the proposed balun transition is illustrated in Figure 4.4. The solid line is the outline of the metallization of the front side of the substrate while the back side is shaded. The proposed balun consists of a section of edge coupled transmission lines. At the input end of the balun, one of the coupled lines joins the input microstrip line and the other is connected with the ground plane through via holes. The microstrip line at the input port is assumed to be 50Ω . The main idea of this transition is to generate 180° difference at the output end of the coupled lines. Both of the conductors have a gradual taper in width to increase the bandwidth performance of the balun transition. To enhance the coupling and

convert the electric field orientation from vertical to parallel against the substrate, the ground plane beneath the coupled lines is removed. Moreover, considering that tight coupling is not easily obtainable by way of the edge coupling, a separate rectangular conductor is added under the coupled lines to further enhance the coupling between the coupled lines.

4.2.2 Microstrip-to-microstrip balun transition



(a) Sketch of two back-to-back baluns



(b) Photograph of the prototype

Figure 4.5: Structure of two back-to-back baluns

To evaluate the performance of the proposed structure as a microstrip-to-microstrip balun transition, a balanced back-to-back transition configuration was developed, as shown in Figure 4.5. The solid line is the outline of the metallization of the front side of the substrate while the back side is shaded. It was built on the microwave substrate RO4003 with a dielectric constant of 3.38 and a thickness of 0.8 mm. To connect the two back-to-back baluns, a small section of uncoupled 50Ω microstrip line was used. As defined in Figure 4.3, the dimensions of the structure are: $W_1=1.9$ mm, $W_2=1.3$ mm, $W_3=1.4$ mm, $W_4=8.8$ mm, $W_5=5.5$ mm, $W_6=0.3$ mm, $W_7=2.85$ mm, $W_m=1.87$ mm, $S=0.15$ mm. To reduce discontinuity, the elliptic tapered line was used in our structure.

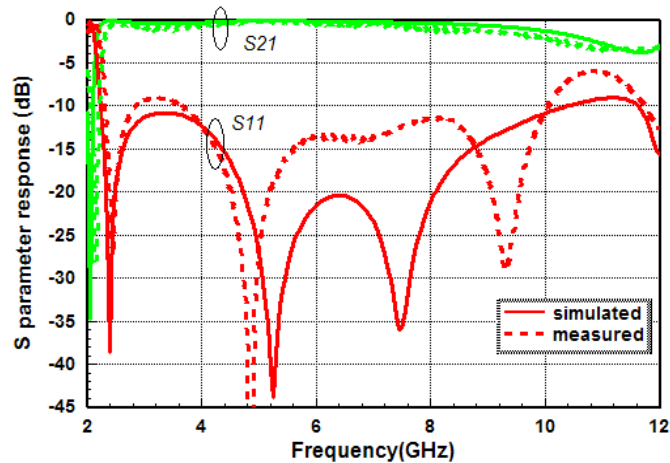


Figure 4.6: Return loss and insertion loss of the balanced back-to-back balun transition

Figure 4.6 displays the simulated and measured results of the back-to-back balun transition. The new transition was simulated using Ansoft HFSS. The measurement was carried out on the HP8510C vector network analyzer. It is observed that good agreement is achieved between measurement and simulation. The measured return loss is found to be around or better than -10 dB over the frequency band from 2.3 GHz to 10 GHz, or around 120%

bandwidth. The measured insertion loss for the two back-to-back baluns is within 2.5 dB over the operating frequency band.

To further demonstrate the effect of a separated rectangular conductor under the coupled lines for this microstrip-to-microstrip balun transition, a contrast design case was simulated. In this contrast design case, the conductor under the coupled lines is removed. Figure 4.7 displays the simulated amplitude responses of the back-to-back balun transition with the conductor under the coupled lines removed.

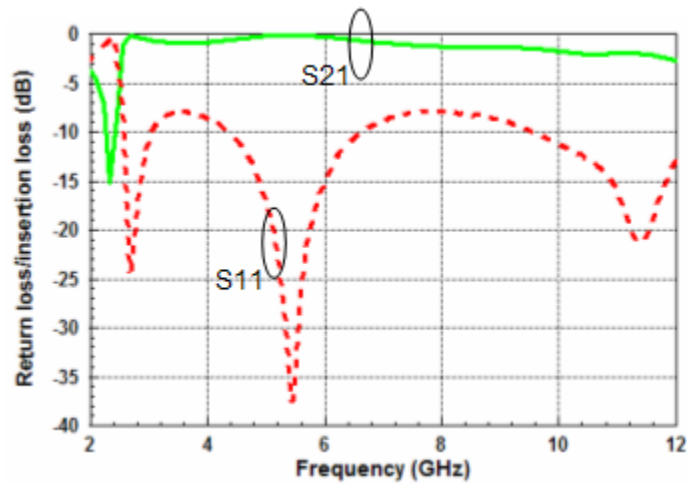


Figure 4.7: Simulated S-parameters for the contrast back-to-back microstrip-to-microstrip balun

Comparing Figure 4.6 and Figure 4.7, it is seen that the return loss can be improved when the separated rectangular conductor is added under the coupled lines.

4.2.3 Microstrip-to-CPS balun transition

To be used as a microstrip-to-CPS transition, this structure also exhibits a wide band characteristic. To evaluate the transition performance, a balanced back-to-back balun transition is designed for measurement purposes, as shown in Figure 4.8. The solid line is the

outline of the metallization of the front side of the substrate while the back side is shaded. The substrate used is a RO4003 with a dielectric constant of 3.38 and a thickness of 0.8 mm. The gap between CPS strips is 0.15 mm and the strip width is 2 mm. The CPS characteristic impedance is about 96Ω , as was simulated with IE3D. Defined in Figure 4.3, the physical dimensions of the structure are: $W_1=2.35$ mm, $W_2=2$ mm, $W_3=1.3$ mm, $W_4=9$ mm, $W_5=7$ mm, $W_6=0.3$ mm, $W_7=3.9$ mm, $W_m=1.87$ mm, $S=0.15$ mm.

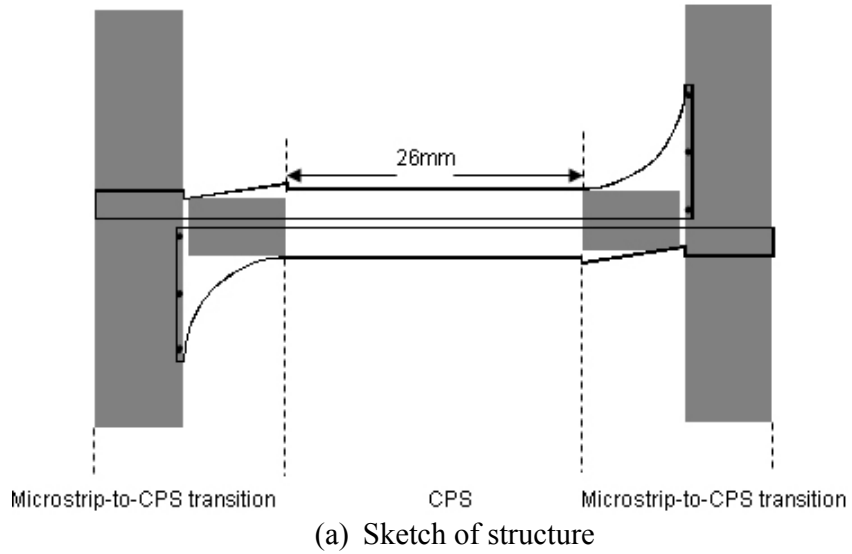


Figure 4.8: Microstrip-to-CPS back-to-back transition configuration

The return loss and insertion loss of the two back-to-back microstrip-to-CPS transitions were optimized with the aid of Ansoft simulation software HFSS and measured using the HP8510C network analyzer. The measured results, which include the effects from the SMA connectors, are presented using dashed lines in Figure 4.9. The return loss is better than -10 dB from 3 to 8.3 GHz achieving around 94% bandwidth, and insertion loss over the band is within 3 dB.

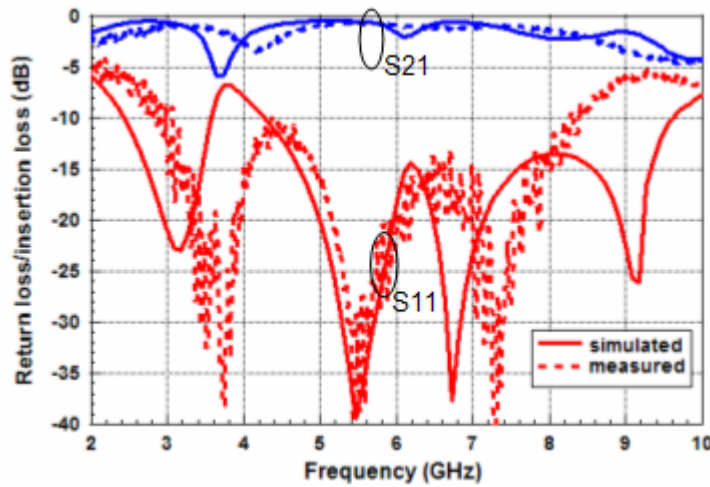


Figure 4.9: Measured input return and insertion loss of the balun transition

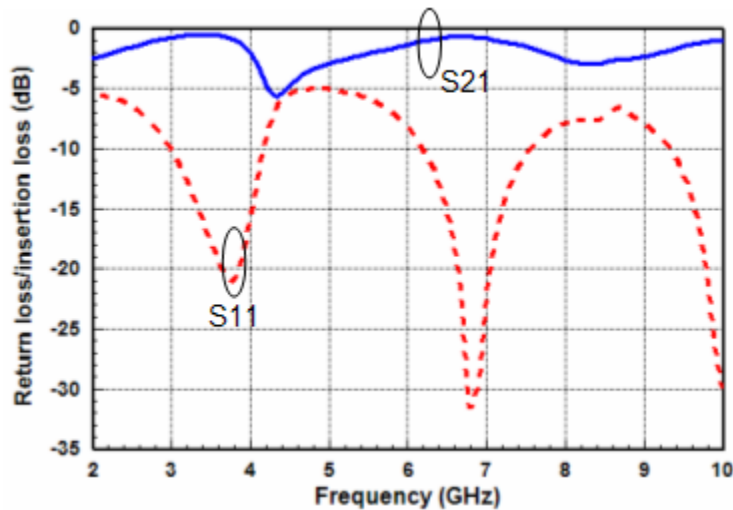


Figure 4.10: Simulated S-parameter performance for the contrast back-to-back microstrip-to-CPS balun

Likewise, to further demonstrate the effect of a separated rectangular conductor under the coupled lines for this microstrip-to-CPS balun transition, a contrast design case was simulated. In this contrast design case, the conductor under the coupled lines is removed. Figure 4.10 displays the simulated amplitude responses of the contrast back-to-back balun transition. Comparing Figure 4.9 and Figure 4.10, it is seen that the return loss can be improved when the separated rectangular conductor is added under the coupled lines. Moreover, since coupling between the coupled lines in our proposed balun structure can be enhanced when a high dielectric constant substrate material is used, better performance is expected when we choose a high dielectric constant substrate material.

Compared to balun transition designs in the prior arts, the present one has the merits of wideband performance and multipurpose applications. The comparisons between the newly proposed balun and the prior arts have been tabulated and summarized in Table 4.1. Note that in Table 4.1, the bandwidths are determined by the input return loss (-10dB) as well as insertion loss (-3dB) for back-to-back configurations.

Table 4.1: Comparison between the present design and the prior arts

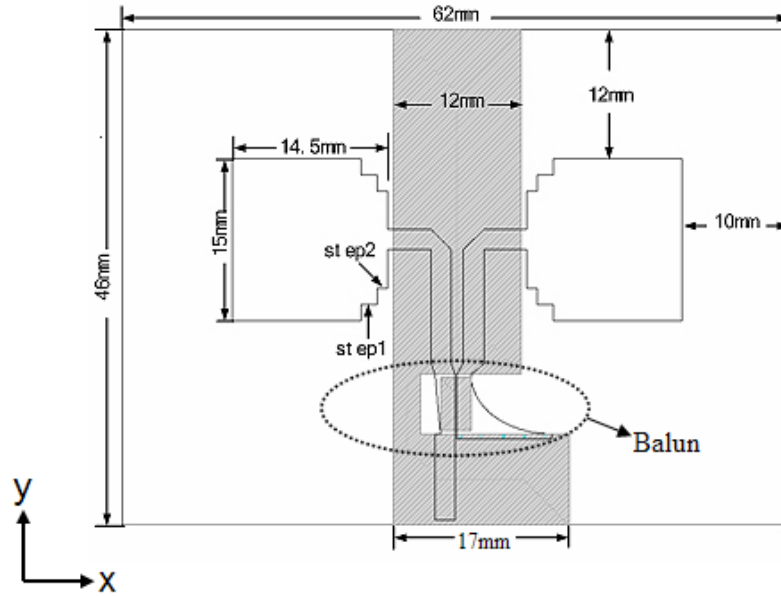
Item	Application	Bandwidth
Dib et. al's transition [36, 37]	Microstrip-CPS	49%
	Microstrip-CPW	44%
Suh and Chang's transition [38]	Microstrip-CPS	164%
Tilley et. al's transition [39]	CPW-CPS	25%
Li et. al's transition [40]	CPW-CPS	200%
Present balun	Microstrip-Microstrip	94%
	Microstrip-CPS	120%

4.3 An application of the proposed UWB planar tapered balun

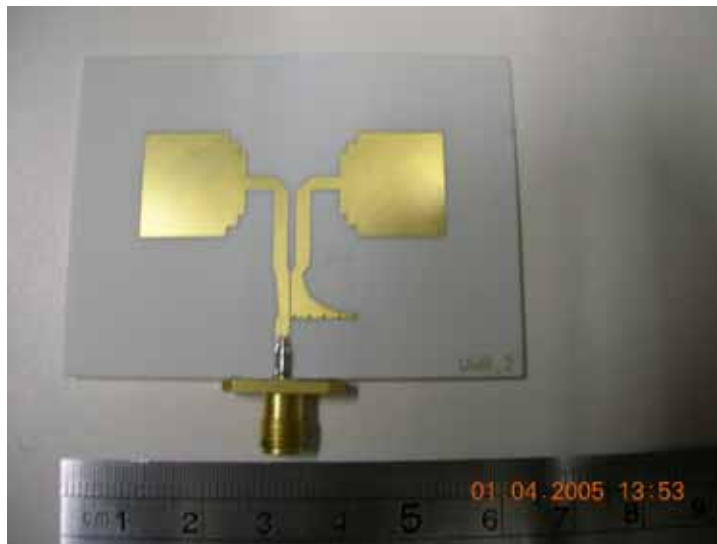
Antennas with an omnidirectional radiation pattern in the azimuth plane can be used in many applications and are very attractive for wireless communications such as the mobile and wireless local area network (WLAN) systems [42]. On the other hand, ultra-wideband antennas have received a lot of interests and applications in communication systems with broadband and spread-spectrum features in radar systems [43]. In this section, we present a planar dipole antenna having omnidirectional radiation property in an ultra-wideband operating bandwidth. The monopole patch antenna used for UWB application was introduced by S. H. Choi et al. [44].

4.3.1 Antenna Configuration

The geometry of the proposed UWB planar dipole antenna fed by the microstrip tapered balun transition is shown in Figure 4.11. The dimensions of step 1 and step 2 are $1.5 \times 1.5 \text{ mm}^2$ and $1 \times 1.5 \text{ mm}^2$, respectively. The area encircled by dashed line is the proposed planar tapered balun transition which provides a balanced signal to the dipole antenna.



(a) Sketch of the proposed antenna structure



(b) Photograph of the prototype

Figure 4.11: Proposed UWB planar dipole antenna.

4.3.2 Simulation and measurement results

Figure 4.12 illustrates the simulated and measured return loss of the proposed balanced UWB antenna. It is observed that good agreement is achieved between measurement and simulation.

As can be observed in Figure 4.12, the measured return loss of the UWB dipole antenna is under -10dB with an impedance bandwidth as wide as 8.4 GHz (from ~2.8 GHz to ~11.2 GHz), and it covers the entire frequency range (from 3.1 GHz to 10.6GHz) of the UWB system.

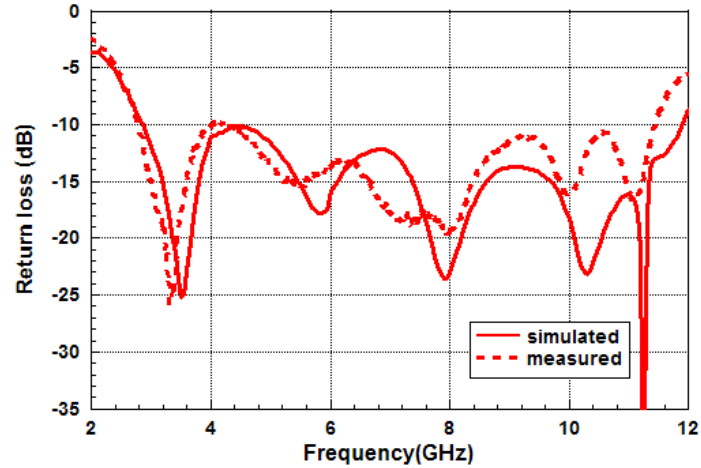
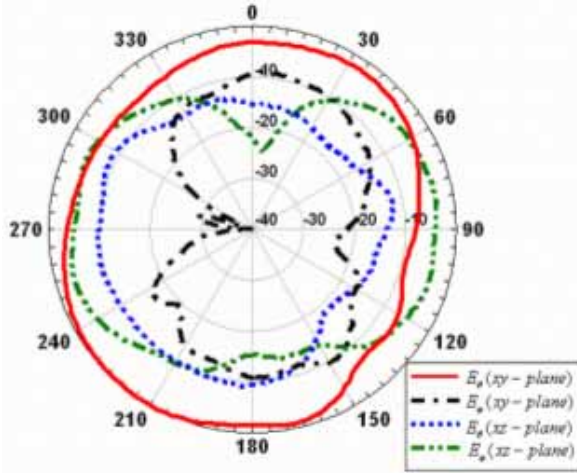
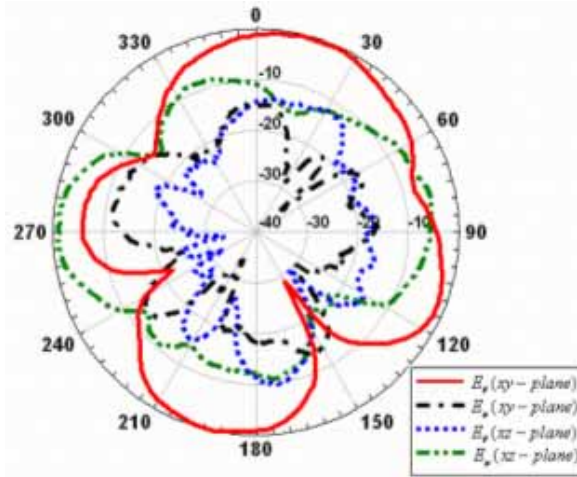


Figure 4.12 Simulated and measured return loss of the proposed UWB antenna

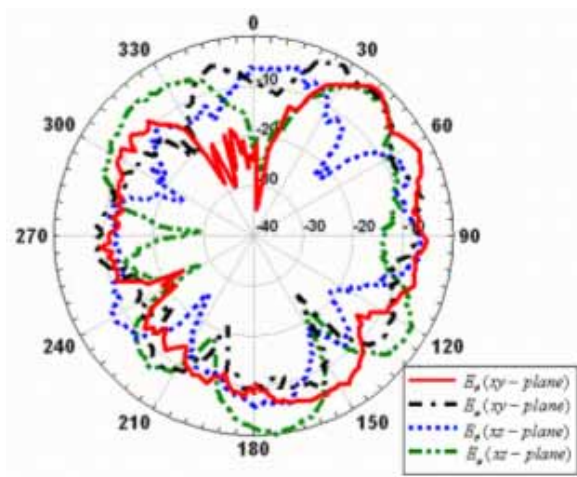
The measured radiation patterns of the proposed balanced UWB antenna are presented as shown in Figure 4.13. The measured antenna gain of the proposed balanced UWB antenna is shown in Figure 4.14. It can be seen that the obtained gain is in the range of 4 to 8dBi.



(a) $f = 3$ GHz



(c) $f = 6.5$ GHz



(d) $f = 10$ GHz

Figure 4.13: Measured radiation patterns of the proposed balanced UWB antenna

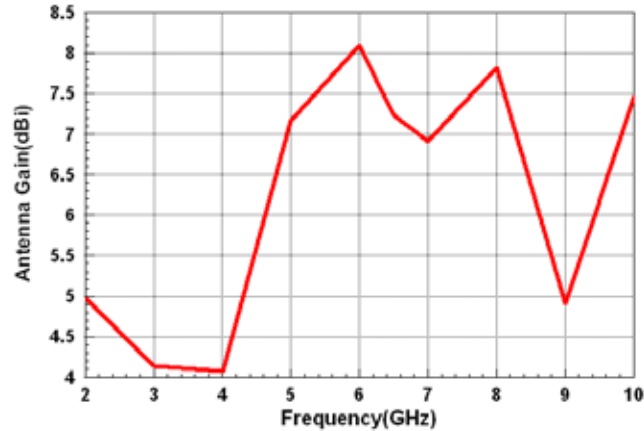


Figure 4.14: Measured peak antenna gain across the operating bandwidth

4.4 Conclusion

In this chapter, balun transitions using tapered lines for bandwidth enhancement have been investigated. Firstly, the microstrip tapered balun was examined. Compared with conventional Marchand baluns, the microstrip tapered baluns show broadband performance. However, this balun transition is difficult to use in some applications due to its non-planar configuration. To solve this problem, a broadband uniplanar balun transition, which can either be used as a microstrip-to-microstrip or a microstrip-to-CPS transition, has been reported for the first time. The proposed balun transition consists of a section of edge coupled transmission line, and a taper was employed on both of the coupled lines to increase its bandwidth. The performance of the newly proposed transition was investigated in terms of a microstrip-to-microstrip and a microstrip-to-CPS transition. Lastly, as an application example, a UWB omnidirectional planar dipole antenna fed by the planar tapered balun was proposed and studied.

Chapter 5

Wideband Microstrip Balun Design Using Phase Shifters

Planar baluns [45-50] are one of the most popular balun structures because of the ease in implementation and their good performance. The planar baluns mainly consist of the simple half-wavelength line separation splitters, the multi-section half-wave baluns and the coupled-line baluns. The N-section half-wave balun [45, 46] could be easily realized using the conventional printed circuit board (PCB) process, however it has some disadvantages, such as the large size, and bad return loss and isolation at the balanced ports, which greatly restrict its application in many wireless communications systems. Most of the other planar baluns, including either the planar Marchand baluns [47] or the planar transmission line baluns consisting of a power divider and a coupled-line 180° phase shifter [48-50], utilize edge-coupled structures. For the edge-coupled structures, the coupling factor is largely dependant on the gap between the two coupled-lines and the dielectric constant of the substrate. For the MMICs or MICs design, the gap between the two coupled-lines could be a few micrometers, thus tight coupling is still achievable in the edge-coupled way. However, for the designs using the PCB fabrication technology, such planar baluns usually tend to choose the inter-digital Lange couplers, the broadside coupling lines, i.e. multi-layer structures, or

modifying the even- and odd-mode impedances of the coupled lines to achieve tight coupling [47], which are high in cost or complex in structure.

Phase shifters could find their applications in baluns, and many efforts have been taken to develop wideband phase shifter structures and improve the performance of the phase shifters [51-54]. To evaluate the performances of a phase shifter, one should be most concerned with a low insertion loss and a flat phase characteristic. In the simplest case, a section of transmission line can be deemed as a phase shifter because electromagnetic waves travel with a certain velocity in the transmission material. By properly adjusting the length of the transmission line, a wide range of phase shifting can be achieved. However, since the length of the transmission line section is largely related to the operating frequency, a stable phase shift within a wide bandwidth can not be achieved. To obtain a wide band performance, several coupled line structures are proposed [48-51]. Among them, one of the most popular structures is the Schiffman phase shifter [51] which employs a C-section coupled line. Based on Schiffman's work, several different phase shifter configurations have been proposed and investigated [52-54].

The aim of this chapter is to develop a wideband planar balun which can be easily realized using the conventional PCB technique, and the key concept is to realize such a balun using a power divider and a wideband 180° phase shifter. The challenge is how to find a suitable wideband 180° phase shifter which can be applied in the single layer PCB environment. Many previously proposed phase shifter structures have been proved not suitable for the conventional PCB design [48-50]. Firstly, a Schiffman phase shifter was examined. According to the analysis, the bandwidth of the Schiffman phase shifter is largely relevant to the coupling of the C-section coupled line. Previously, most of Schiffman phase shifters were

designed using MMICs or MICs technique. In this chapter, a novel wideband 90° Schiffman phase shifter, on a single layer PCB, using the patterned ground plane technique, is introduced for the first time and validated by the simulation and measurement results. According to the theoretical analysis, a single section Schiffman phase shifter is not suitable for 180° phase shifting. On the other hand, it can be implemented by cascading two 90° Schiffman phase shifters. However such arrangement may bring a larger insertion loss and size occupation. Since a Schiffman phase shifter is not a good choice for the balun design, another simple 180° phase shifter structure was studied. This 180° phase shifter does not require any coupled line configuration, and therefore can be easily applied in the conventional PCB. Based on the 180° phase shifter, we presented a novel planar balun structure on a single-layer PCB. The microstrip baluns proposed by Roger and Bhartia in [48] and Bharj et al. in [49] both employed tightly coupled lines. They can be realized in multilayer structures or MICs design. However, they cannot be realized using the conventional single-layer PCB technique, which is low cost. Compared with other previously proposed microstrip baluns, the newly proposed balun structure shows great advantages in low cost and good performance. Moreover, such planar balun has been used for balanced antenna designs and good performances have been obtained. In this chapter, the fabrication work was done in the author's lab.

5.1 Standard Schiffman phase shifter

5.1.1 Structure description

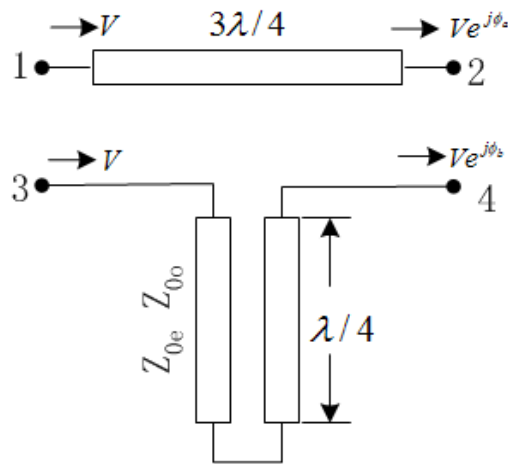


Figure 5.1: Standard 90 degree Schiffman phase shifter structure

Figure 5.1 shows a standard 90° Schiffman phase shifter structure [51]. The phase shifter is a 4-port network with two separate branches. One branch is a section of reference transmission line, and the other comprises a symmetrical coupled-line section with one end, named the C-section network, connected. In the ideal case, the connection part should be zero in length. Input and output ports were stretched from the other end. A well designed phase shifter would introduce an insertion loss as small as possible.

5.1.2 Analysis

To analyze the C-section coupled-line network in the Schiffman phase shifter, image impedance was introduced. Image impedances, Z_{i1} and Z_{i2} , are defined for the network as:

Z_{i1} =input impedance at port 1 when port 2 is terminated with Z_{i2} ,

Z_{i2} =input impedance at port 2 when port 1 is terminated with Z_{i1} .

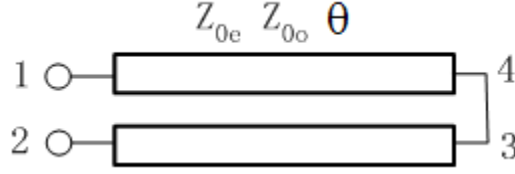


Figure 5.2: Coupled-line transform used in the Schiffman phase shifter

In the C-section coupled-line structure shown in Fig. 5.2, port 3 and port 4 are interconnected.

The Z matrix of the transformed 2-port network yields under the boundary condition $U_3=U_4$ and $I_3 = -I_4$.

$$Z_{2\text{port}} = \begin{bmatrix} Z_{11} + \frac{(Z_{13} - Z_{14})(Z_{41} - Z_{31})}{Z_{33} - Z_{34} + Z_{44} - Z_{43}} & Z_{12} + \frac{(Z_{13} - Z_{14})(Z_{42} - Z_{32})}{Z_{33} - Z_{34} + Z_{44} - Z_{43}} \\ Z_{21} + \frac{(Z_{23} - Z_{24})(Z_{41} - Z_{31})}{Z_{33} - Z_{34} + Z_{44} - Z_{43}} & Z_{22} + \frac{(Z_{23} - Z_{24})(Z_{42} - Z_{32})}{Z_{33} - Z_{34} + Z_{44} - Z_{43}} \end{bmatrix} \quad (5.1)$$

where Z_{mn} ($m, n=1, \dots, 4$) is the impedance matrix of a symmetrical coupled line section with the port orders defined in Figure 5.2.

Convert Z matrix to ABCD matrix:

$$A_{\text{BCD}} = \begin{bmatrix} \frac{Z_{0e} - Z_{0o} \tan^2 \theta}{Z_{0e} + Z_{0o} \tan^2 \theta} & \frac{2jZ_{0e}Z_{0o}}{Z_{0e} \cot \theta + Z_{0o} \tan \theta} \\ 2j & \frac{Z_{0e} - Z_{0o} \tan^2 \theta}{Z_{0e} + Z_{0o} \tan^2 \theta} \\ \frac{Z_{0e} \cot \theta + Z_{0o} \tan \theta}{Z_{0e} + Z_{0o} \tan^2 \theta} & \frac{Z_{0e} - Z_{0o} \tan^2 \theta}{Z_{0e} + Z_{0o} \tan^2 \theta} \end{bmatrix} \quad (5.2)$$

the two-port network is symmetrical, thus $A=D$

$$Z_i = \sqrt{\frac{B}{C}} = \sqrt{Z_{0e}Z_{0o}} \quad (5.3)$$

From the analysis above, it was found that image impedance Z_i is independent from frequency, therefore this structure had a broadband characteristic in terms of the impedance matching. For example, if we chose the port impedance at 50Ω for a 90° phase shifter design, $\sqrt{Z_{0e}Z_{0o}} = 50 \Omega$ should be fulfilled to achieve a good impedance matching.

The phase response with frequency of a C-section coupled line has been derived by Jones and Bolljahn [57], and can be expressed in term of the even- and odd-mode impedances of the coupled-line and the length.

$$\Phi_b = \cos^{-1} \left(\frac{\frac{Z_{0e}}{Z_{0o}} - \tan^2 \theta}{\frac{Z_{0e}}{Z_{0o}} + \tan^2 \theta} \right) \quad (5.4)$$

The phase shifting

$$\Delta\phi = K\theta - \cos^{-1} \left(\frac{\frac{Z_{0e}}{Z_{0o}} - \tan^2 \theta}{\frac{Z_{0e}}{Z_{0o}} + \tan^2 \theta} \right) \quad (5.5)$$

where K stands for the ratio of the length of uniform transmission line to the coupled one, and θ stands for the electrical length of the coupled line.

The maximum of differential phase shift $\Delta\phi_{\max}$ in terms of ρ was derived [54] as

$$\Delta\phi_{\max} = K \tan^{-1} \sqrt{\frac{K\rho - 2\sqrt{\rho}}{2\sqrt{\rho} - K}} - \cos^{-1} \left(\frac{\rho + 1 - K\sqrt{\rho}}{\rho - 1} \right) \quad (5.6)$$

where $\rho = \frac{Z_{0e}}{Z_{0o}}$.

5.1.3 Design curve and example

For example, if we want to obtain a 90° standard Schiffman phase shifter with a $\pm 5^\circ$ phase error tolerance, the maximum of differential phase shift can be determined

$$\Delta\phi_{\max} = 95^\circ \quad (5.7)$$

By substituting $K=3$ and (5.7) into (5.6), we obtain:

$$\rho = 3.017 \quad (5.8)$$

So the corresponding even- and odd-mode impedances are:

$$\begin{aligned} Z_{0e} &= \sqrt{\rho} \cdot Z_0 = 86.85(\Omega) \\ Z_{0o} &= \frac{Z_0}{\sqrt{\rho}} = 28.79(\Omega) \end{aligned} \quad (5.9)$$

The following equations can be used to obtain the bandwidth [54]:

$$\Delta\phi_{\min} = 85^\circ = K\theta_1 - \cos^{-1}\left(\frac{\rho - \tan^2 \theta_1}{\rho + \tan^2 \theta_1}\right) \quad (5.10)$$

$$B = \frac{180^\circ - 2 \cdot \theta_1}{90^\circ} \quad (5.11)$$

where θ_1 stands for the lowest band where $\Delta\phi_{\min}$ locates and B stands for the maximum bandwidth.

By solving the equations, it was found that $B=80.5\%$. Therefore, it was proved that, within a $\pm 5^\circ$ phase error tolerance, the standard Schiffman phase shifter can obtain a bandwidth of 80.5% . To achieve this, the even- and odd-mode impedance ratio $\rho = 3.017$ was required.

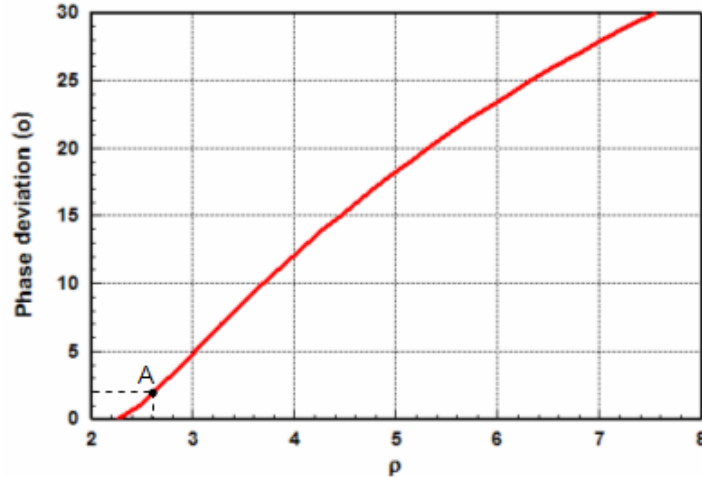


Figure 5.3: Phase deviation versus impedance ratio ρ for the standard 90° Schiffman phase shifter

In Figure 5.3, the relationship between the phase deviation in degrees and the impedance ratio was plotted for the optimal bandwidth performance. From the design curve, a minimum value $\rho=2.25$ is required, otherwise, there would be no solution for the standard 90° Schiffman phase shifter. According to the design curves, a 90° Schiffman phase shifter with $\pm 2^\circ$ phase derivation was designed to ensure that an optimal bandwidth can be obtained. From Figure 5.3, we chose the point A with an impedance ratio $\rho=2.61$. Accordingly, the even- and odd-mode impedance of the coupled lines could be determined as:

$$Z_{0e}=50 \cdot \sqrt{\rho}=80.8 \Omega, Z_{0o}=\frac{50}{\sqrt{\rho}}=30.95\Omega.$$

This also implied that a strong coupled line section with the coupling factor of -7dB should be attained. Microwave substrate RO4003 having thickness 0.8 mm and dielectric constant $\epsilon_r=3.38$ was used in our design. The geometry of the coupled line could be determined as $W=1.25$ mm and $S=0.028$ mm. As shown in Figure 5.4, W and S were defined as the width of the coupled lines and the spacing between coupled lines, respectively.

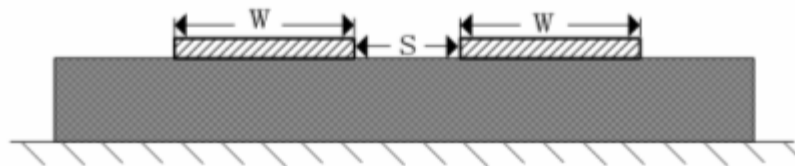
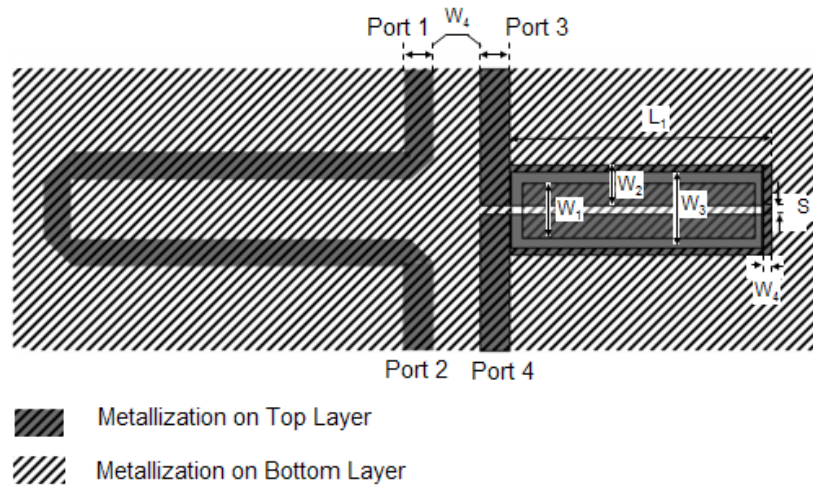
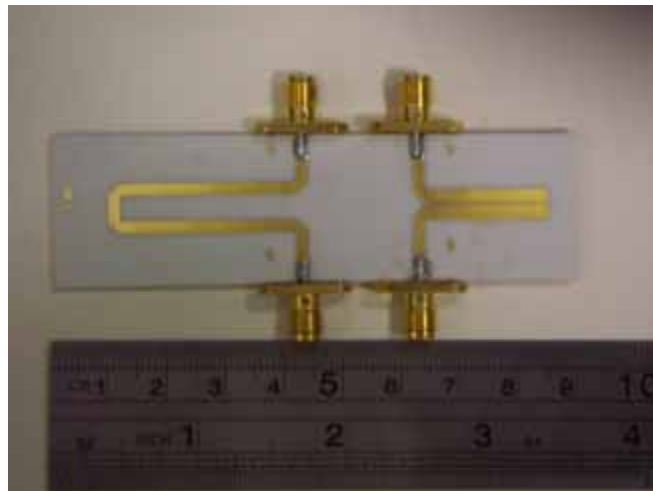


Figure 5.4: Side view of the edge coupled transmission line



(a) Layout schematics



(b) Photograph of the prototype

Figure 5.5: 90° Schiffman phase shifter using a patterned ground plane
 $W_1=3.05$ mm, $W_2=2.4$ mm, $W_3=4$ mm, $W_4=0.3$ mm, $L_1=21$ mm and $S=0.3$ mm

For conventional single layer PCB process, such a tight coupling was difficult to obtain using the edge coupled line structure since S was too small to be fabricated. For this case, we used the patterned ground plane technique, which has been employed in Chapter 3 was proposed

to handle this problem. With a slot under the coupled lines cut on the ground plane, both the even- and odd-mode capacitances of the coupled lines would be decreased substantially. However, the decrease of the even-mode capacitance is much faster than that of the odd-mode capacitance. Meanwhile, an additional separated rectangular conductor was placed under the coupled lines to act as a capacitor so that the odd-mode capacitance could be increased. Figures 5.5(a) and 5.5(b) show the layout and photograph of the proposed 90° Schiffman phase shifter, respectively.

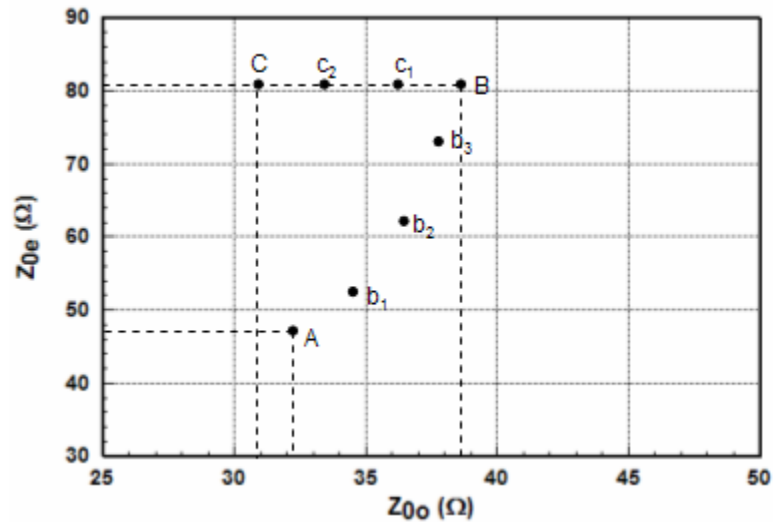


Figure 5.6: Even- mode impedance Z_{0e} versus odd- mode impedance Z_{0o} in the design procedure for the Schiffman phase shifter in Figure 5.5

In Figure 5.6, a design procedure is illustrated for this 90° Schiffman phase shifter design. The point C stands for the desired Z_{0e} and Z_{0o} , $Z_{0e}=80.8 \Omega$ and $Z_{0o}=30.95 \Omega$. Firstly the coupled lines are set 2.4 mm in width; and according to the PCB fabrication capability, the gap between the coupled lines is set as 0.3 mm. At this stage, with a perfect ground plane under the coupled lines, the even- and odd-mode impedances of the coupled lines can be determined as $Z_{0e} = 46.9 \Omega$ and $Z_{0o} = 32.3 \Omega$, which locate at point A in Figure 5.6. Then a slot is cut on the ground plane beneath the coupled lines to increase the value of Z_{0e} . The dots (b_1, b_2, b_3, B) denote the trace of Z_{0e} and Z_{0o} with varying the width W_3 of the slot.

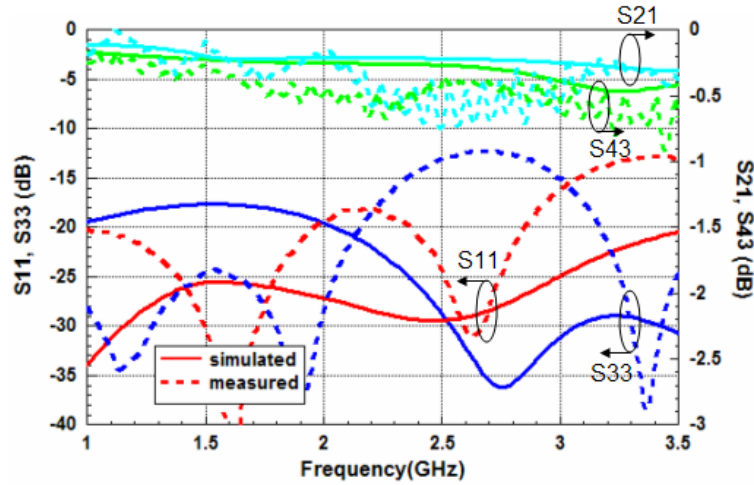
Regarding this movement from b_1 to B as in Figure 5.6, it is observed that a larger slot width will produce a higher even-mode impedance. At point B, $Z_{0e}=80.8 \Omega$. From Figure 5.6, Z_{0o} is too big to meet the requirement. Then an additional conductor is placed to decrease Z_{0o} . This treatment will not affect the value of Z_{0e} much. The dots c_1 and c_2 between point B and C denote the trace of Z_{0e} and Z_{0o} with varying the width W_1 of the additional conductors. Table 3.2 exhibits the relationship between the even- and odd-mode impedances Z_{0e} and Z_{0o} and the physical dimensions of the coupled lines with a patterned ground plane during the above process from point A to C.

Table 5.1: Relationship between the even- and odd-mode impedances Z_{0e} and Z_{0o} and the physical dimensions of the coupled lines with a patterned ground plane as in Figure 5.5

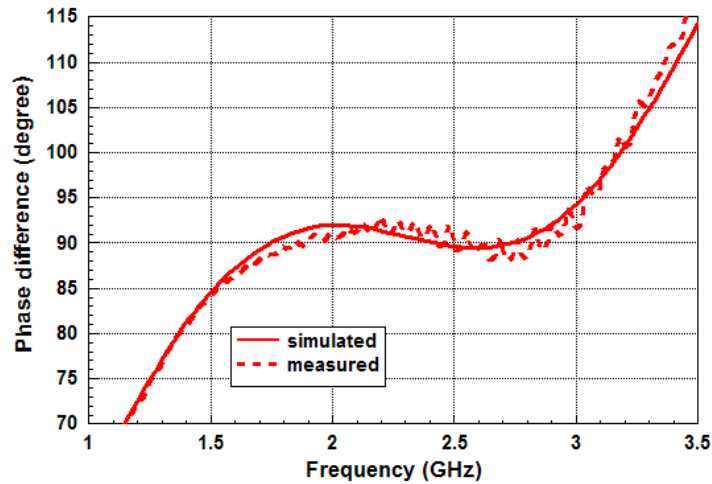
Trace point	$W_3(\text{mm})$	$W_1(\text{mm})$	$Z_{0e}(\Omega)$	$Z_{0o}(\Omega)$
A	--	--	46.9	32.3
b_1	1.2	--	52.3	34.5
b_2	2.2	--	62.6	36.4
b_3	3.2	--	73.2	37.8
B	4	--	80.8	38.7
c_1	4	1	80.8	36.5
c_2	4	2.1	80.8	33.6
C	4	3.15	80.8	32.3

With the port defined in Figure 5.5, the simulated and measured S parameter and phase difference response of the phase shifter are shown in Figures 5.7(a) and (b), respectively. The simulation work was carried out using the commercial software IE3D. From the measured results, it can be observed that the present design is capable of controlling the insertion loss less than 1 dB and the return loss better than -12 dB across a wide bandwidth. The phase

derivation is within $\pm 2^\circ$ covering a band from 1.7-2.9 GHz, or 52% bandwidth. A $\pm 5^\circ$ phase derivation can be obtained from 1.5-3.1 GHz, or about 70% bandwidth.



(a) S parameter response

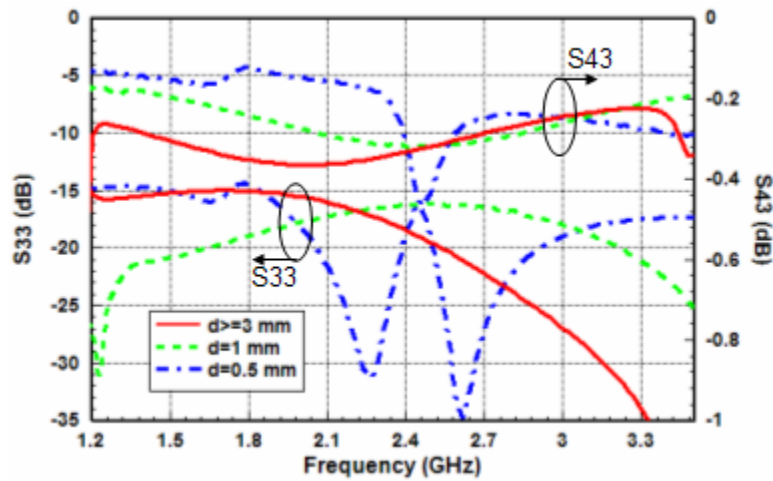


(c) Phase response

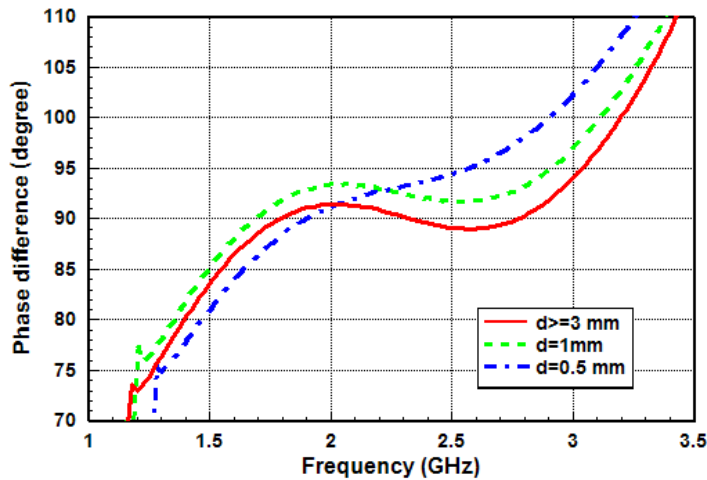
Figure 5.7: Simulated results of the 90° Schiffman phase shifter design

Since the proposed phase shifter may be used in system applications, the radiation effects from the patterned ground plane should be considered. A minimum depth for the air cavity is necessary; otherwise practical values of Z_{0e} and Z_{0o} will be disturbed. To investigate the performance interference when the proposed balun is packaged into a system box, we place a ground plane as a virtual system box surface, and use IE3D to simulate the effects. Since the

ground plane under the path 2-1 in Figure 5.5 is perfect, we only consider the radiation effects of path 4-3. Figure 5.8 shows the amplitude and phase difference responses of the proposed 90° Schiffman phase shifter for various values of depth of the air cavity d . With reference to Figure 5.8, it can be seen that in our design the interference can be ignored when d is larger than 3mm. When $d < 3\text{mm}$, the smaller is the depth of the air cavity, the stronger is the interference. A value of the cavity depth d less than 0.5 mm is not recommended in order to maintain a good performance.

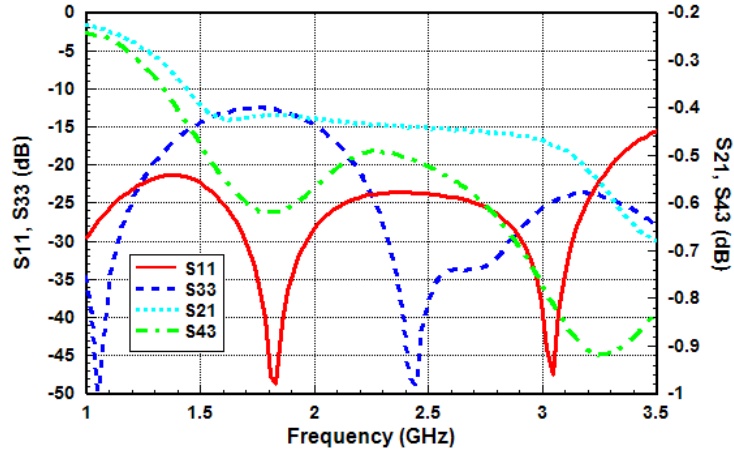


(a) Return losses and insertion losses

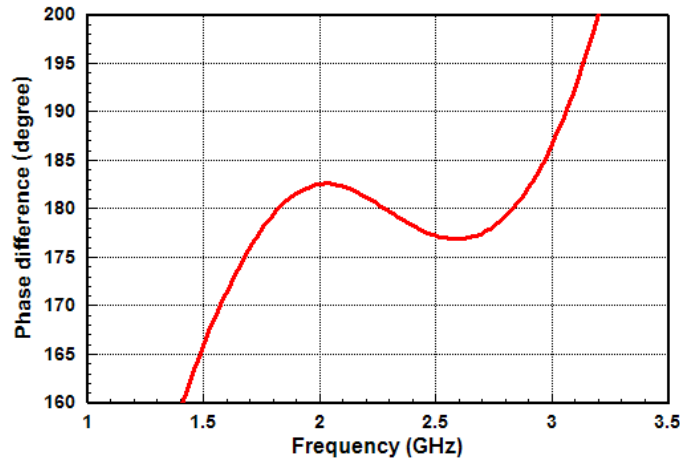


(b) Phase responses

Figure 5.8: Simulated amplitude and phase difference responses of the proposed 90° Schiffman phase shifter with various values of depth of the air cavity d



(a) S parameter response



(b) Phase response

Figure 5.9: Simulated results of two cascaded 90° Schiffman phase shifters

We can cascade two 90° Schiffman phase shifters to obtain a 180° phase shifter. The simulated S parameter and phase difference response of two cascaded 90° Schiffman phase shifters are shown in Figures 5.9(a) and (b), respectively. Again, the simulation work was carried out using IE3D. From the simulation results, it can be observed that the two cascaded 90° Schiffman phase shifters can maintain a $\pm 5^\circ$ phase derivation from 1.7-3.0 GHz, or about 55.3% bandwidth. Within the bandwidth, the insertion loss is less than 1 dB and the return loss better than -10 dB.

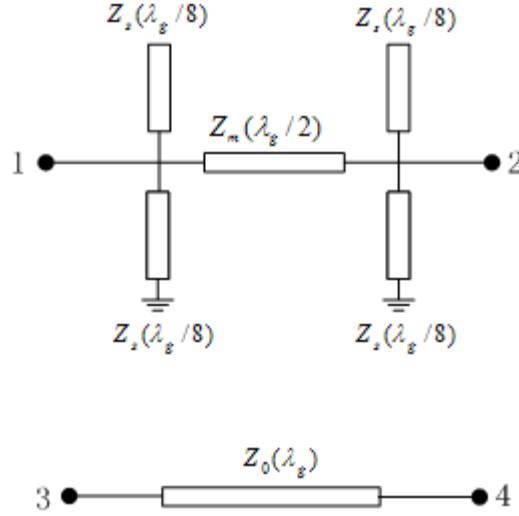
5.2 A broadband 180° phase shifter

Although the Schiffman phase shifters had good performance in achieving wideband phase shift with small insertion loss, there were two major drawbacks in utilizing them in balun structures. Firstly, according to Quirarte and Starski's analysis [54], Schiffman phase shifters work best when the electrical length of the C-section coupled lines θ is 90° (θ was treated as a variable) at the central frequency. The phase shifting is symmetric around $\theta=90^\circ$. It is convex for $\theta<90^\circ$ and concave for $\theta>90^\circ$. Therefore, the Schiffman phase shifters were not suitable for large phase shift like 180° or above. Secondly, the broadband performance in Schiffman phase shifter was largely related to the coupling factor of the coupled line.

As described in the following section, a broadband 180° phase shifter using $\lambda/8$ stubs for fast and fixed phase shifts [56] has been investigated. Compared to the Schiffman phase shifter, this phase shifter structure has no coupled line structure and could be easily realized using the conventional low cost PCB technique.

5.2.1 Analysis of the broadband 180° phase shifter

As shown in Figure 5.10, the path 3-4 of the phase shifter was a standard one wavelength transmission line with the characteristic impedance of Z_0 . The path 1-2 comprised a section of half wavelength transmission line with the characteristic impedance of Z_m . Four parallel $\lambda/8$ short and open stubs with the characteristic impedance of Z_s are connected at the end of the transmission line.


 Figure 5.10: A broadband 180° phase shifter structure

The input and output reflection coefficients of the scattering matrix could be obtained by [56]:

$$S_{33}=S_{44}=0 \quad (5.14a)$$

$$S_{11}=S_{22}=\frac{1}{2} \left\{ \frac{1-j(Y_m \tan \theta - 2Y_s \cot \theta)}{1+j(Y_m \tan \theta - 2Y_s \cot \theta)} + \frac{1+j(Y_m \tan \theta + 2Y_s \cot \theta)}{1-j(Y_m \tan \theta + 2Y_s \cot \theta)} \right\} \quad (5.14b)$$

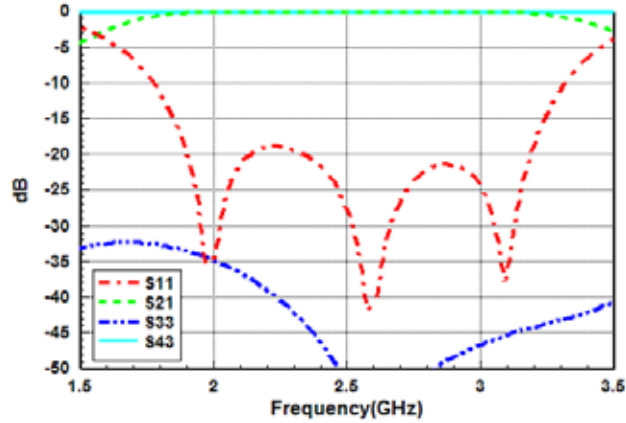
The relative transmission phase shift was obtained by:

$$\Delta\phi = \arg(S_{43}) - \arg(S_{21}) = -4\theta + \pi - \tan^{-1} \left(\frac{1 + Y_m^2 + 2Y_s Y_m \cot \theta (\tan \theta - \cot \theta) - (2Y_s \cot \theta)^2}{Y_m \tan \theta - Y_m \cot \theta - 4Y_s \cot \theta} \right) \quad (5.15)$$

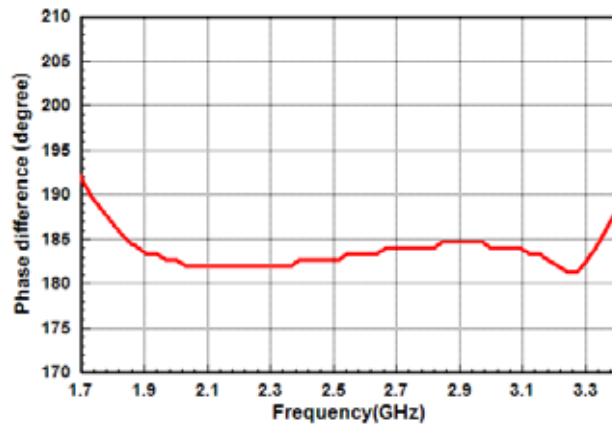
By simulations, the optimum values of Z_m and Z_s were obtained with the conditions of VSWR=1.15:1 and 2° maximum phase deviation [56]:

$$Z_m=80.5(\Omega) \quad (5.16)$$

$$Z_s=63.7(\Omega) \quad (5.17)$$



(a) S parameter response



(b) Phase derivation

Figure 5.11 Simulated results of the broadband 180° phase shifter

With the parameters above, a 180° broadband phase shifter operating at the central frequency 2.4 GHz was designed and simulated using IE3D. It was built on the microwave substrate RO4003 of thickness 0.8mm and dielectric constant $\epsilon_r=3.38$. Figures 5.11(a) and 5.11(b) show the amplitude and phase responses of the S parameters of the phase shifter design respectively. From the diagrams, it can be observed that the S parameter response of the phase shifter has a good performance. Return losses of the two branches are both below -10 dB over the frequency range 1.8-3.3 GHz and below -15 dB across 1.8-3.2 GHz. The phase derivation across the frequency band is within 4° .

5.3 A new wideband planar balun on a single-layer PCB

In this section, a new wideband planar microstrip balun has been proposed. The new wideband planar balun consisted of a 3 dB Wilkinson power divider [55] for power splitting, which was in wideband operation, and a non-coupled-line broadband 180° phase shifter introduced in the former section for phase shifting. Compared to the prior arts [47-50], the proposed balun does not require employing the inter-digital Lange couplers, the broadside coupling lines or the high permittivity substrate to achieve tight coupling. As such, the new balun can be easily fabricated on a single layer PCB substrate, which is inexpensive and simple in structure. Also, the balun can be integrated with antennas at the same substrate having a low dielectric constant for achieving high efficiency. In addition, the proposed balun can also show a good matching and isolation for the two balanced ports. This could greatly improve the circuit performance. To demonstrate the design methodology, one prototype of the balun has been presented. The design was simulated using the commercial software IE3D and validated by the measurement. Measured return loss for the unbalanced port is less than -10 dB in the frequency range from 1.7 GHz to 3.3 GHz, or 64%. The measured return losses for both the two balanced ports are better than -10 dB, and the balanced port isolation is below -15 dB across the operation bandwidth. Within the operation bandwidth, the measured amplitude and phase imbalance between the two balanced ports are within 0.3 dB and $\pm 5^\circ$, respectively.

5.3.1 Design theory

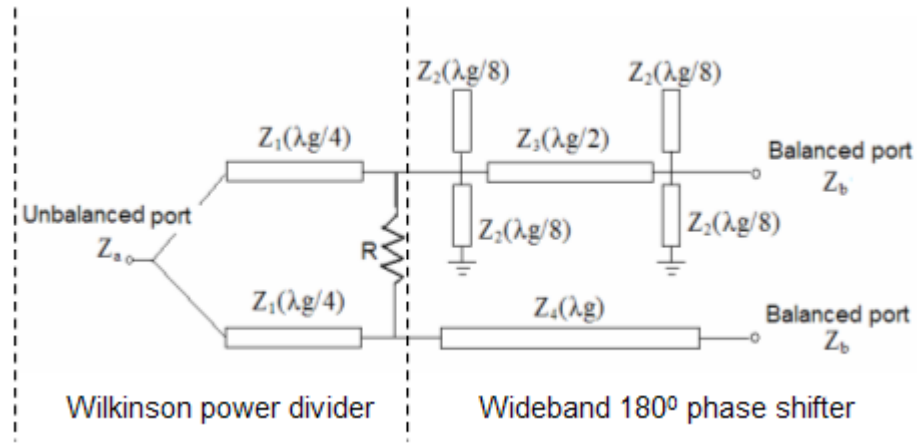


Figure 5.12: Circuit schematic of the proposed planar balun

The proposed balun structure comprised of a two-way equal power division Wilkinson power divider cascaded by a broadband 180° phase shifter [56] as shown in Figure 5.12. From Figure 5.12, it was found that equal power division was achieved by Wilkinson power divider. After the original input signal was split in two, they passed through the two paths of the 180° phase shifter respectively to obtain a stable phase shifting. Because of the wide bandwidth characteristic of the phase shifter, the balun could operate across a reasonably broad band. In Figure 5.12, Z_a and Z_b stand for the input and output port impedance respectively, Z_1 stands for the characteristic impedance of the quarter wavelength microstrip-lines in the power divider, Z_2 stands for the characteristic impedance of the shunted open and short circuit $\lambda/8$ microstrip-lines used in the phase shifter, Z_3 stands for the characteristic impedance of the main microstrip-line, Z_4 stands for the characteristic impedance of the reference line.

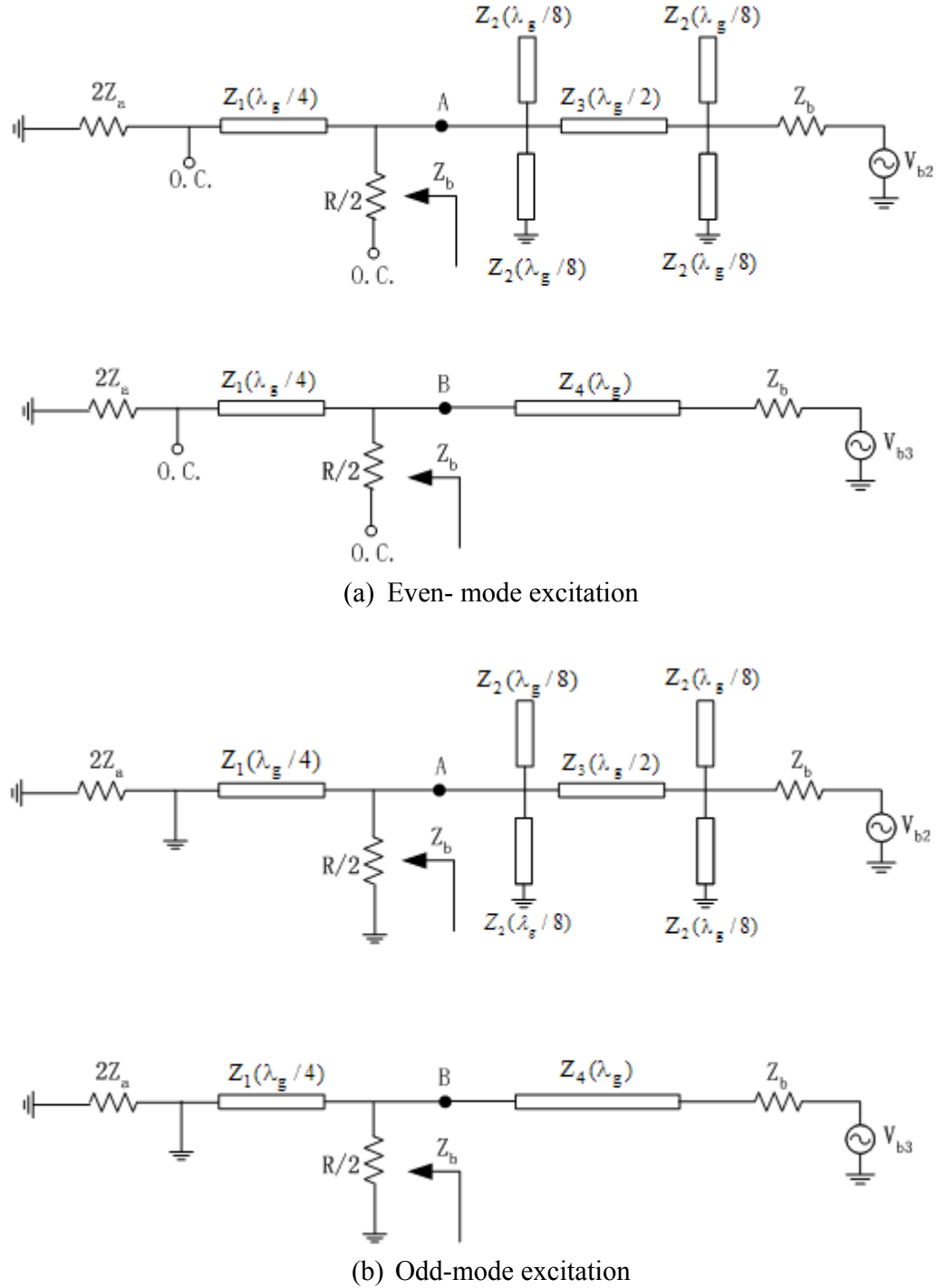


Figure 5.13: Even- and odd-mode analysis of the proposed balun structure

As shown in Figure 5.13, the even-odd mode analysis is employed on the Balun structure:

For the even mode excitation, $V_{b2} = V_{b3} = 2 V$, and no current flows through the $R/2$ resistors.

If we deem the unbalanced port impedance Z_a as two shunted $2Z_a$ resistors, there is no current flowing through each other. Thus we can bisect the network of Figure 5.11 with open circuit as shown in Figure 5.13(a). For the odd mode excitation, $V_{b2} = -V_{b3} = 2 \text{ V}$, and there is a voltage null at the midline point of circuit. Thus we can bisect the network of Figure 5.11 with short circuit as shown in Figure 5.13(b). To keep both even- and odd-mode impedance matching, input impedance at points A and B is required to be Z_b . To make Wilkinson power divider achieve impedance transforming from unbalanced port impedance Z_a to input impedance Z_b at points A and B, a proper value of Z_1 and R was determined. (5.18)-(5.22) presents design equations for the proposed planar balun structure in a general way. It is important to note that for equations (5.20)-(5.21), we referred to [56] to get the optimized coefficients 1.27 and 1.61.

$$Z_1 = \sqrt{2Z_a \cdot Z_b} \quad (5.18)$$

$$R = 2 \cdot Z_b \quad (5.19)$$

$$Z_2 = 1.27 \cdot Z_b \quad (5.20)$$

$$Z_3 = 1.61 \cdot Z_b \quad (5.21)$$

$$Z_4 = Z_b \quad (5.22)$$

5.3.2 Structure description

To demonstrate the methodology mentioned above, a planar balun operating at central frequency of 2.4 GHz was fabricated. The layout graph of the planar balun is shown in Figure 5.14. It was designed on the microwave substrate RO4003 of thickness 0.8 mm and dielectric constant $\epsilon_r=3.38$. For convenience, the balanced and unbalanced ports impedances were all set to be 50Ω . In this new design, U-shaped microstrip-lines were used to minimize the size, and the short circuit was attained through 0.4 mm diameter via holes connected to the ground.

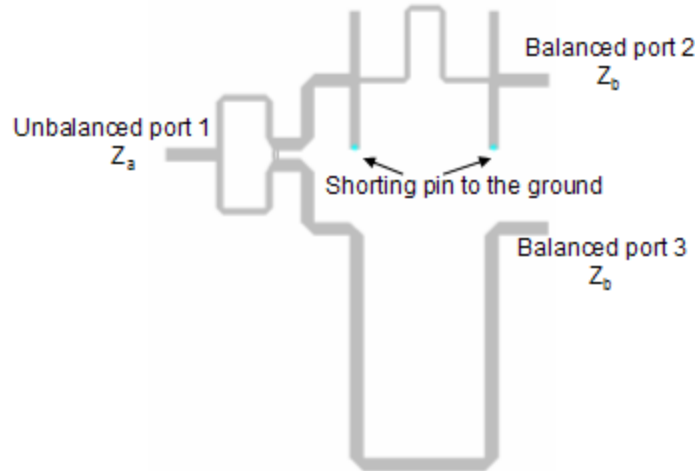
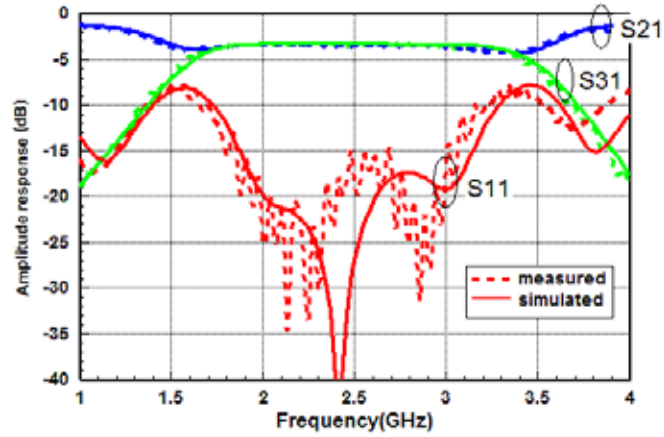


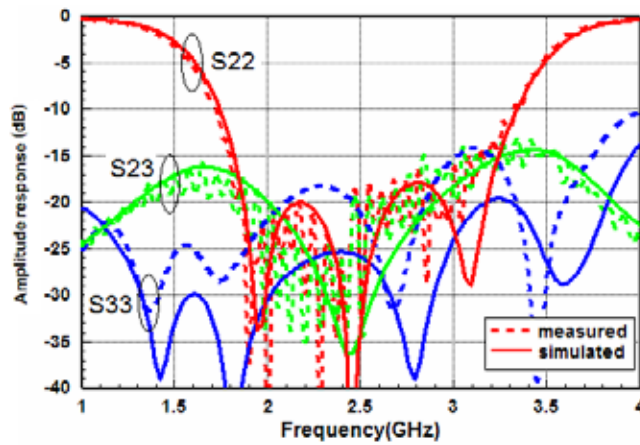
Figure 5.14: Layout graph of the planar balun

5.3.3 Simulation and measurement results

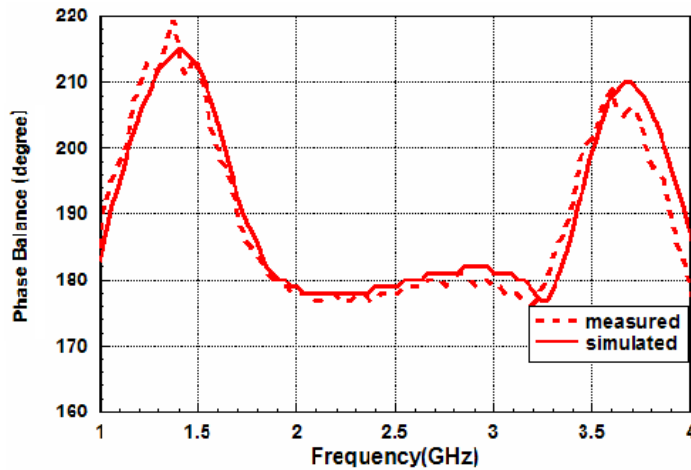
Figures 5.15(a)-(c) display the simulated and measured results for the amplitude and phase responses of the proposed planar balun. Figure 5.15(a) shows the return loss of the unbalanced port and the transmission responses between the unbalanced port and both of the two balanced ports. Figure 5.15(b) shows the return losses and isolation of both the two balanced ports. Figure 5.15(c) shows the phase difference between both of the two balanced ports. The new balun was simulated using EM simulation software IE3D. The measurement was carried out on the HP8510C vector network analyzer. It was observed that good agreement was achieved between measurement and simulation. The measured return loss for the unbalanced port was found to be below -15 dB in the frequency range from 1.8 GHz to 3.1 GHz, or 53%, and better than -10 dB over the frequency band from 1.7 to 3.3 GHz, or 64%. Within the operation band, the measured return losses for both the two balanced ports are better than -10 dB, and the balanced port isolation is below -15 dB. The measured amplitude and phase imbalance between the two balanced ports are within 0.3 dB and 5° , respectively, over the operating frequency band. Figure 5.16 shows the board photograph.



(a) Input return loss and insertion loss response



(b) Output return losses and isolation response



(c) Phase balance response

Figure 5.15: S parameter response of the newly proposed planar balun

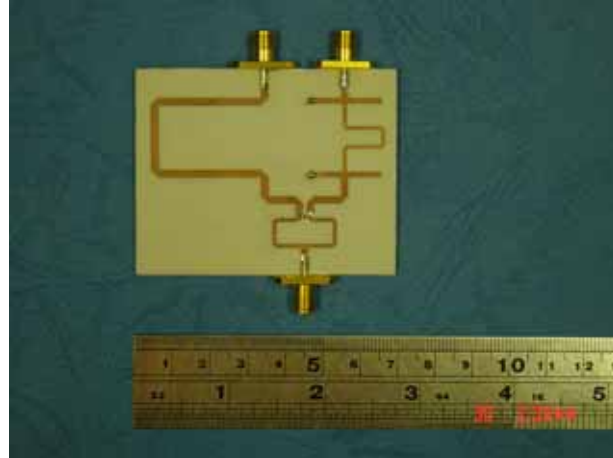


Figure 5.16: Photograph of the fabricated board

5.3.4 Comparison and discussion

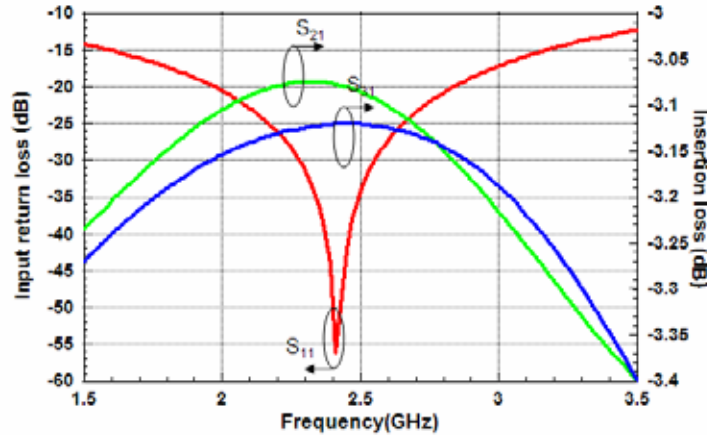


(a) A single section half-wave balun

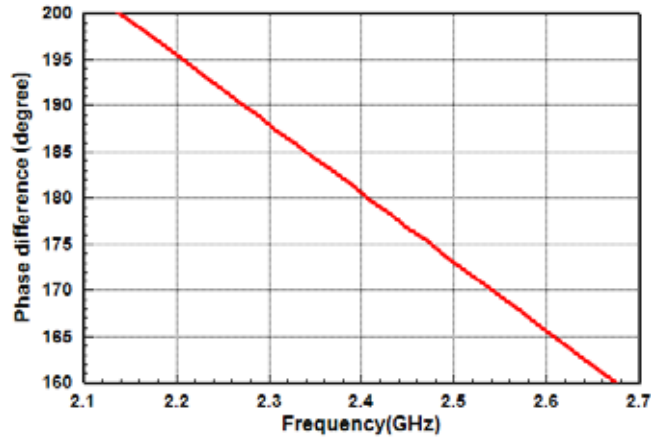
(b) A four-section half-wave balun

Figure 5.17: Half-wave balun structure

To demonstrate the merits of our proposed balun structure, we investigated the performances of N section half-wave baluns. The N section half-wave baluns consisted of several identical half-wave resonators separated by quarter-wave microstrip sections. A simple case of a single section half-wave balun was made up of a Magic T for power splitting and two sections of microstrip line with half wavelength difference. Figure 5.17 shows the N-section half-wave balun structure.



(a) Return losses of the unbalanced port and the transmission responses between the unbalanced port and the two balanced ports



(a) Phase differences of the two balanced ports

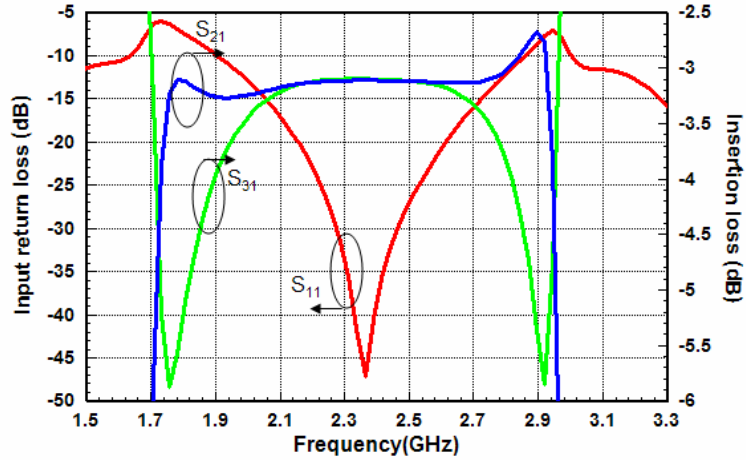
Figure 5.18: Simulated results of a single section half-wave balun

The design of a single section half-wave balun operating at 2.4 GHz was concerned. The circuit was built on the microwave substrate RO4003 of thickness 0.8mm and dielectric constant $\epsilon_r=3.38$. For convenience, unbalanced and balanced ports were set to be 50 Ω . IE3D was used to simulate the performance of the single section half-wave balun. And simulation results of S parameter and phase responses are shown in Figures 5.18(a) and 5.18(b) respectively. From the simulation results, it was observed that with respect to input impedance matching, the single section half-wave balun could obtain around 100%

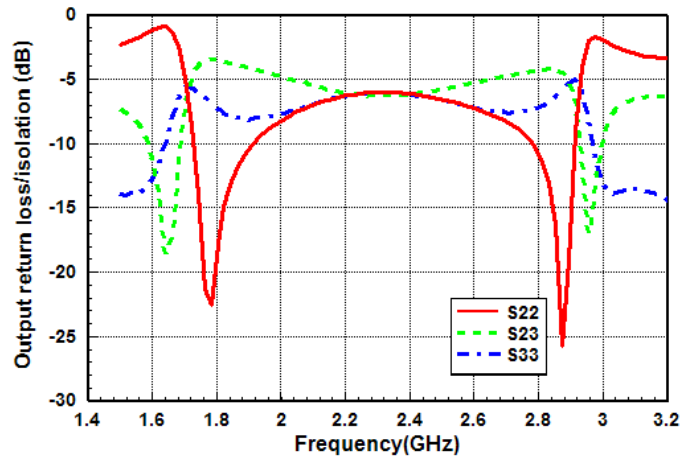
bandwidth for return loss better than -10 dB. The amplitude balance between two balanced ports is within 0.1 dB across the operating band. However, the phase difference between balanced ports is not stable. For $\pm 5^\circ$ phase error tolerance, the phase bandwidth is from 2.34-2.47 GHz, or 5.4% bandwidth.

Cascading identical sections at the output end of the single section half-wave balun could improve the phase bandwidth performance. Here, we took a 3-section half-wave balun as an example. It was built on the same substrate as the single section one above. Simulation results are shown in Figure 5.19. From the simulation result, we found that the 3-section half-wave balun exhibited an amplitude balance less than 1 dB and a return loss better than -10 dB from 1.9-2.8 GHz, or around 38% bandwidth. Phase imbalance between the two balanced ports is within $\pm 5^\circ$ over the operating frequency band.

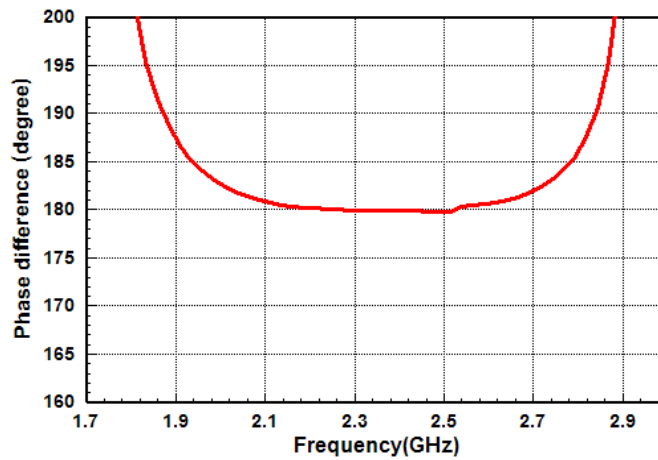
Compared to balun designs in the prior arts, the present balun has the merit of not requiring the coupled line structure. Therefore it could be designed on a variety of substrates and can be integrated with antennas together on the same low-permittivity substrate for achieving high efficiency. Compared with the N section half-wave baluns [45], the present balun showed many advantages in terms of the size, bandwidth, return loss and isolation at the two balanced ports. The planar baluns in [48, 50] using the coupled-line phase shifters could have a wider bandwidth, however they were fabricated on the MMICs or MICs with an edge gap of a few micrometers for achieving tight coupling. Compared with MICs circuit, the conventional PCB fabrication is low cost. The comparisons between the newly proposed balun and the prior arts have been tabulated and summarized in Table 5.2. Note that in Table 5.2 only the bandwidths for the phase imbalanced are listed as they are more critical.



(a) Return losses of the unbalanced port and the transmission responses between the unbalanced port and the balanced ports



(b) Output return losses of balanced ports and isolation between balanced ports



(c) Phase differences of the two balanced ports

Figure 5.19: Simulated results of a three-section half-wave balun

Table 5.2: Comparison between the present design and the prior arts

Item	Bandwidth (phase imbalance)	Complexity	Fabrication cost
N-section half-wave balun (our simulation)	5.4% ($\pm 5^0$), $N=1$	Low	Low (PCB)
	$\sim 38\%$ ($\pm 5^0$), $N \geq 3$		
Roger & Bhartia's balun [48]	107% ($\pm 10^0$)	High	High (MIC)
Bharj et al's balun [50]	127% ($\pm 7^0$)	High	High (MIC)
Present balun	64% ($\pm 5^0$)	Low	Low (PCB)

5.4 Conclusion

This chapter focuses on developing a wideband balun structure which could be easily realized using the conventional PCB technique. To explore the possibility of obtaining a concise balun structure on a single layer PCB using a two-way Wilkinson power divider and a 180^0 phase shifter, we investigated several passive wideband phase shifters. A Schiffman phase shifter was examined for the optimal bandwidth performance when a certain phase derivation is chosen. Since Schiffman phase shifters required tight coupling between coupled lines and were not suitable for large phase shift, a non-coupled-line broadband 180^0 phase shifter structure was studied. As such, we presented a novel planar balun structure on a single-layer PCB using this wideband 180^0 phase shifter. A prototype was designed, simulated, fabricated and measured. Good agreement between simulation and measurement was achieved. The measured results exhibited that the proposed planar balun had an octave bandwidth from 1.7 to 3.3 GHz. The measured amplitude and phase imbalances between two balanced ports were within 0.3 dB and $\pm 5^0$, respectively, over the operating frequency band. Measured results of the matching and isolation at the two balanced ports also showed good performance within the operation band.

Chapter 6

Conclusion

This thesis focuses on the miniaturization and bandwidth enhancement of balun designs for wireless applications fabricated on the Low Temperature Co-fired Ceramic (LTCC) or the conventional Printed Circuit Board (PCB) substrate.

The miniaturization of balun designs using LTCC technique is one of the objectives of this thesis. A 2.4GHz conventional Marchand balun and an improved full-matching Marchand balun were realized using the LTCC technique in bid to achieve smaller size occupation. Moreover, the LC resonance method was employed in LTCC balun structures so that the size could be further reduced. Several LC resonance balun structures were analyzed using even-odd mode analysis method with the design curves plotted. Based on the design curves, design examples have been presented to demonstrate the analysis process.

Marchand baluns are difficult to realize in a single layer PCB environment due to tight coupling requirements. In prior arts, Marchand baluns were commonly built with a multilayer broadside coupled structure or built using the MIC technique. We explored the means of designing a Marchand balun on a single-layer and double-side low dielectric substrate. The conventional Marchand balun was also examined, based on which design curves were plotted.

CHAPTER 6 . CONCLUSION

According to the analysis, it was found that a big even-odd mode impedance ratio was required for the conventional Marchand balun design. To attain the desired even-odd mode impedance ratio, a planar Marchand balun using a patterned ground plane has been presented in a single layer PCB environment. In this new design, with the ground plane under the coupled lines removed, the even-mode capacitance was decreased substantially. Meanwhile, two additional separated rectangular conductors were placed under the coupled lines to act as two capacitors so that the odd-mode capacitance was increased. As such, a well-matched Marchand balun on a double-sided PCB has been achieved.

A broadband uniplanar balun transition has been presented. The proposed structure provides a planar configuration which greatly eases its use in many applications. It consists of a section of edge coupled transmission line, and a taper is employed on both of the coupled lines to increase its bandwidth. The proposed transition can either be employed in microstrip-to-microstrip or microstrip-to-CPS applications. The performance of the newly proposed transition has been investigated in terms of a microstrip-to-microstrip and a microstrip-to-CPS transition.

A wideband balun structure, which can be easily realized using the conventional PCB technique, has been developed. Considering the possibility of achieving a concise balun structure on a single layer PCB, using a two-way Wilkinson power divider and a 180^0 phase shifter, several passive wideband phase shifters were investigated. The Schiffman phase shifter was examined for the optimal bandwidth performance when a certain phase derivation was chosen. Since Schiffman phase shifters require tight coupling between coupled lines and are not suitable for large phase shift, a non-coupled-line broadband 180^0 phase shifter structure was studied. We have presented a novel planar balun structure on a single-layer

CHAPTER 6 . CONCLUSION

PCB using this wideband 180° phase shifter. A prototype has been designed, simulated, fabricated and measured. Good agreement between simulation and measurement has been achieved.

Although a balun is a small device in microwave engineering, it holds an important role in many applications. The scope of this thesis covers one aspect of balun investigations and is far from being an all-encompassing research work on balun. In this thesis, the baluns have been mostly investigated as single components. However, ultimately, they should be able to perform effectively from a system point of view. An evaluation of their performance and development of balun applications in a wireless communications system are research areas which could be explored. I hope my thesis can provide some useful information for further research work.

Bibliography

- [1] N. Marchand, "Transmission-line conversion transformers," *Electronics*, vol. 17, pp. 142-146, Dec 1944.
- [2] E.G. Fubini, "Stripline radiators," *IRE Trans. Microwave Theory Tech.*, vol. MTT-3, pp. 149-156, March 1955.
- [3] R. Bawer, and J.J. Wolfe, "A printed-circuit balun for use with spiral antennas," *IRE Trans. Microwave Theory Tech.*, vol. MTT-8, pp. 319-325, May 1960.
- [4] B.R. Hallfold, "A designer's guide to planar mixer baluns," *Microwaves*, Vol. 18, pp. 52-57, Dec 1979.
- [5] R. Bassett, "Three balun designs for push-pull amplifiers," *Microwaves*, Vol. 19, pp. 47-52, July 1980.
- [6] D.E. Baker, J.R. Nortier, and C.A. Van der Neut, "Design and performance of a microstrip balun for archimedes spiral antennas," *Trans. S. Afr. Inst. Electr. Eng.*, Vol. 78, pp. 34-37, Dec 1987.
- [7] D. Raicu, "Design of planar, single-layer microwave baluns," *IEEE MTT-S Symp. Dig.*, pp. 801-804, 1998.
- [8] V. Tritunovic and B. Jokanovic, "Four decade bandwidth uniplanar balun," *Electronics Letters*, Vol. 28, pp. 534-535, 1992.
- [9] D. Heo, A. Sutono, E. Chen, Y. Suh, and J. Laskar, "A 1.9-GHz DECT CMOS power amplifier with fully integrated multilayer LTCC passives," *IEEE Microwave and Wireless Components Letters*, Vol. 11, pp. 249-251, June 2001.
- [10] J. Kassner, and W. Menzel, "A drop-on band-pass filter for millimeter-wave multichip modules on LTCC," *IEEE Microwave and Wireless Components Letters*, Vol. 9, pp. 256-257, Nov 1999.
- [11] J. Heyen, T.V. Kerssenbrock, A. Chernyakov, P. Heide, and A.F. Jacob, "Novel LTCC-/BGA-modules for highly integrated millimeter-wave transceivers," in *IEEE Int. Microwave Symp. Dig.*, 2003, pp. 1041-1044.

BIBLIOGRAPHY

- [12] R. Yu, K.A. Zaki, M. Hageman, D. Stevens, and J. Gipprich, "Low temperature cofired ceramic (LTCC) ridge waveguide bandpass filters," *IEEE MTT-S Symp. Dig.*, pp. 1147-1150, 1999.
- [13] A. Sawicki, and K. Sachse, "A novel directional coupler for PCB and LTCC applications," in *IEEE MTT-S Int. Microwave Symp. Dig.*, pp. 2225-2228, 2002.
- [14] Y. Dakeya, T. Suesada, K. Asakura, and N. Nakajima, and H. Mandai, "Chip multilayer antenna for 2.45 GHz-band application using LTCC technology," in *IEEE MTT-S Int. Microwave Symp. Dig.*, pp. 1693-1696, 2002.
- [15] C.W. Tang, J.W. Sheen, and C.Y. Chang, "Chip-type LTCC-MLC baluns using the stepped impedance method," *IEEE Trans. Microwave Theory Tech.*, vol. 45, pp. 2150-2152, Dec 1997.
- [16] J.W. Sheen, and C.W. Tang, "LTCC-MLC balun for WLAN/Bluetooth," in *IEEE MTT-S Int. Microwave Symp. Dig.*, 2001, pp. 315-318.
- [17] K.S. Ang, I.D. Robertson, "Analysis and design of impedance-transforming planar marchand baluns," *IEEE Trans. Microwave Theory Tech.*, vol. 49, pp.402-406, Feb 2001.
- [18] LTCC design guide, Kyocera America LTCC Division, July 2003.
- [19] S.P. Ojha, G.R. Branner, and B.P. Kumar, "A miniaturized lumped-distributed balun for modern wireless communication systems," in *Proc. IEEE Midwest Circuits and Systems Symp.*, Vol. 3, 1996, pp. 1347-1350.
- [20] C.W. Tang and C.Y. Chang, "LTCC-MLC chip-type balun realized by LC resonance method," *Electronics Letters*, Vol. 38, pp. 519-520, 2002.
- [21] C.W. Tang and C.Y. Chang, "A semi-lumped balun fabricated by low temperature cofired ceramic," in *IEEE MTT-S Int. Microwave Symp. Dig.*, pp. 2201-2204, 2002.
- [22] K.S. Ang, Y.C. Leong, and C.H. Lee, "Analysis and design of miniaturized lumped-distributed impedance-transforming baluns," *IEEE Trans. Microwave Theory Tech.*, vol. 51, pp.1009-1017, March 2003.
- [23] T. Chen et al., "Broadband monolithic passive baluns and monolithic double balanced mixer," *IEEE Trans. Microwave Theory Tech.*, vol. 39, pp. 1980-1986, Dec 1991.
- [24] P.C. Hsu, C. Nguyen, and M. Kintis, "Uniplanar broad-band push-pull FET amplifier," *IEEE Trans. Microwave Theory Tech.*, vol. 45, pp. 2150-2152, Dec 1997.

BIBLIOGRAPHY

- [25] B.A. Munk, "Balun, etc.," chapter 23 in *Antennas for all application* (third edition) by J.D. Kraus, and R.J. Marhefka, McGraw-Hill, 2002.
- [26] C. Cho, and K.C. Gupta, "A new design procedure for single-layer and two-layer three-line baluns," *IEEE Trans. Microwave Theory Tech.*, vol. 46, pp. 2514-2519, Dec 1998.
- [27] A.M. Pavio and A. Kikel, "A monolithic or hybrid broadband compensated balun," in *IEEE MTT-S Int. Microwave Symp. Dig.*, 1990, pp.483-486.
- [28] M.C. Tsai, "A new compact wide-band balun," in *IEEE Microwave Millimeter-wave Monolithic Circuits Symp. Dig.*, 1993, pp.123-125.
- [29] M. Shimosawa, K. Itoh, Y. Sasaki, H. Kawano, Y. Isota, and O. Ishida, "A parallel connected Marchand balun using spiral shaped equal length coupled lines," in *IEEE MTT-S Int. Microwave Symp. Dig.*, 1999, pp. 1737-1740.
- [30] K. Nishikawa, I. Toyoda, and T. Tokumitsu, "Compact and broadband three-dimensional MMIC balun," *IEEE Trans. Microwave Theory Tech.*, vol. 47, pp. 96-98, Jan 1999.
- [31] Y.J. Yoon, Y. Lu, R.C. Frye, M.Y. Lau, P.R. Smith, L. Ahlquist and D.P. Kossives, "Design and characterization of multilayer spiral transmission-line baluns," *IEEE Trans. Microwave Theory Tech.*, vol. 47, pp. 1841-1847, Sept 1999.
- [32] R. Mongia, I. Bahl, and P. Bhartia, *RF and Microwave Coupled-Line Circuits*. Norwood, MA: Artech House, 1998, pp. 109-114.
- [33] K.S. Ang, Y.C. Leong, and C.H. Lee, "Multisection Impedance-Transforming Coupled-Line Baluns," *IEEE Trans. Microwave Theory Tech.*, vol. 51, pp.536-541, Feb. 2003.
- [34] D. M. Pozar. *Microwave Engineering*, 2nd ed., Wiley, New York, 1998, pp. 388-391.
- [35] G.I. Zysman and A.K. Johnson, "Coupled Transmission Line Networks in an Inhomogeneous Dielectric Medium," *IEEE Trans. Microwave Theory Tech.*, vol. MTT-17, No. 10, pp. 753-759, Oct. 1969.
- [36] N.I. Dib, R.N. Simons, and L.P.B. Katehi, "New uniplanar transitions for circuit and antenna applications," *IEEE Trans. Microwave Theory Tech.*, vol. 43, pp. 2868-2873, Dec. 1995.
- [37] Y. Qian and T. Itoh, "A broadband uniplanar microstrip-to-CPS transition," in *Microwave Conf. Proc., AMPC '97*, vol. 2, pp. 609-612, 1997.

BIBLIOGRAPHY

- [38] Y.H. Suh and K. Chang, "A wideband coplanar stripline to microstrip transition," *IEEE Microwave and Wireless Component Lett.*, vol. 11, No. 1, Jan, 2001.
- [39] K. Tilley, X.-D. Wu, and K. Chang, "Coplanar waveguide fed coplanar strip dipole antenna," *Electron. Lett.*, vol. 30, no. 3, pp. 176–177, Feb, 1994.
- [40] M.-Y. Li, K. Tilley, J. McCleary, and K. Chang, "Broadband coplanar waveguide-coplanar strip-fed spiral antenna," *Electron. Lett.*, vol. 31, pp. 4-5, Jan. 1995.
- [41] J.W. Duncan, and V.P. Minerva, "100:1 Bandwidth balun transformer," *Proc. IRE.* vol. 48, pp. 156-164, 1960.
- [42] W. Sichak, J. Nail, "UHF omnidirectional antenna systems for large aircraft," *IEEE. Trans. Antennas and Propagation*, Vol: 2, pp.6 - 15, Jan 1954
- [43] C. Fowler, J. Entzminger, J. Corum, "Assessment of ultra-wideband (UWB) technology," *IEEE Aerospace and Electronic Systems Magazine*, Vol:5, pp.45-49, Nov. 1990
- [44] G. Y. Chen, and J. S. Sun, "A printed dipole antenna with microstrip tapered balun" *Microwave and Optical Technology Letters*, vol. 40, pp.344-346, Feb. 2004
- [45] R. Sturdivant, "Balun designs for wireless mixers, amplifiers and antennas," *Applied Microwave*, summer, 1993, pp. 34-44.
- [46] M. Basraoui and S. N. Prasad, "Wideband, planar, log-periodic balun," *IEEE MTT-S Symp. Dig.*, 1998, pp. 785-788.
- [47] Z.Y. Zhang, Y.X. Guo, L.C. Ong, and M.Y.W. Chia, "Improved planar Marchand balun with a patterned ground plane," accepted by *International Journal of RF and Microwave CAE*.
- [48] J. Rogers and R. Bhartia, "A 6 to 20GHz planar balun using a Wilkinson divider and lange couplers," *IEEE MTT-S Symp. Dig.*, 1991, pp. 865-868.
- [49] D.C. Boire, J.E. Degenford and H. Cohn, "A 4.5 to 18 GHz phase shifter," *IEEE MTT-S Symp. Dig.*, 1985, pp. 601-604.
- [50] S.S. Bharj, S.P. Tan, and B. Thompson, "A 2-18 GHz 180 degree phase splitter network," *IEEE MTT-S Symp. Dig.*, 1989, pp. 959-962.
- [51] B.M. Schiffman, "A new class of broad-band microwave 90-degree phase shifters," *IRE Trans. Microwave Theory Tech.*, pp. 232-237, Apr. 1958.

BIBLIOGRAPHY

- [52] B. Schiek, and J. Kohler, "A method for broad-band matching of microstrip differential phase shifters," *IEEE Trans. Microwave Theory Tech.*, vol. 25, pp. 666-671, Aug. 1977.
- [53] J.L.R. Quirarte, and J.P. Starski, "Novel Schiffman phase shifters," *IEEE Trans. Microwave Theory Tech.*, vol. 41, pp. 9-14, Jan. 1993.
- [54] J.L.R. Quirarte, and J.P. Starski, "Synthesis of Schiffman phase shifters," *IEEE Trans. Microwave Theory Tech.*, vol. 39, pp. 1185-1189, Nov. 1991.
- [55] E. Wilkinson, "An N-way hybrid power divider," *IRE Trans. On Microwave Theory and Tech*, MTT-8, 1960, pp. 116-118.
- [56] S. Y. Eom, S. I. Jeon, J. S. Chae and J. G. Yook, "Broadband 180⁰ bit phase shifter using a new switched network," *IEEE MTT-S Symp. Dig.*, 2003, pp. 39-42.
- [57] E.M.T. Jones and J.T. Bolljahn, "Coupled-strip-transmission-line filters and directional couplers," *IRE MTT*, pp. 75-81, Apr, 1956.

List of publications

Journal Papers:

- [1] **Zhen-Yu Zhang**, Y.X. Guo, L.C. Ong, and M.Y.W. Chia, "Improved Planar Marchand Balun Using A Patterned Ground Plane," accepted by International Journal of RF and Microwave Computer-Aided Engineering.
- [2] **Zhen-Yu Zhang**, Y.X. Guo, L.C. Ong, and M.Y.W. Chia, "A new wideband planar balun on a single layer PCB," accepted by IEEE Microwave and Wireless Component Letter.
- [3] **Zhenyu Zhang**, Y.X. Guo, L.C. Ong, and M.Y.W. Chia, "Analysis of Parallel Coupled-Line Bandpass Filters Using a Ground Plane Aperture," accepted by Microwave and Optical Technology Letters.
- [4] **Zhen-Yu Zhang**, Y.X. Guo, L.C. Ong, and M.Y.W. Chia, "Design of LTCC miniaturized baluns realized by LC resonanced method," submitted to International Journal of RF and Microwave Computer-Aided Engineering.

Conference Papers:

- [1] **Zhenyu Zhang**, Y.X. Guo, L.C. Ong, and M.Y.W. Chia, "New Wideband Marchand Balun on Single-Layer PCB," Proceedings of the 4th international workshop on ITS Telecommunications, pp. 323-326, July 8-9, 2004, Singapore.

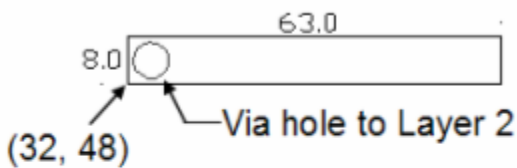
LIST OF PUBLICATIONS

- [2] **Zhenyu Zhang**, Y.X. Guo, L.C. Ong, and M.Y.W. Chia, "A novel Marchand Balun on a double-sided PCB," European Microwave Conference, Amsterdam, The Netherlands, pp. 381-384, Oct, 2004.
- [3] **Zhenyu Zhang**, Y.X. Guo, L.C. Ong, and M.Y.W. Chia, A novel parallel-coupled bandpass filter, European Microwave Conference, pp. 479-482, Oct, 2004, Amsterdam, The Netherlands.
- [4] Y.X. Guo, **Zhenyu Zhang**, and L.C. Ong, "Miniature and dual-band Marchand baluns in LTCC," Progress in Electromagnetics Research Symposium, p. 21-23, Aug 28-31, 2004, Nanjing, China.
- [5] K.W. Khoo, Y.X. Guo, **Zhen-Yu Zhang**, L.C. Ong, and K.M. Luk, Dual L-probe proximity-fed rectangular patch antenna using a broadband balun feeding network, pp. 234-237, Mar, 2005, Singapore.
- [6] **Zhenyu Zhang**, Y.X. Guo, L.C. Ong, and M.Y.W. Chia, "A new planar Marchand Balun," accepted by IEEE MTT-S International Microwave Symposium, June, 2005, California, U.S.A.
- [7] Y.X. Guo, **Zhen-Yu Zhang**, Y.F. Ruan, L.C. Ong, M. Y. W. Chia and X.Q. Shi, A novel UWB tapered balun and its applications on antennas, accepted by Loughborough Antennas & Propagation Conference, April, 2005, Burleigh Court, U.K.

Appendix I – Dimensions of Various LTCC

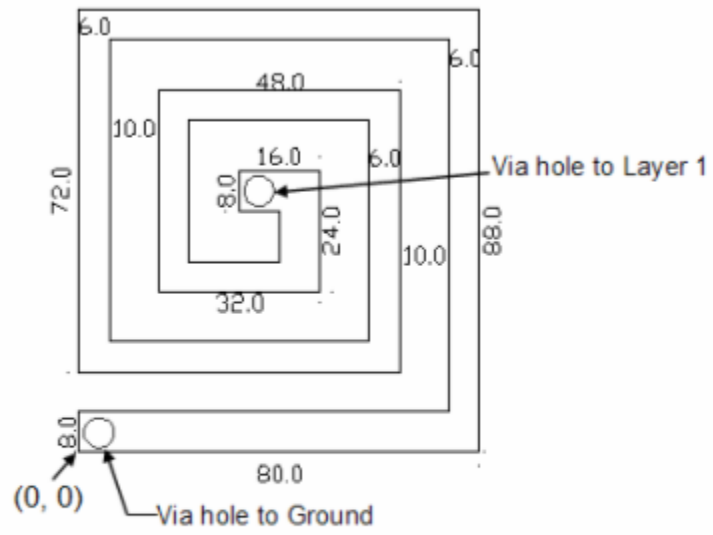
Baluns

Balun Dimensions (in mils) for Figure 2.8 in p.15

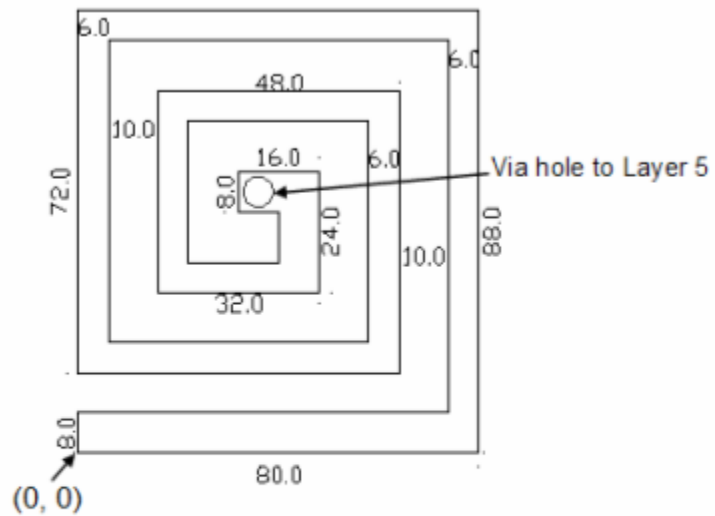


Layer 1 ($z = 3.7$)

APPENDIX I: DIMENSIONS OF VARIOUS LTCC BALUNS

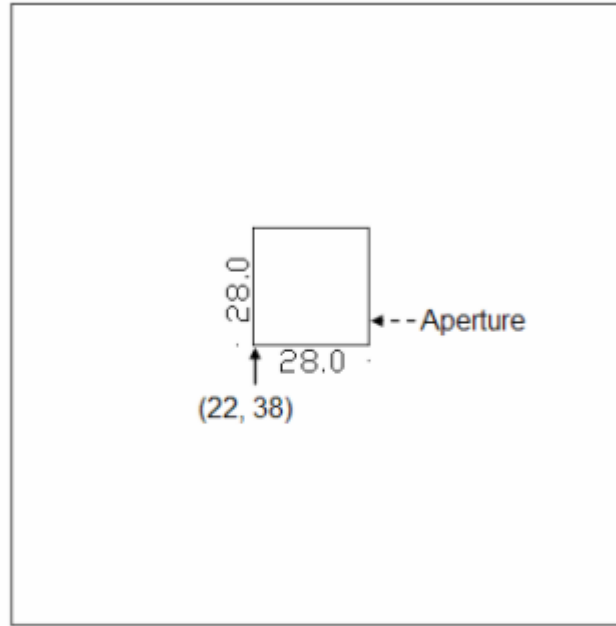


Layer 2 (z = 7.4)

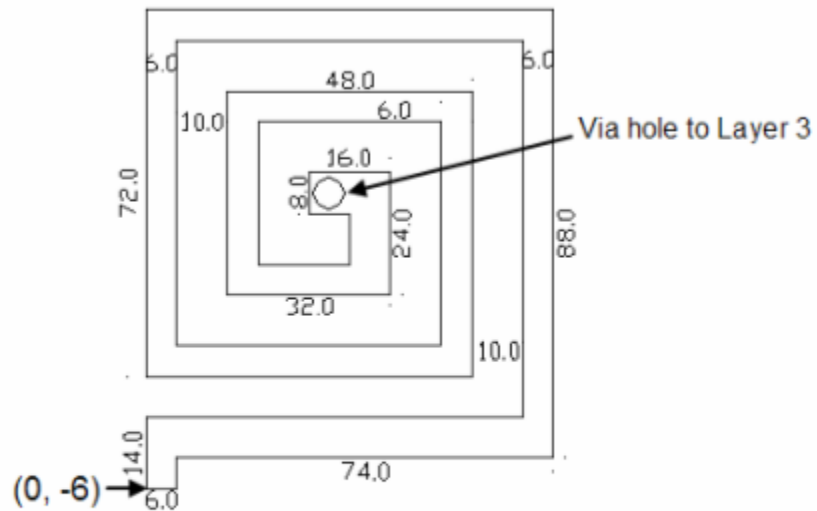


Layer 3 (z = 11.1)

APPENDIX I: DIMENSIONS OF VARIOUS LTCC BALUNS

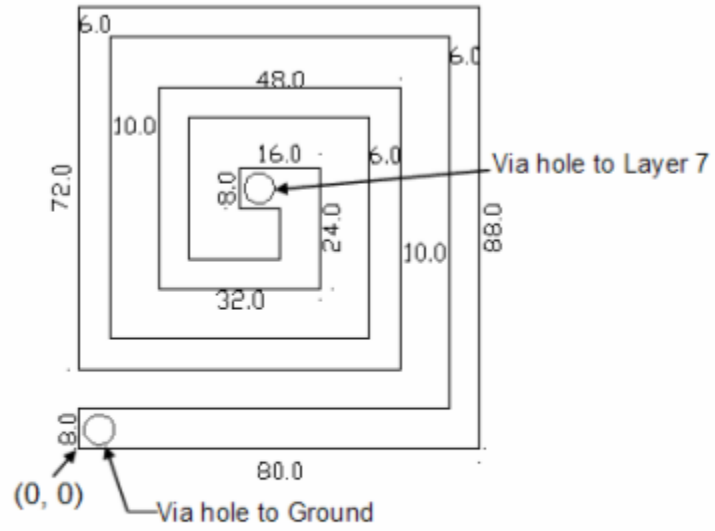


Layer 4 (z = 14.8)

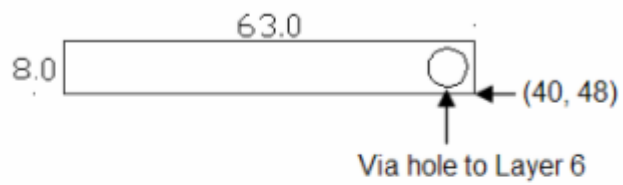


Layer 5 (z = 18.5)

APPENDIX I: DIMENSIONS OF VARIOUS LTCC BALUNS

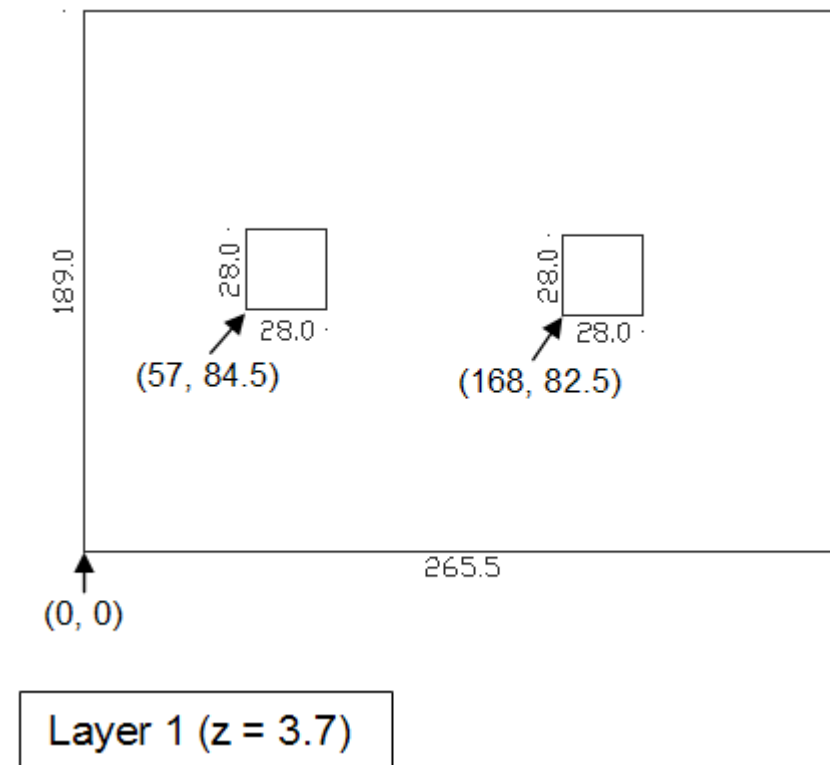
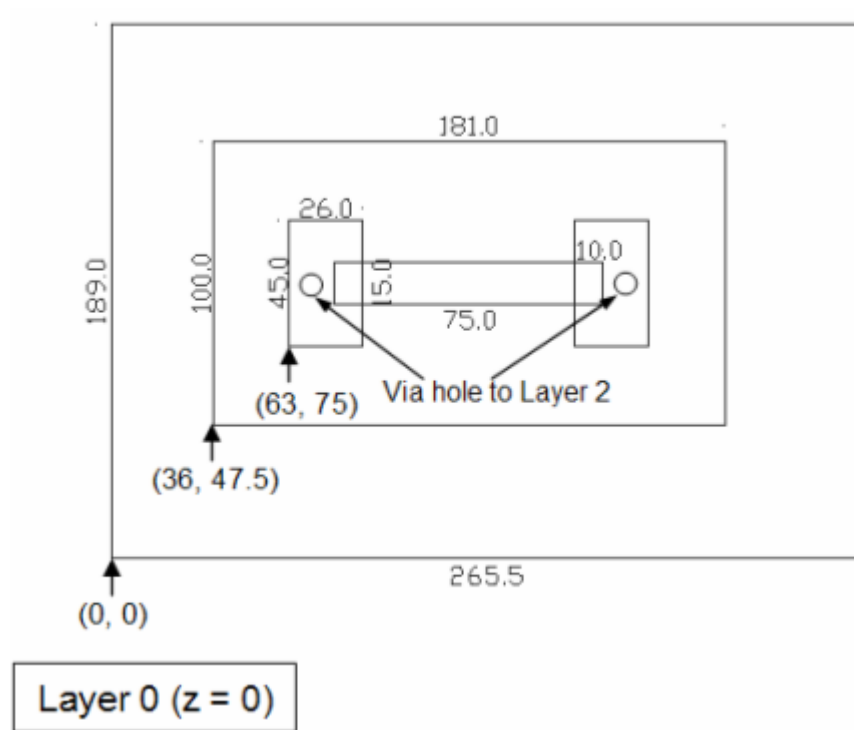


Layer 6 (z = 22.2)

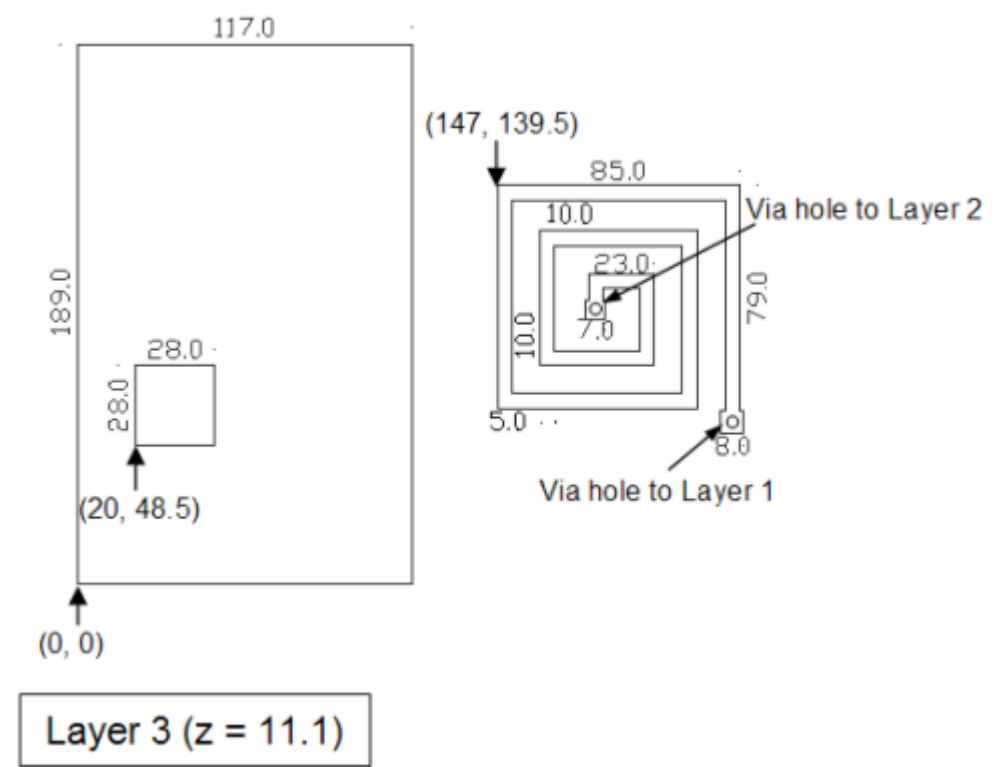
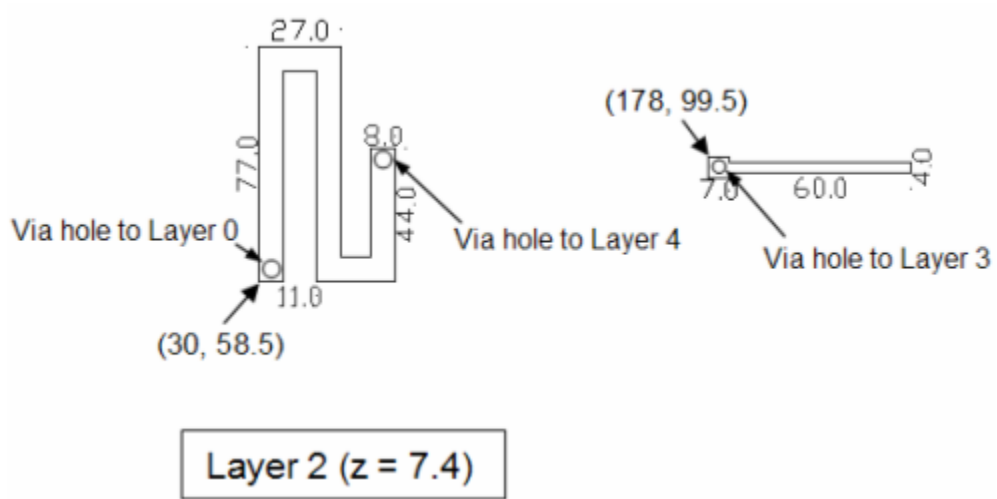


Layer 7 (z = 25.9)

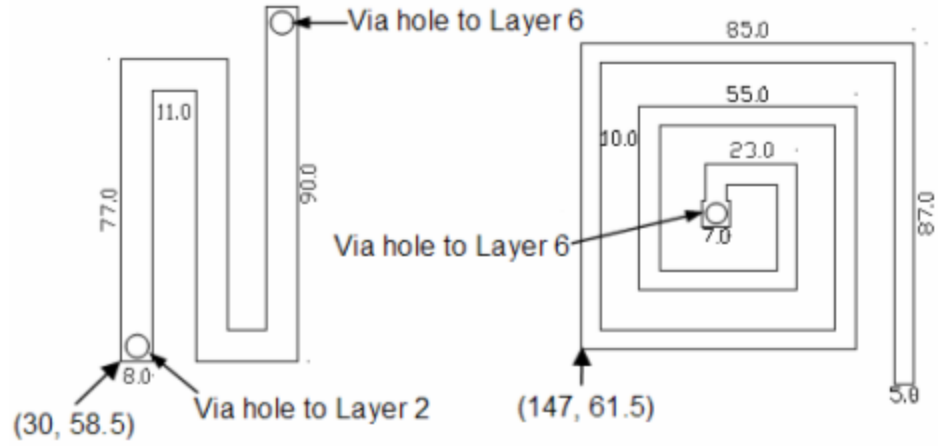
Balun Dimensions (in mils) for Figure 2.14 in p.20



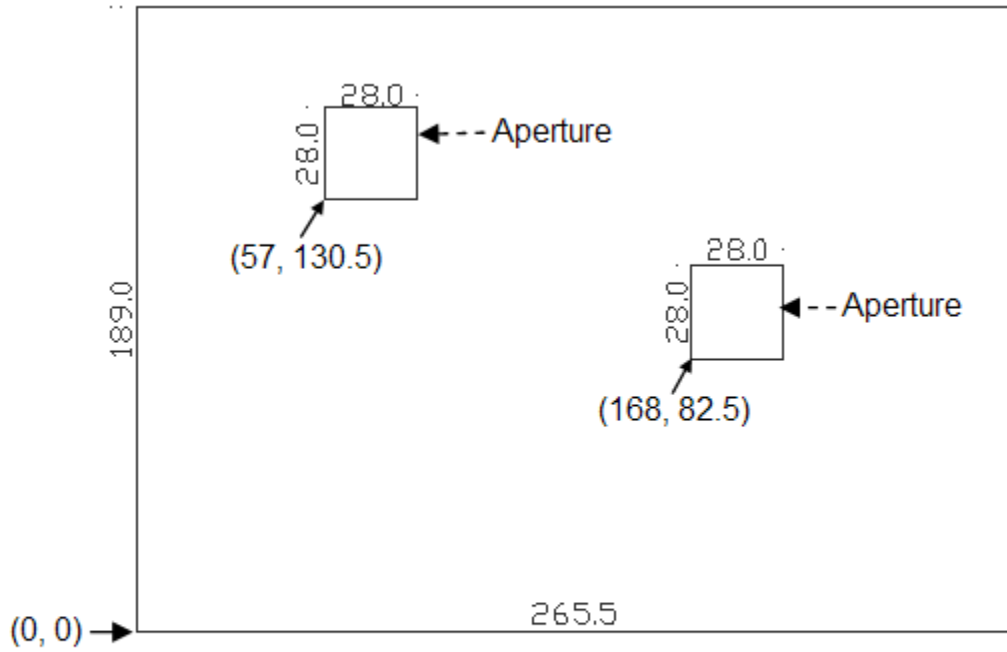
APPENDIX I: DIMENSIONS OF VARIOUS LTCC BALUNS



APPENDIX I: DIMENSIONS OF VARIOUS LTCC BALUNS

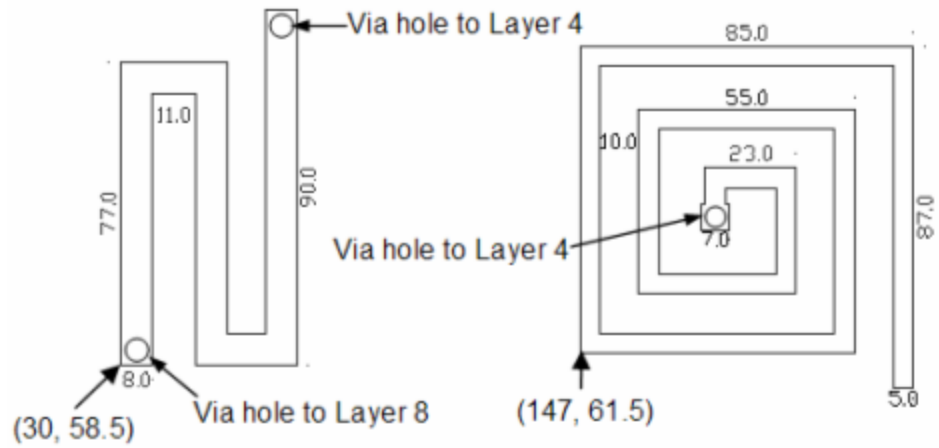


Layer 4 (z = 14.8)

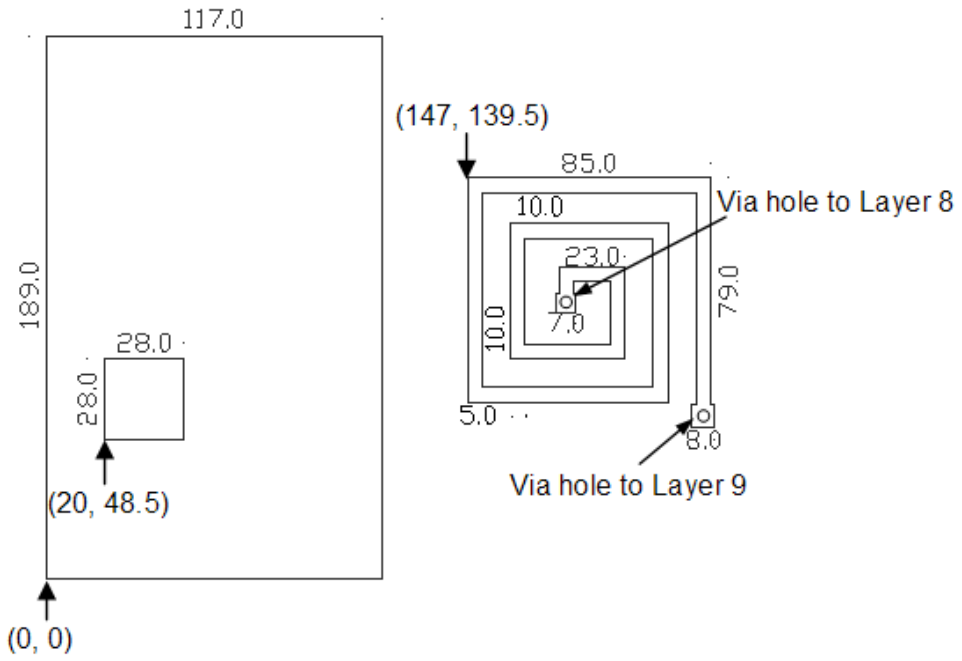


Layer 5 (z = 18.5)

APPENDIX I: DIMENSIONS OF VARIOUS LTCC BALUNS

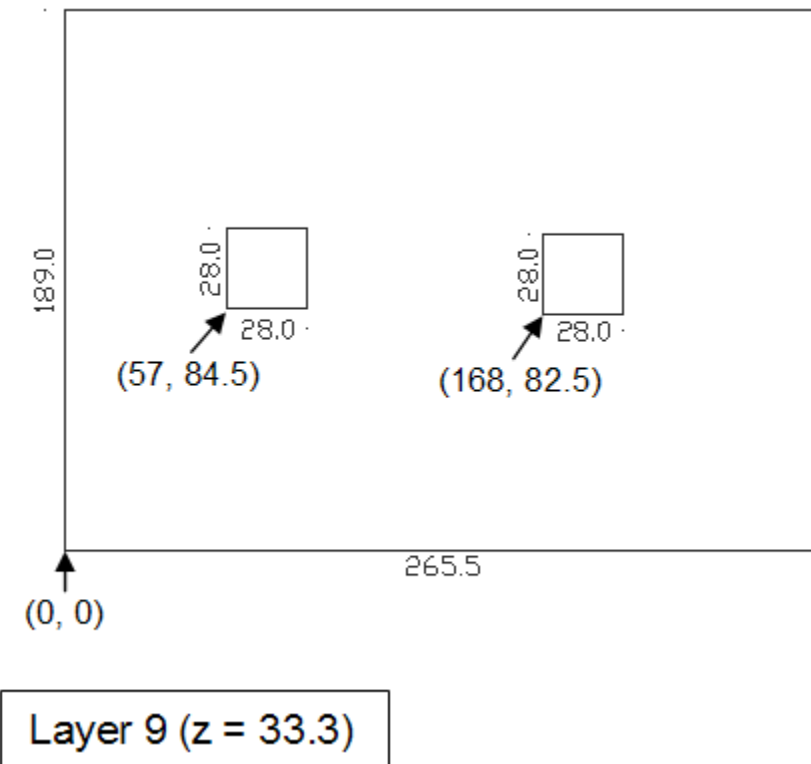
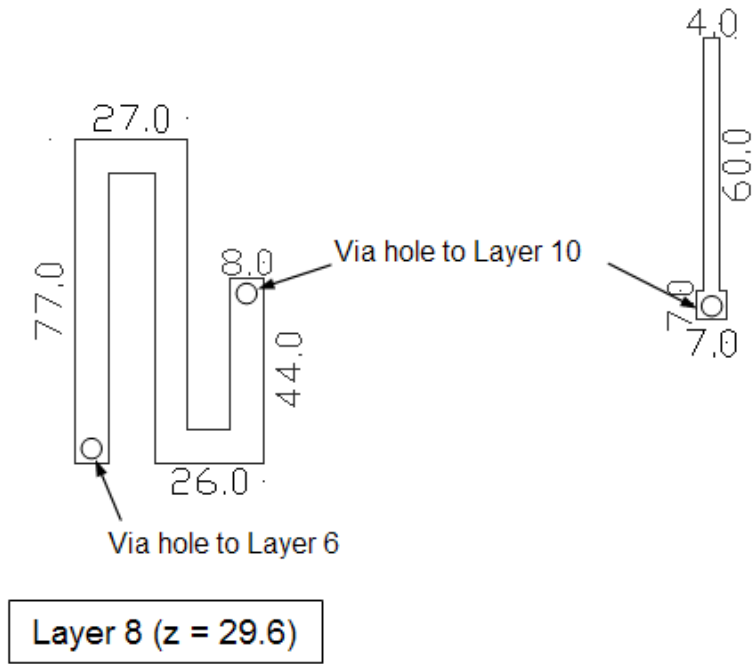


Layer 6 (z = 22.2)

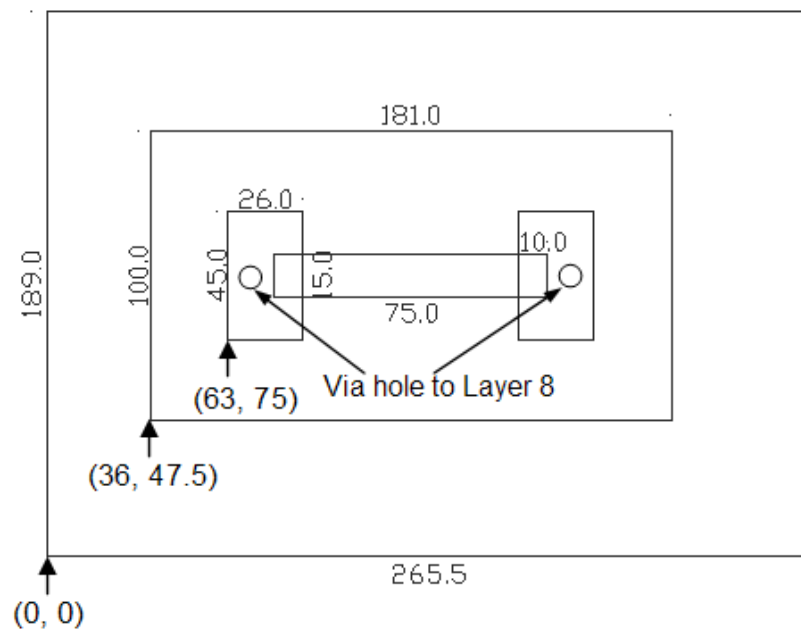


Layer 7 (z = 25.9)

APPENDIX I: DIMENSIONS OF VARIOUS LTCC BALUNS

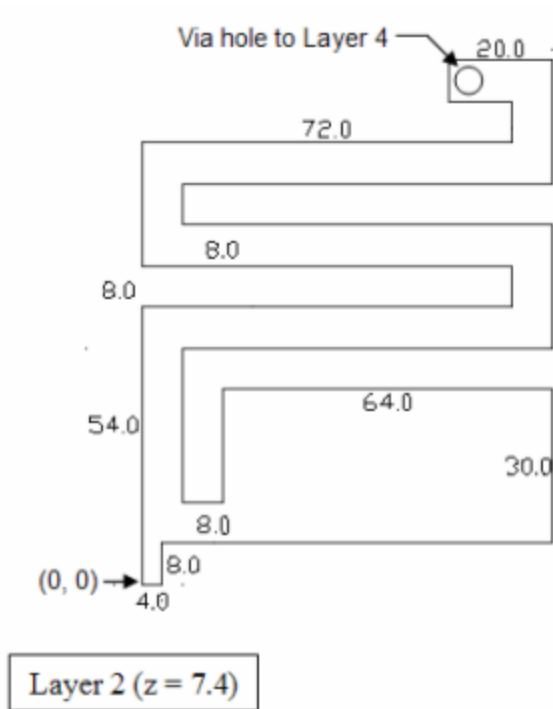
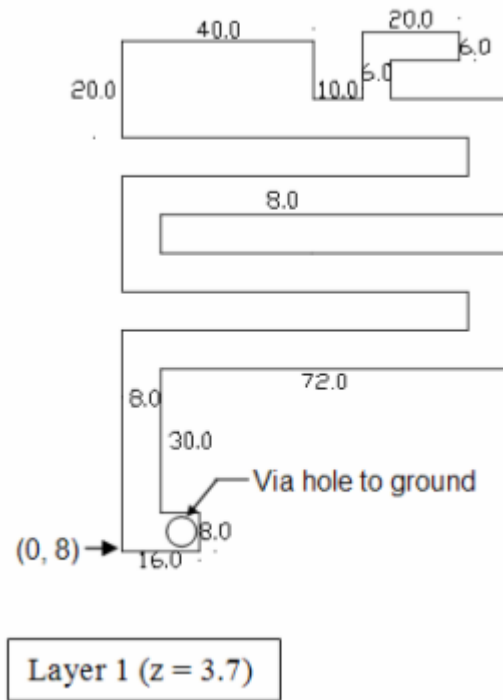


APPENDIX I: DIMENSIONS OF VARIOUS LTCC BALUNS

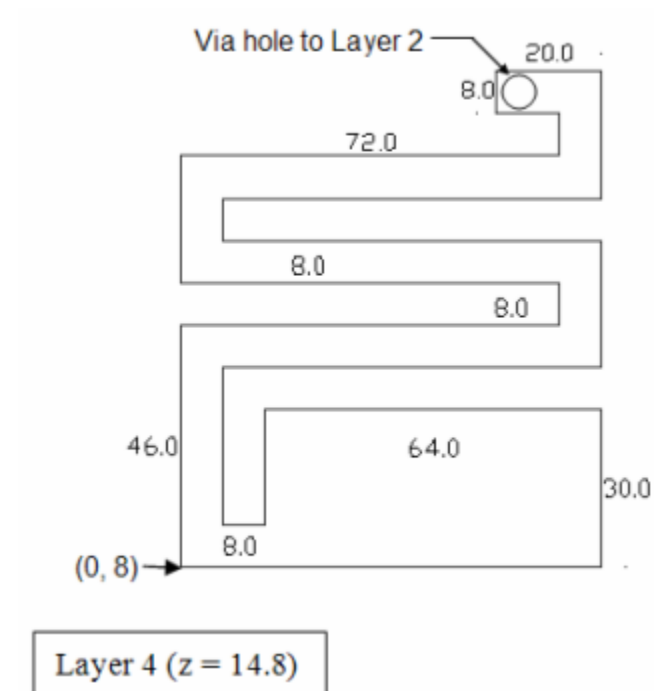
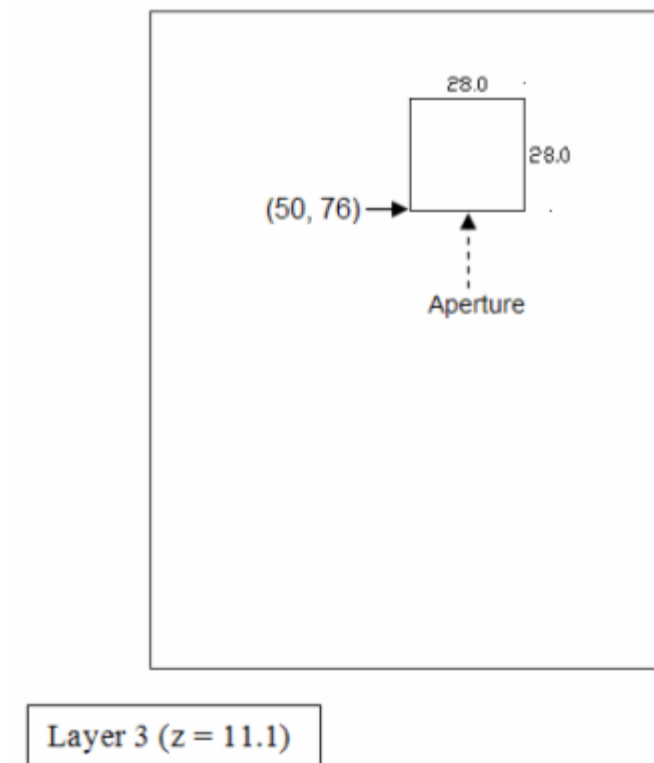


Layer 10 (z = 37)

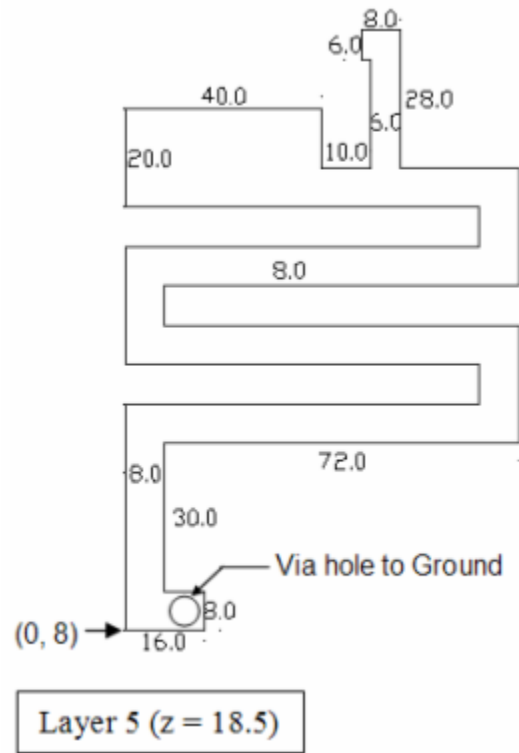
Balun Dimensions (in mils) for Figure 2.26 in p.34



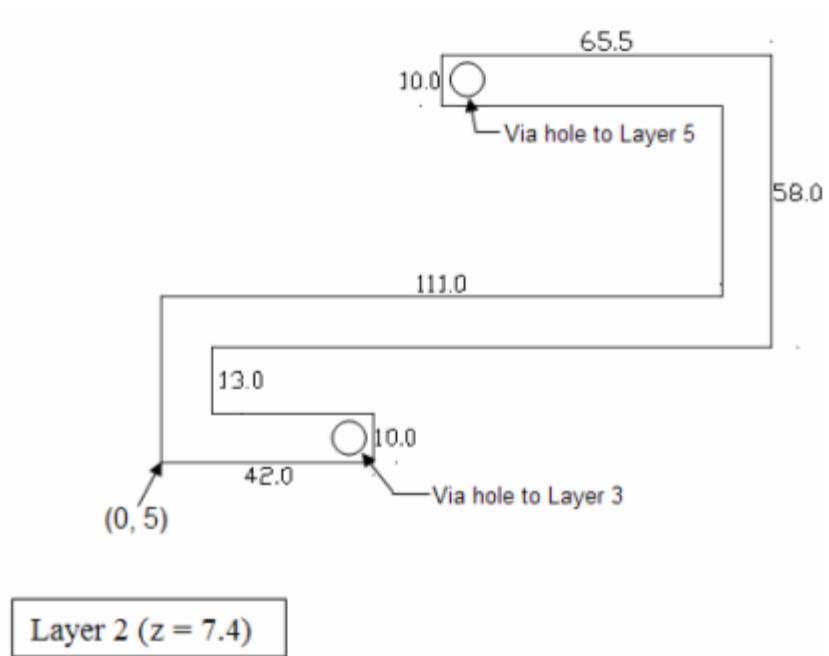
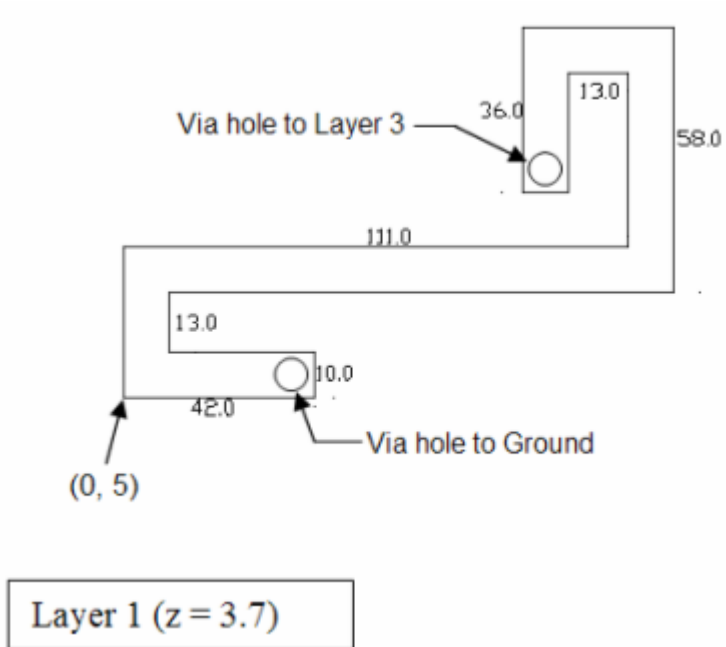
APPENDIX I: DIMENSIONS OF VARIOUS LTCC BALUNS



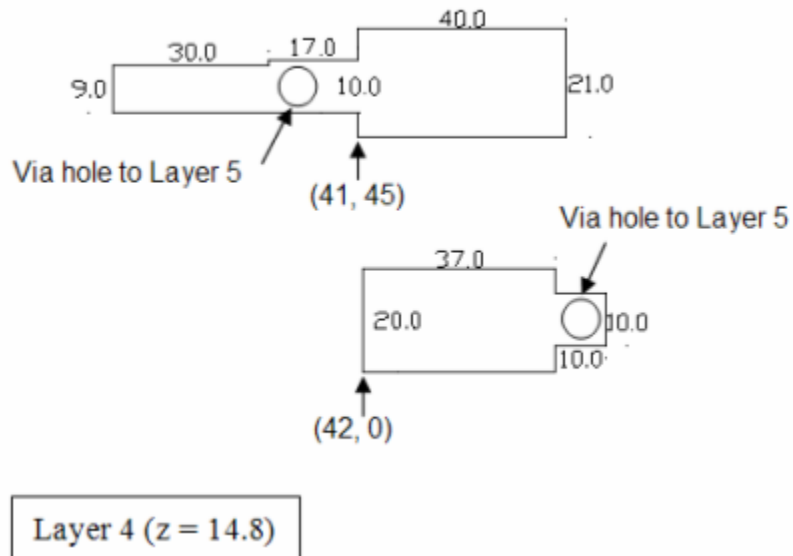
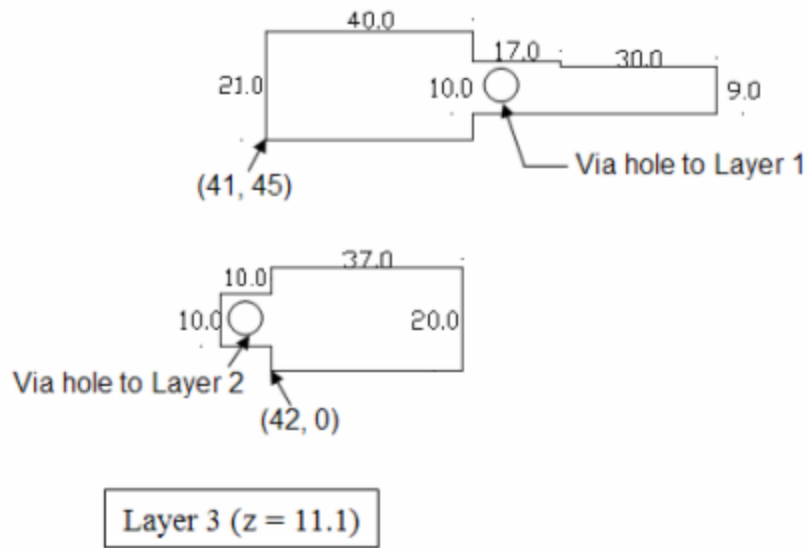
APPENDIX I: DIMENSIONS OF VARIOUS LTCC BALUNS



Balun Dimensions (in mils) for Figure 2.30 in p.38



APPENDIX I: DIMENSIONS OF VARIOUS LTCC BALUNS



APPENDIX I: DIMENSIONS OF VARIOUS LTCC BALUNS

